

# ResearchOnline@JCU

This file is part of the following reference:

**Kim, Peter Young-Han (2012) *Characteristics of internal pressures in buildings with a dominant opening*. MEngSc thesis, James Cook University.**

Access to this file is available from:

<http://researchonline.jcu.edu.au/39261/>

*The author has certified to JCU that they have made a reasonable effort to gain permission and acknowledge the owner of any third party copyright material included in this document. If you believe that this is not the case, please contact*

*[ResearchOnline@jcu.edu.au](mailto:ResearchOnline@jcu.edu.au) and quote  
<http://researchonline.jcu.edu.au/39261/>*

# Characteristics of Internal Pressures in Buildings with a Dominant Opening

Thesis submitted by

Peter Young-Han KIM BEng

in October, 2012

for the degree of Master of Engineering Science

in the School of Engineering and Physical Sciences

James Cook University

## **Acknowledgements**

I would like to thank my supervising committee, Associate Professor John Ginger, Dr. David Henderson and Dr. John Holmes. Their technical advice, guidance and critical feedback throughout the course of this thesis were greatly appreciated. I would especially like to acknowledge my primary supervisor John Ginger, who always had an open door throughout this thesis.

I acknowledge the Cyclone Testing Station (CTS) for their support of this project through the use of equipment and resources, as well as the CTS technical staff, their advice on experimental setup was greatly appreciated. I also acknowledge technical staff from the machine shop of the School of Engineering and Physical Sciences at James Cook University for their help and advice.

Finally, I thank my family and friends for their on-going support and encouragement.

## Abstract

A building with a dominant windward wall opening will produce large internal pressures during a severe wind event and is a structural design criterion. Internal pressures were measured using a boundary layer wind tunnel for a series of windward dominant opening sizes, internal volume sizes and background building porosities. Internal pressures were also estimated using numerical simulations of the governing equation incorporating background porosity. The background porosity was represented as a single lumped porous opening. Results were presented in terms of a non-dimensional dominant opening size to internal volume parameter,  $S^*$  and the lumped background porosity area to dominant opening area parameter,  $\phi_6$ .

The measured internal pressure results were compared with measured external pressures at the dominant opening. For the sealed building scenarios (no background porosity) but with a dominant opening, the mean internal pressure was equal to the mean external pressure, and the internal pressure fluctuations (standard deviation) and peaks were dependent on the size of the dominant opening and size of the internal volume. For porous building scenarios, the internal pressure mean, standard deviation and peaks were attenuated with varying levels of increasing porosity.

The internal pressure numerical simulations were matched with the experimental results by varying the inertial coefficient of the dominant opening and discharge coefficients for the dominant opening and lumped porous opening. The lumped porous opening discharge coefficients varied with the dominant opening discharge coefficients. The dominant opening inertial and discharge coefficients varied with the sizes of dominant opening area and internal volume. The range of dominant opening inertial coefficients was larger than the theoretical value of 0.89. The range of discharge coefficients for the dominant opening was less than the steady flow value of 0.61. Further experiments on the flow through dominant openings were conducted using a pressure loading actuator. The results show that when the flow through an opening reverses (i.e.) changes direction, the discharge coefficient is significantly reduced.

# Table of Contents

Acknowledgements .....	i
Abstract .....	ii
List of Figures.....	v
List of Tables .....	ix
1 Introduction .....	1
1.1 Objectives.....	2
1.2 Overview .....	2
2 Literature Review .....	4
2.1 Discharge Coefficient.....	7
2.2 Inertial Coefficient .....	10
2.3 Chapter Summary.....	11
3 Theory .....	13
3.1 Building Porosity .....	14
3.2 Dimensional Analysis .....	15
3.3 Discharge Coefficient.....	16
3.4 Inertial Coefficient .....	17
4 Wind Tunnel Methodology and Results.....	19
4.1 Experimental Setup .....	19
4.2 Wind Tunnel Specifications .....	19
4.2.1 Wind Tunnel Model .....	21
4.2.2 Numerical Model.....	25
4.3 Results and Discussion.....	25
4.3.1 Sealed Building .....	25
4.3.2 Internal Pressure Simulation.....	31
4.3.3 Linearization of the Governing Equation .....	41
4.3.4 Porous Building.....	43
4.3.5 Internal Pressure Simulation.....	51
5 Flow Characteristics across an Opening.....	57

5.1	Experimental Setup .....	57
5.2	Results and Discussion.....	59
6	Conclusions .....	65
6.1	Recommendations for Future Work.....	67
7	References .....	68
8	Appendix A – Additional Tables.....	72
9	Appendix B – Additional Figures .....	74

## List of Figures

Figure 3-1: Location of the vena contracta for a freely flowing fluid.....	17
Figure 3-2: Effective length of an air “slug” oscillating at the opening of a building .....	18
Figure 4-1: Wind tunnel profiles for Terrain Category 2 compared to AS/NZS1170.2 profiles	20
Figure 4-2: Velocity spectrum of approaching wind at roof height (100mm) .....	20
Figure 4-3: Scale model with dimensions 400mm x 200mm x 100mm with a 600mm extension below the wind tunnel floor (All dimensions presented in mm) .....	21
Figure 4-4: Location of 1.5mm and 3mm hole diameter, $d$ of porosity for the wind tunnel model (All dimensions are presented in mm).....	22
Figure 4-5: Areas A1 to A4 and locations of the external pressure taps used for area averaging (All units presented in mm) .....	23
Figure 4-6: Ratio of measured mean internal to external pressure coefficient versus $S^*$ .....	26
Figure 4-7: Internal pressure spectra for a) volume V1, b) volume V3, c) volume V5 and d) volume V7 with varying dominant opening areas A1 , A2, A3 and A4.....	29
Figure 4-8: Measured ratio of internal to external pressure standard deviation versus $S^*$ and $\phi_5$ with area configurations shown in brackets.....	30
Figure 4-9: Measured ratio of peak internal to external pressure versus $S^*$ and $\phi_5$ with area configurations shown in brackets .....	31
Figure 4-10: Measured external and internal and simulated internal pressure spectra for opening area A1 and volume V1 using $k = 0.3$ and $CI = 0.89$ for simulations.....	32
Figure 4-11: Measured external and internal and simulated internal pressure spectra for opening area A1 and volume V3 using $k = 0.2$ and $CI = 1.7$ for simulations.....	32
Figure 4-12: Measured external and internal and simulated internal pressure spectra for opening area A1 and volume V5 using $k = 0.25$ and $CI = 1.15$ for simulations.....	33
Figure 4-13: Measured external and internal and simulated internal pressure spectra for opening area A1 and volume V7 using $k = 0.4$ and $CI = 0.9$ for simulations.....	33

Figure 4-14: Measured external and internal and simulated internal pressure spectra for opening area A2 and volume V1 using $k = 0.11$ and $CI = 1.0$ for simulations.....	34
Figure 4-15: Measured external and internal and simulated internal pressure spectra for opening area A2 and volume V3 using $k = 0.15$ and $CI = 2.2$ for simulations.....	34
Figure 4-16: Measured external and internal and simulated internal pressure spectra for opening area A2 and volume V5 using $k = 0.25$ and $CI = 1.4$ for simulations.....	35
Figure 4-17: Measured external and internal and simulated internal pressure spectra for opening area A2 and volume V7 using $k = 0.35$ and $CI = 1.15$ for simulations.....	35
Figure 4-18: Measured external and internal and simulated internal pressure spectra for opening area A3 and volume V1 using $k = 0.07$ and $CI = 1.1$ for simulations.....	36
Figure 4-19: Measured external and internal and simulated internal pressure spectra for opening area A3 and volume V3 using $k = 0.07$ and $CI = 3.0$ for simulations.....	36
Figure 4-20: Measured external and internal and simulated internal pressure spectra for opening area A3 and volume V5 using $k = 0.13$ and $CI = 1.8$ for simulations.....	37
Figure 4-21: Measured external and internal and simulated internal pressure spectra for opening area A3 and volume V7 using $k = 0.2$ and $CI = 1.5$ for simulations.....	37
Figure 4-22: Measured external and internal and simulated internal pressure spectra for opening area A4 and volume V1 using $k = 0.04$ and $CI = 1.3$ for simulations.....	38
Figure 4-23: Measured external and internal and simulated internal pressure spectra for opening area A4 and volume V3 using $k = 0.04$ and $CI = 3.4$ for simulations.....	38
Figure 4-24: Measured external and internal and simulated internal pressure spectra for opening area A4 and volume V5 using $k = 0.1$ and $CI = 2.1$ for simulations.....	39
Figure 4-25: Measured external and internal and simulated internal pressure spectra for opening area A4 and volume V7 using $k = 0.15$ and $CI = 1.6$ for simulations.....	39
Figure 4-26: Discharge coefficient $k$ , versus $S^*$ , estimated from numerical simulations.....	40
Figure 4-27: Inertial coefficient $CI$ versus $S^*$ , estimated from numerical simulations.....	41

Figure 4-28: Discharge coefficient $k$ , versus $S^*$ , estimated by linearizing the governing equation using Vickery and Bloxham method.....	42
Figure 4-29: Ratio of internal and external mean pressure coefficients to $\phi_6$ .....	43
Figure 4-30: Measured external and internal pressure spectra for varying $\phi_6$ values of 0 (P1), 0.28 (P2), 0.95 (P3) and 1.24 (P4) for area A1 and volumes V3, V5 and V7 .....	45
Figure 4-31: Measured external and internal pressure spectra for varying $\phi_6$ values of 0 (P1), 0.09 (P2), 0.31 (P3) and 0.40 (P4) for area A2 and volumes V3, V5 and V7 .....	47
Figure 4-32: Measured external and internal pressure spectra for varying $\phi_6$ values of 0 (P1), 0.05 (P2), 0.15 (P3) and 0.20 (P4) for area A3 and volumes V3, V5 and V7 .....	48
Figure 4-33: Measured external and internal pressure spectra for varying $\phi_6$ values of 0 (P1), 0.03 (P2), 0.10 (P3) and 0.12 (P4) for area A4 and volumes V3, V5 and V7 .....	50
Figure 4-34: Ratio of internal and external pressure standard deviation to $S^*$ for varying $\phi_6$ ..	51
Figure 4-35: Ratio of internal and external peak pressure coefficient to $S^*$ for varying $\phi_6$ .....	51
Figure 4-36: Area A2 and internal volume V7 for porosities with a constant $k$ and varying $kL'$	53
Figure 4-37: Area A4 and internal volume V7 for porosities with opening $k = 0.15$ and varying $kL'$ .....	54
Figure 4-38: Discharge coefficient for background porosity $kL'$ with increasing $S^*$ .....	55
Figure 4-39: Discharge coefficient for background porosity $kL'$ versus dominant opening discharge coefficient $k$ .....	56
Figure 5-1: Setup for measuring the discharge coefficient, with the opening shown in the pressure chamber and arrows indicating positive flow direction .....	58
Figure 5-2: Sharp edged, 56mm diameter, d circular opening .....	59
Figure 5-3: 6mm thickness, 50mm $\times$ 50mm square opening .....	59
Figure 5-4: Sample net pressure across the dominant opening time history trace .....	60
Figure 9-1: Area A1 and internal volume V3 for porosities with a constant $k$ and varying $kL'$ .	75
Figure 9-2: Area A1 and internal volume V5 for porosities with a constant $k$ and varying $kL'$ .	76
Figure 9-3: Area A1 and internal volume V7 for porosities with a constant $k$ and varying $kL'$ .	78

- Figure 9-4: Area A2 and internal volume V3 for porosities with a constant  $k$  and varying  $kL'$ . 79
- Figure 9-5: Area A2 and internal volume V5 for porosities with a constant  $k$  and varying  $kL'$ . 81
- Figure 9-6: Area A3 and internal volume V3 for porosities with a constant  $k$  and varying  $kL'$ . 82
- Figure 9-7: Area A3 and internal volume V5 for porosities with a constant  $k$  and varying  $kL'$ . 84
- Figure 9-8: Area A3 and internal volume V7 for porosities with a constant  $k$  and varying  $kL'$ . 85
- Figure 9-9: Area A4 and internal volume V3 for porosities with a constant  $k$  and varying  $kL'$ . 87
- Figure 9-10: Area A4 and internal volume V5 for porosities with a constant  $k$  and varying  $kL'$ . 88

## List of Tables

Table 2-1: Summary of discharge coefficients and loss coefficient from various studies.....	10
Table 2-2: Summary of estimated inertial coefficients and where applicable, adjusted inertial coefficients .....	11
Table 4-1: Test configurations opening and volume sizes, $S^*$ , leakage area $AL$ with $\phi 5$ and $\phi 6$ .....	24
Table 5-1: Discharge coefficients under steady pressure for various opening configurations....	61
Table 5-2: Discharge coefficients under unidirectional, sinusoidal flow for varying amplitudes, frequencies and opening configurations.....	62
Table 5-3: Discharge coefficients under reversing flow, sinusoidal flow with varying opening areas and frequencies .....	63
Table 8-1: Measured area averaged external pressure coefficients for dominant opening sizes A1, A2, A3 and A4 .....	72
Table 8-2: Measured internal pressure coefficients for dominant opening sizes A1, A2, A3 and A4 with internal volumes V1, V2, V3 and V4.....	72
Table 8-3: Dominant opening and internal volume sizes, Helmholtz Frequency with $S^*$ and $\phi 5$ .....	73
Table 8-4: Ratios of measured internal and external pressure coefficients for varying opening areas and internal volume sizes.....	73

# 1 Introduction

Wind driven pressures inside a building are generated by the external pressures acting on a building envelope and the flow paths through openings that connect the internal volume to the outside. The effective internal volume, and the size and location of openings will also influence the magnitude of internal pressures. The combined external and internal pressure actions create net pressures acting across building surfaces. Net pressures on the building envelope drives natural ventilation, allows water ingress, and must be considered for designing cladding and structural systems of buildings.

A building that is nominally sealed has smaller internal pressure relative to the external pressure due to the small opening areas. However, a dominant opening will produce large internal pressures and is a structural design criterion for wind loading. The windward dominant opening case is generally the most critical design scenario. Dominant openings typically occur due to failures of windows and doors during windstorms or windborne debris impact. When windstorms occur with little warning (ie. thunderstorms), doors and windows left open during the event can become dominant openings. Dominant openings that cause large internal pressures leading to wind induced structural failures are observed in damage investigations after windstorms (Boughton et al, 2012, Leitch et al, 2009 and Henderson et al, 2006).

Wind loading standards and codes (AS/NZS 1170.2, 2011 and ASCE7-10, 2010) specify a quasi-static internal pressure coefficient, that is based on the external pressure coefficients at the dominant opening. Allowances for reducing internal pressure for design are possible for increasing building envelope permeability or large internal volumes (ASCE7-10, 2010). The Australia and New Zealand Wind Loading Standard (AS/NZS 1170.2, 2011) requires closed doors and windows to be considered as dominant openings, unless shown that they are capable of withstanding design wind pressures and debris impact loads.

A number of studies since the mid 1970s have analysed internal pressure dynamics. The studies showed that a Helmholtz resonator model can be used to represent a building with a

dominant opening. The Helmholtz resonance in a building with a dominant opening can also influence the internal pressure characteristics. The key parameters that affect internal pressure dynamics are: size of the opening, size of the volume, porosity and flexibility of the envelope, velocity and turbulence of the approaching flow and the flow characteristics through an opening (i.e. discharge coefficient and inertial coefficient).

## **1.1 Objectives**

This thesis aims to further define the Helmholtz resonance effect in buildings through the study of the key parameters. Therefore, the objectives are twofold: 1) to determine the effects of varying dominant opening areas and internal volume sizes on the characteristics of internal pressures, including mean and standard deviation, and 2) to determine the effect of increasing leeward background porosity on internal pressure characteristics.

These objectives will be met by developing an analytical method and numerical simulations which will be complimented by a series of wind tunnel model tests and a series of basic experiments measuring the flow characteristics through openings.

## **1.2 Overview**

The second chapter presents a review of the current state of knowledge of internal pressure studies and the relevant parameters that influence their fluctuations. The review includes a summary of discharge coefficients and inertial coefficients for air flow through openings, used by previous studies. Chapter three presents the theory of internal pressure with the incorporation of background porosity into the governing equation. The governing equation is provided in non-dimensional format. Chapter three also includes theoretical concepts for the discharge coefficient from a fluid mechanics context and the inertial coefficient from Helmholtz resonator theory.

Chapter four describes the experimental set-up in the boundary layer wind tunnel and numerical modelling used to study internal pressure with varying opening areas and internal volume with a range of background porosity. The chapter also includes the experimental set-up

used to determine the flow characteristics (i.e. discharge coefficients) across dominant openings. This leads into the fifth chapter which presents and discusses the wind tunnel experiment and numerical simulation results, as well as the results and discussion of the flow across openings. The sixth and final chapter concludes the thesis by summarizing the study and highlighting the major findings.

## 2 Literature Review

Using the concept of mass continuity, Liu and Saathoff (1981) analytically estimated the flow through a building with multiple openings. They showed that the mean internal pressure is a function of the mean external pressures and the size of the area at each opening. Their analytical solution was validated by wind tunnel experiments and is the basis for determining internal pressures in wind loading standards and codes (AS/NZS 1170.2, 2011 and ASCE 7, 2010). The mean internal pressure in a building with a dominant opening and no porosity is equal to the mean external pressure at the opening (Liu, 1975).

The dynamic response of internal pressures was first investigated by Holmes (1979). His study showed that a building with a single dominant opening acts as a Helmholtz resonator, a well known topic in acoustics. The governing equation that describes the variation of internal pressure with time,  $t$  is shown in Equation 2-1. Equation 2-1 represents the internal pressure,  $p_i$  in a building, generated by a “slug” of air oscillating in and out of the opening. The external pressure at the opening is denoted by  $p_e$ . Holmes also identified several key parameters that influence the magnitude of the Helmholtz resonance, as the opening area size  $A_o$ , effective internal volume size  $V_o$ , discharge coefficient  $k$ , inertial coefficient  $C_I$ , speed of sound,  $a_s$  and air density,  $\rho$ .

$$\frac{C_I V_o}{a_s^2 \sqrt{A_o}} \ddot{p}_i + \frac{1}{2\rho} \left( \frac{V_o}{a_s^2 k A_o} \right)^2 \dot{p}_i |\dot{p}_i| + p_i = p_e \quad \text{Equation 2-1}$$

Vickery (1986) derived the same governing equation as Holmes (1979) by using the unsteady flow equation. Liu and Saathoff (1981) arrived at another version of the governing equation using the unsteady Bernoulli equation. Their governing equation was heuristically modified to account for contraction of flow at the opening. Vickery (1991) showed that the flow contraction appears in Liu and Saathoff’s equation because the integration limits end at the opening instead of inside the building volume. Similarly, Sharma and Richards (1997b) use a

variation of Liu and Saathoff's equation, by adopting the contraction coefficient on the “slug” of air and using an independent loss coefficient to account for damping in the system. It is worth noting that the same solution can be found using the three different governing equations. For the purpose of this study, the more commonly used governing equation described by Holmes (1979) and Vickery (1986) is adopted (Holmes and Ginger, 2012).

Yu et al (2006) represented the opening area, internal volume, speed of sound and mean wind speed at roof height  $\bar{U}_h$  as a non-dimensional parameter,  $S = (a_s^2/\bar{C}_{pw}\bar{U}_h^2)^{2/3} \times A_o/V_o^{2/3}$ . This means that a unique solution for internal pressure fluctuations can be determined with  $S$ , if the discharge characteristics are known. Ginger et al (2008) simplified the governing equation by using  $S^* = (A_o^{3/2}/V_o) \times (a_s/\bar{U}_h)^2$ . This format facilitates the incorporation of internal pressure dynamics into a format compatible with wind loading standards (Holmes and Ginger, 2012) and is adopted in this study.

Holmes (1979; 2009) showed that similarity needs to be maintained to satisfy internal pressure fluctuations in a wind tunnel model study. Scaling can be achieved by distorting the volume ratio by  $[V_o]_r = [L]_r^3/[U]_r^2$ . Here,  $[L]_r$  is the length ratio and  $[U]_r$ , is the velocity ratio between full scale and model scale. A subsequent study by Sharma et al (2010) showed that volume distortions of a uniform cavity in wind tunnel experiments with geometric discontinuity in the internal volume, could behave as multiple Helmholtz resonators. Therefore, maintaining a uniform cavity for each room is required for internal pressure wind tunnel testing.

A flexible building envelope will cause the internal volume to vary with fluctuations in the internal pressure. Vickery (1986) showed that the influence of this effect on internal pressure, can be accounted for by increasing the nominal volume,  $V_o$  by a factor of  $K_A/K_B$ . This gives an effective volume  $V_e = V_o(1 + K_A/K_B)$ . Here,  $K_A$  is the bulk modulus of air and  $K_B$  is the bulk modulus of the structure. The bulk modulus of the structure is the relationship between the change in internal volume with the change in internal pressure. Ginger et al (1997) confirmed Vickery's analytical model by estimating the flexibility at full-scale of the WERFL

building at Texas Tech University. Pearce and Sykes (1999) tested a series of flexible roof structures in the wind tunnel and also concluded that using an effective volume was satisfactory in describing the internal pressure response of buildings with a flexible envelope.

In buildings without large openings, the external pressure affects the internal pressure by enabling air flow in and out of the building through the porosity in its envelope. The amount of porosity in a building can vary extensively based on the building's function and location. For example, a shed has higher envelope porosity than a high rise building, and tropical houses will allow greater natural ventilation than houses in temperate climates.

Vickery (1986) and Vickery and Bloxham (1992) showed that the inertia of the air flow through background porosity can be ignored because it is orders of magnitude smaller than the damping caused by air flowing through porous openings. They also showed that instead of treating each porous opening independently, it was acceptable to represent the sum of the porous areas by a single effective lumped porous area.

The background porosity can attenuate internal pressure in a building with a dominant opening. Vickery and Bloxham (1992) showed that internal pressure fluctuations are attenuated when the background porosity area exceeds 10% of the dominant opening area. As the background porosity increases to 30% of the dominant opening area, the mean internal pressure will be significantly reduced. Woods and Blackmore (1995) and Yu et al (2008) also studied internal pressures in buildings using a lumped background porosity term and varying dominant opening areas and found that as the ratio of the porous area to dominant opening area increases, the mean internal pressure is reduced.

Guha et al (2009) developed a numerical model incorporating the background porosity into the governing equation to numerically estimate the effects of porosity on internal pressure. The governing equation with background porosity was linearised by Guha et al (2011a). The study found that a lumped leeward opening was a reasonable assumption for buildings with background porosities up to nominally 10%. Guha et al (2011b) have also performed full scale

monitoring on a shed and found the Helmholtz peak to be damped due to the high levels of porosity in the structure.

Oh et al (2004) developed a numerical model that treated each porous opening individually, using the power law equation, suggested by Shaw (1981). The power law assumes that the flow through porous openings is similar to laminar flow in a pipe.

## **2.1 Discharge Coefficient**

The discharge coefficient for airflow through building envelopes has been studied extensively. However, detailed studies on the discharge coefficient for flow in and out of a dominant opening have been limited in their scope.

For a steady flow through a sharp edged opening, connecting two infinitely large volumes, the discharge coefficient,  $k$  is equal to 0.61 (Rouse, 1961). The discharge coefficient can also be represented as a loss coefficient  $C_L$ , where  $C_L = 1/k^2$ . Vickery (1991) has stated that it is unlikely that that steady flow discharge coefficients would be applicable for the dominant opening scenario, where highly turbulent wind pressure causes air flow to move in and out of a building.

Many building ventilation studies have analysed the discharge coefficients by considering the effects of parameters such as the opening area geometry, opening depth, building porosity, approaching wind direction, turbulence intensity and Reynolds number. Karava et al (2005) published a review paper summarising the effects of these parameters, which showed a large variation of the discharge coefficients between studies. They concluded that it was not possible to establish a generalized discharge coefficient and recommended that a unique discharge coefficient be selected for a given configuration.

Vickery and Karakatsanis (1987) estimated the discharge coefficient for unidirectional steady flow with low turbulence by measuring the flow through a range of opening configurations in a building model using a wind tunnel. They found that for Reynolds numbers

greater than about 3000, the discharge coefficient is nominally constant at 0.7. For Reynolds numbers less than 3000, the discharge coefficient ranges from 0.37 to 0.7. The Reynolds number was defined as  $Re = \bar{U}\sqrt{A_o}/\nu$ , where  $\nu$  is the kinematic viscosity of air and  $\bar{U}$  is the mean velocity at the opening.

As shown in the governing Equation 2-1, air flow through a dominant opening and the internal pressure fluctuations are affected by the discharge coefficient,  $k$ . Many studies apply  $k = 0.6$  when analysing the pressure inside a building with a dominant opening. Values for  $k$  can be obtained by matching numerical simulations using Equation 2-1 with experimental results.

Holmes (1979) obtained a  $k$  value of 0.15 for a dominant opening in a wind tunnel model by comparing wind tunnel results with a numerical simulation. The lower discharge coefficient was attributed to the unsteady highly fluctuating and the reversing flow of the wind through the dominant opening caused by Helmholtz resonance. Ginger (2000) estimated the discharge coefficient for a full scale porous and flexible structure in turbulent flow to be 0.15 for a 5% opening area and 0.35 for a 2% opening area. Using similar methods of spectra matching, Yu et al. (2006) and Oh et al. (2007) estimated the discharge coefficient to be 0.37 and 0.63 respectively.

An alternative method of defining the discharge coefficient was presented by Sharma and Richards (1997b), which applies a contraction coefficient  $C_c$ , to the opening area  $A_o$ , in the inertial term and an independent loss coefficient  $C_L$  in the damping term of Equation 2-1. In this case,  $C_L$  includes all losses in the system and is defined as an effective loss coefficient with a value of 1.2 for the configurations tested by Sharma (2010). The  $C_c$  was empirically identified using computational fluid dynamics when a contraction was qualitatively observed at the orifice. While the actual magnitude of the contraction on the area was not physically measured, a value of 0.6 was heuristically matched using wind tunnel experiments and numerical simulations.

Few studies have examined the reversing flow condition and its effect on the discharge coefficient. Etheridge (2000) and Costola and Etheridge (2008) have studied the effects of changing flow direction on discharge coefficients for chimney stacks. However, the forward and reversing directions were considered independently and essentially treated as unidirectional. A study by Chaplin et al (2000) applied a sinusoidal reversing flow to a volume. The discharge coefficient was calculated explicitly by linearising the governing equation. The results showed that the mean discharge coefficients generally matched the steady flow theory for large openings but did not match for smaller openings.

Oh et al. (2007) and Holmes and Ginger (2012) have both presented useful summaries of discharge coefficients assumed or derived in various studies. The summary showed that  $k$  has been estimated to be in the range of 0.15 to 1.0. In the majority of studies, the discharge coefficient is determined by matching of the measured internal pressure spectrum with the spectrum of internal pressure obtained from numerical models of Equation 2-1. Table 2-1 shows a summary of discharge coefficients and loss coefficients estimated by various researchers with  $S^*$  (if known).

Table 2-1: Summary of discharge coefficients and loss coefficient from various studies

Study	$S^*$	Estimated Discharge Coefficient $k$	Estimated Loss Coefficient $C_L$	Comments
Holmes (1979)	0.015	0.15	44	Scale model of a house model. Spectra matching.
Vickery and Karakatsanis (1987)	-	0.38 to 0.7	2.0 to 6.9	Unidirectional steady flow. $k$ measured directly
Vickery and Bloxham (1992)	0.0185	1.0	1.0	Spectra matching.
Vickery (1994)	Unknown	0.61	2.7	Assumed
Sharma and Richards (1997a)	Unknown	0.9	1.2	$U_h$ unknown. Spectra matching.
Sharma and Richards (1997b)	0	0.75	1.8	Helmholtz resonance determined by tapping flexible wall. Therefore, $U_h = 0$ m/s. Spectra matching.
Ginger et al (1997)	0.082 and 0.021	0.15 and 0.35	8 to 44	Full scale. Spectra matching.
Chaplain et al (2000)	-	0.67 to 1.15	0.75 to 2.2	Reversing flow. Linearised equation.
Sharma and Richards (2003)	0.26 to 0.37	0.6	2.7	Oblique wind directions.
Yu et al (2006)	0.17 to 10.63	0.37	7.3	Spectra matching. Assumed to be constant for all configurations.
Oh et al (2007)	0.0001 to 0.008	0.63	2.5	Spectra matching.

## 2.2 Inertial Coefficient

The effective length,  $l_e$  is the estimated length of an air “slug” oscillating in and out of an opening of a Helmholtz resonator and is given by  $l_e = C_I \sqrt{A_o}$  for very thin opening thicknesses. Few studies have assessed the inertial coefficient,  $C_I$  for internal pressure applications. Most studies have typically assumed the inertial coefficient to be a constant of 0.89, taken from Helmholtz resonator theory (Rayleigh, 1945). However, Vickery (1986) has stated that the inertial coefficient can vary from 0.89 to 2.0.

The inertial coefficient can be estimated by matching the Helmholtz frequencies between experimental and numerical simulations of Equation 2-1. Several researchers have adjusted other parameters in Equation 2-1 to match Helmholtz frequencies while keeping the inertial coefficient constant. For example, Holmes (1979) adjusted the polytropic exponent,  $n$

from 1.4 to 1.2, Liu and Rhee (1986) and Sharma and Richards (1997b) used a contraction coefficient in the inertial term to match the Helmholtz frequency with measured values. Vickery (1991) stated that the flow conditions for Helmholtz resonator theory are not applicable for internal pressure applications and therefore the assumed constant value for the inertial coefficient is not valid and should be adjusted. Table 2-2 presents inertial coefficients determined in various studies that indicate the parameters that were varied (if any) and presents the “effective” inertial coefficient used in Equation 2-1 to match the measured values.

Table 2-2: Summary of estimated inertial coefficients and where applicable, adjusted inertial coefficients

Study	Assumed Inertial Coefficient $C_I$	Altered Factor	Adjusted Inertial Coefficient $C_I$
Holmes (1979)	0.89	$n = 1.2$	1.04
Liu and Rhee (1986)	0.89	$C_C = 0.6$ on area	1.01
Vickery and Bloxham (1992)	-	-	1.1 to 1.6
Vickery (1994)	0.89	-	0.89
Sharma and Richards (1997a)	0.66	$C_C = 0.6$ on area	1.1
Sharma and Richards (1997b)	0.63	$C_C = 0.6$ on area	1.04
Ginger et al (1997)	0.89	-	0.89
Chaplin et al (2000)	-	-	-26 to 1.39
Sharma and Richards (2003)	0.78	$C_C = 0.6$ on area	1.3
Yu et al (2006)	1.3	$C_C = 1.0$ on area	1.3
Oh et al (2007)	0.89	-	0.89

## 2.3 Chapter Summary

A building with a dominant opening can be represented as a Helmholtz resonator, where the external pressure fluctuations act as the forcing function. The Helmholtz resonator phenomenon contributes significantly to the internal pressure fluctuations in a building. The internal pressure fluctuations can be represented with respect to the opening area size and internal volume size relationship,  $S^*$ . A comprehensive study of the effects of a range of  $S^*$  on internal pressure fluctuations are performed in this project. Internal pressure characteristics are attenuated by increasing levels of background building porosity. The background porosity can be represented as the sum of the porous openings as a single lumped porous opening in the analysis.

Studies on the discharge and inertial coefficients for internal pressures in buildings are limited. Previous studies show that a wide range of discharge coefficients (between 0.15 and 1.15) and inertial coefficients (between 0.89 and 1.6) have been estimated. Further research into discharge and inertial coefficients is required to explain the large range in these values.

### 3 Theory

The unsteady, incompressible flow through an opening can be described using the unsteady discharge equation shown in Equation 3-1 (Vickery, 1986). The area averaged velocity,  $U_o$  is related to the flow through the opening,  $Q$  and opening area,  $A_o$  by  $U_o = Q/A_o$  and the acceleration of the flow is  $\dot{U}_o$ . The flow is driven by the pressure difference across the opening,  $\Delta p$ . The loss coefficient and the inertial coefficient are  $C_L$  and  $C_I$  respectively.

$$\Delta p = \frac{1}{2} \rho C_L U_o^2 + \rho C_I \sqrt{A_o} \dot{U}_o \quad \text{Equation 3-1}$$

Applying principles of mass conservation, where the flow into a building equals the flow out of the building, Liu (1975) showed that the mean internal pressure in a building is dependent on the pressure acting on the windward and leeward openings, and the sizes and discharge characteristics of the corresponding openings. The mean internal pressure is represented by Equation 3-2 in terms of pressure coefficients,  $C_p$  where  $C_p = p/(1/2 \rho \bar{U}_h^2)$ . Here,  $\rho$  is the density of air and  $\bar{U}_h$  is the mean wind speed at roof height,  $h$ . Windward and leeward opening areas and pressures are denoted by the subscript  $W$  and  $L$ , respectively. From Equation 3-2, it can be shown that for a building with a single windward dominant opening (i.e.  $A_L = 0$ ) that the mean internal pressure is equal to the mean windward external pressure.

$$\bar{C}_{pi} = \frac{\bar{C}_{pW}}{1 + \left(\frac{A_L}{A_W}\right)^2} + \frac{\bar{C}_{pL}}{1 + \left(\frac{A_W}{A_L}\right)^2} \quad \text{Equation 3-2}$$

Assuming the cavity of a building with a single dominant opening behaves as a Helmholtz resonator (Holmes, 1979), the internal pressure fluctuations can be expressed by Equation 3-3. Here, the first term describes the inertia of a “slug” of air by its effective length,  $l_e$  and the speed of sound can be expressed as  $a_s = \sqrt{n \times p_o / \rho}$ , where  $p_o$  is the atmospheric pressure and  $n$  is the polytropic exponent. The undamped Helmholtz frequency  $f_H$ , is  $f_H = \frac{1}{2\pi} \sqrt{a_s^2 A_o / (l_e V_e)}$ , where  $V_e$  is the effective internal volume.

$$\frac{l_e V_e}{a_s^2 A_o} \ddot{C}_{pi} + \left( \frac{V_e \bar{U}_h}{2a_s^2 k A_o} \right)^2 \dot{C}_{pi} |\dot{C}_{pi}| + C_{pi} = C_{pW} \quad \text{Equation 3-3}$$

### 3.1 Building Porosity

The pressure drop through porous openings in a building can also be represented by Equation 3-1. Ignoring inertial effects and assuming a lumped porous opening, the turbulent flow through porous openings can be represented by a single discharge equation in Equation 3-4.

$$p_i - \bar{p}_L = \frac{1}{2} \rho C'_L U_L^2 \quad \text{Equation 3-4}$$

Here  $\bar{p}_L$  is the mean external pressure acting on the porous surfaces,  $U_L$  is the area averaged velocity through the lumped porous opening and  $C'_L$  is the effective loss coefficient and can be related to an effective discharge coefficient  $k'_L$ , by  $C'_L = (1/k'_L)^2$ . The governing equation of internal pressure with a windward dominant opening  $A_o$ , including a lumped porous opening,  $A_L$  is given in Equation 3-5. The external pressure acting on the opening is given by its coefficient  $C_{pW}$ . When a building has no porosity (i.e. when  $A_L = 0$ ), Equation 3-5 reduces to Equation 3-3. This was also shown by Yu et al (2008) and Guha et al (2011a).

$$\begin{aligned} \frac{l_e V_e}{a_s^2 A_W} \ddot{C}_{pi} + \frac{k'_L l_e A_L}{U_h A_W} \cdot \frac{\dot{C}_{pi}}{\sqrt{(C_{pi} - \bar{C}_{pL})}} + \frac{\rho^2 U_h^2 V_e^2}{4k^2 n^2 p_i^2 A_W^2} \\ \cdot \left( \frac{2k'_L A_L n p_i}{V_e \rho U_h} \cdot \sqrt{(C_{pi} - \bar{C}_{pL})} + \dot{C}_{pi} \right) \\ \cdot \left| \frac{2k'_L A_L n p_i}{V_e \rho U_h} \cdot \sqrt{(C_{pi} - \bar{C}_{pL})} + \dot{C}_{pi} \right| + C_{pi} = C_{pW} \end{aligned} \quad \text{Equation 3-5}$$

### 3.2 Dimensional Analysis

Using dimensional analysis, Holmes (1979) rearranged Equation 3-3 into five non-dimensional parameters to represent the fluctuating internal pressure coefficient  $C_{\sigma pi}$  (Equation 3-6).

$$C_{\sigma pi} = f(\phi_1, \phi_2, \phi_3, \phi_4, \phi_5) \quad \text{Equation 3-6}$$

The five non-dimensional parameters are:

$$\phi_1 = \frac{A_o^{3/2}}{V_e}, \phi_2 = \frac{a_s}{\bar{U}_h}, \phi_3 = \frac{\rho \bar{U}_h \sqrt{A_o}}{\mu}, \phi_4 = \frac{\sigma_u}{\bar{U}}, \phi_5 = \frac{\lambda_u}{\sqrt{A_o}}$$

Here  $\mu$  is viscosity of air and  $\lambda_u$  is the integral length scale of turbulence. By including a dimensionless time parameter  $t^* = t\bar{U}_h/\lambda_u$ , Equation 3-3 can be expressed in non-dimensional format (Equation 3-7).

$$\frac{C_I}{\phi_1 \phi_2^2 \phi_5^2} \ddot{C}_{pi} + \frac{1}{4k^2} \left( \frac{1}{\phi_1 \phi_2^2 \phi_5} \right)^2 \dot{C}_{pi} |\dot{C}_{pi}| + C_{pi} = C_{pW} \quad \text{Equation 3-7}$$

The  $\phi_1 \phi_2^2$  parameters in the first and second terms of Equation 3-7 can be replaced by the non-dimensional parameter  $S^*$ , where  $S^* = (A_o^{3/2}/V_e) \times (a_s/\bar{U}_h)^2$  as shown by Ginger et al (2008). Equation 3-8 shows the governing equation in non-dimensional  $S^*$  format. This implies that internal pressure fluctuations depend on the size of the opening area with respect to the size of the internal volume, and that there is a unique solution for  $C_{pi}$  for a given  $S^*$  and  $\phi_5$ , if  $k$  and  $C_I$  are known.

$$\frac{C_I}{S^* \phi_5^2} \ddot{C}_{pi} + \left( \frac{1}{4k^2} \right) \left( \frac{1}{S^* \phi_5} \right)^2 \dot{C}_{pi} |\dot{C}_{pi}| + C_{pi} = C_{pW} \quad \text{Equation 3-8}$$

A building with a dominant opening and background porosity can be represented in a non-dimensional format by the addition of a sixth non-dimensional parameter  $\phi_6 = A_L/A_W$ . Equation 3-2 and Equation 3-5 can be represented in non-dimensional format shown in Equation 3-9 and Equation 3-10 respectively. Equation 3-10 is the governing equation that is

used for this study. It can be shown that when  $\phi_6 = 0$  (i.e. no background porous openings), the governing equation is equivalent to Equation 3-8.

$$\bar{C}_{pi} = \frac{\bar{C}_{pW}}{1 + (\phi_6)^2} + \frac{\bar{C}_{pL}}{1 + \left(\frac{1}{\phi_6}\right)^2} \quad \text{Equation 3-9}$$

$$\begin{aligned} \frac{C_I}{S^* \phi_5^2} \ddot{C}_{pi} + k'_L \frac{\phi_6}{\phi_5} \frac{C_I}{\sqrt{(C_{pi} - \bar{C}_{pL})}} \dot{C}_{pi} + \frac{k'_L{}^2}{k^2} \phi_6^2 (C_{pi} - \bar{C}_{pL}) \\ + \frac{k'_L}{k^2} \frac{\phi_6}{S^* \phi_5} \sqrt{C_{pi} - \bar{C}_{pL}} \dot{C}_{pi} + \left(\frac{1}{4k^2}\right) \left(\frac{1}{S^* \phi_5}\right)^2 \dot{C}_{pi} |\dot{C}_{pi}| + C_{pi} \\ = C_{pW} \end{aligned} \quad \text{Equation 3-10}$$

### 3.3 Discharge Coefficient

The unsteady flow,  $Q$  through an opening,  $A_o$ , driven by a pressure difference  $\Delta p$ , was described by the discharge equation given in Equation 3-1. For the purpose of this study, the discharge coefficient is considered as a time averaged “mean” value. The discharge coefficient for an opening is a function of the velocity coefficient,  $C_v$  and contraction coefficient,  $C_c$  :

$$k = C_c \times C_v \quad \text{Equation 3-11}$$

where,

$$C_c = \frac{\text{area of the vena contracta}}{\text{area of the orifice}} \quad \text{Equation 3-12}$$

$$C_v = \frac{\text{velocity at the vena contracta}}{\text{theoretical velocity}} \quad \text{Equation 3-13}$$

Under steady flow, the vena contracta is the point where the streamlines first become parallel and where the air jet has the smallest area represented in Figure 3-1 at A-A. For steady

flow through a two-dimensional, sharp edged circular orifice connecting two infinitely large volumes, steady flow theory gives  $C_c = \pi/(\pi + 2) \approx 0.61$  and  $C_v \approx 0.99$  or 1 (Rouse, 1959). This gives a discharge coefficient of 0.6 to 0.61.

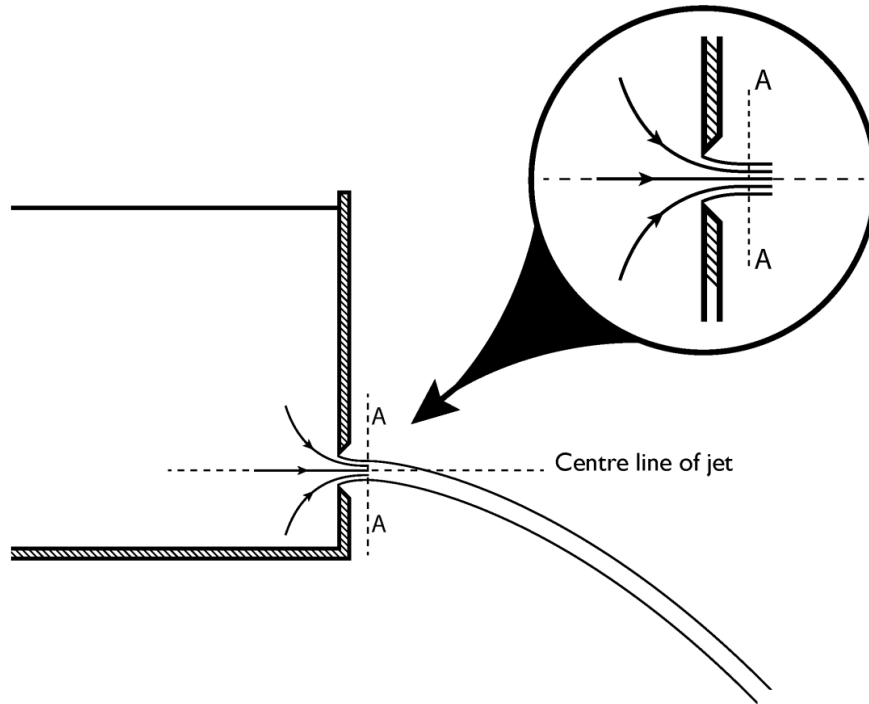


Figure 3-1: Location of the vena contracta for a freely flowing fluid

### 3.4 Inertial Coefficient

The mass of a “slug” of air can be defined by the density and volume of the air “slug”. From Helmholtz resonator theory, the volume of the “slug” can be estimated by the cross sectional area of the orifice and an effective length. The effective length  $l_e$ , is the length of the air “slug” oscillating at an opening and can be expressed as Equation 3-14.

$$l_e = l_o + \Delta l \quad \text{Equation 3-14}$$

Here,  $l_o$  is the length of the opening and  $\Delta l$  is the extended length of the air “slug” beyond the opening. However, when opening lengths are small (i.e. windows and doors),  $l_o$  can be ignored. The extended length represents the oscillating air just outside the opening. Figure 3-2 shows a schematic of a “slug” of air oscillating in a windward dominant opening.

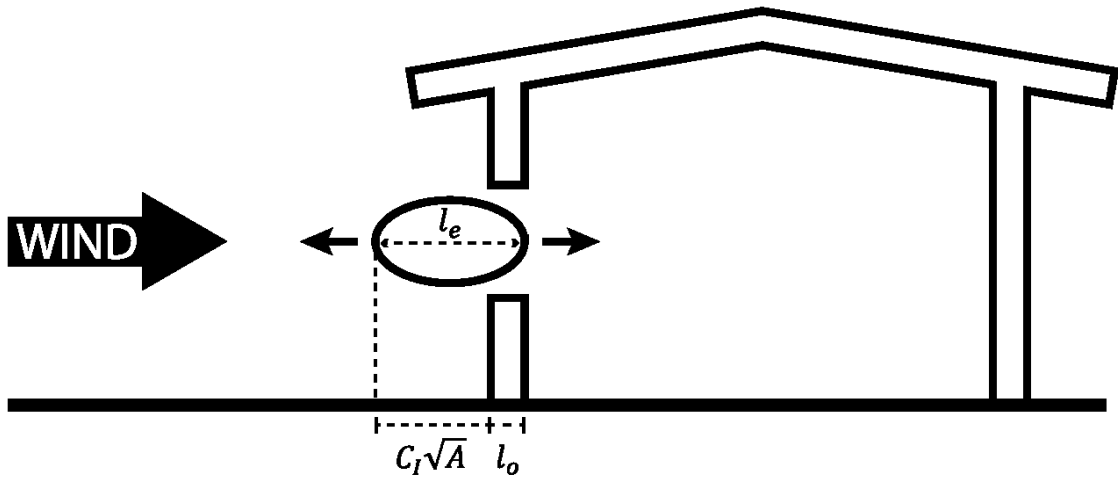


Figure 3-2: Effective length of an air “slug” oscillating at the opening of a building

Rayleigh (1896) estimated the upper and lower bound extended lengths for circular openings in Helmholtz resonators to be  $\Delta l > 0.785r$  and  $\Delta l < 0.849r$ , where  $r$  is the radius of opening.

In practice, dominant openings are typically rectangular. Malecki (1969) provides estimates of  $\Delta l$  for rectangular openings to be  $\Delta l = \frac{1}{2}b\mu$ , where  $b$  is the breadth of the opening and  $\mu$  is a coefficient based on the ratio of the length to breadth. Holmes (1979) and Vickery (1986) found that the best match for internal pressure wind tunnel studies was an extended length using an approximately circular shape given by  $\Delta l = \frac{1}{2}\sqrt{\pi A} = C_l\sqrt{A}$ , where  $C_l = \frac{1}{2}\sqrt{\pi} \approx 0.89$ . When the volume of air is oscillating in a volume with two open ends, such as a tube, the air on both ends of the opening are incorporated multiplying  $\Delta l$  by two.

## 4 Wind Tunnel Methodology and Results

### 4.1 Experimental Setup

A series of scale model wind tunnel tests were performed for this study. The dominant opening external pressure obtained from wind tunnel results were used for numerical simulations. All experiments described herein were performed at the wind tunnel building at the School of Engineering and Physical Sciences, in James Cook University.

### 4.2 Wind Tunnel Specifications

Wind tunnel measurements were carried out in the atmospheric boundary layer wind tunnel at James Cook University with dimensions 2.0m height, 2.5m width and 22.0m length. The atmospheric boundary layer flow was modelled at 1/200 for Terrain Category 2, as defined by AS/NZS 1170.2 (2011). The atmospheric boundary layer was modelled by installing a 250mm trip board at the inlet, immediately followed by a fetch of carpet to simulate terrain roughness. Tests were conducted at a mean reference wind speed of approximately 10 m/s at roof height,  $\bar{U}_h$  (height = 100mm model scale). The mean velocity profile and turbulence intensity profile of the simulated boundary layer flow and the boundary layer profile as defined by Deaves and Harris (1978) are shown in Figure 4-1. The velocity spectrum of the wind speed at roof height is shown in Figure 4-2 and the integral length scale of turbulence  $\lambda_{\text{int}}$ , at roof height was estimated to be 300mm.

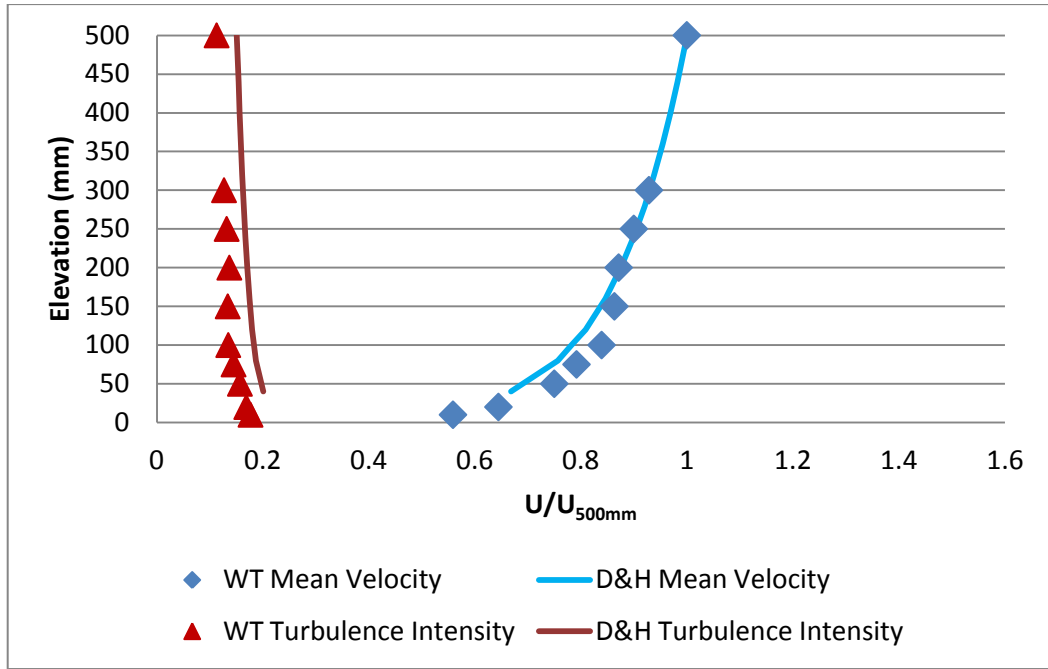


Figure 4-1: Wind tunnel profiles for Terrain Category 2 compared to AS/NZS1170.2 profiles

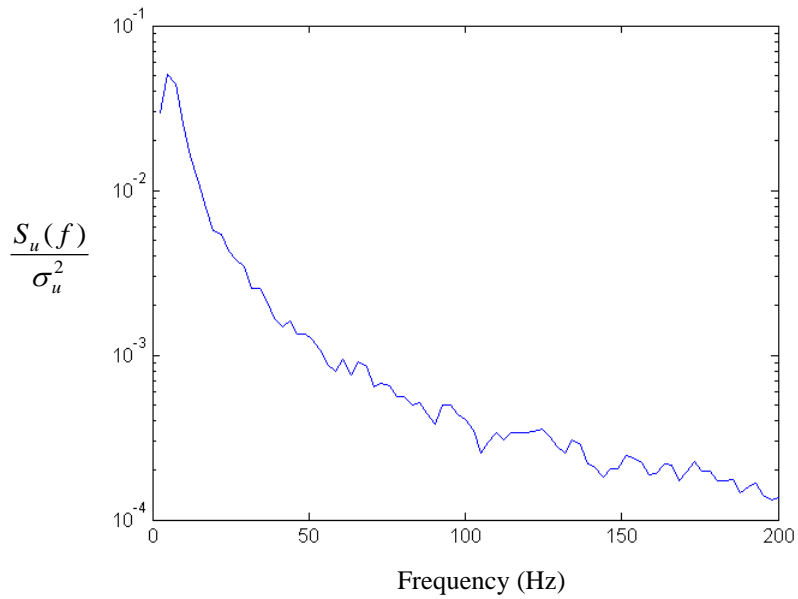


Figure 4-2: Velocity spectrum of approaching wind at roof height (100mm)

Pressures were measured using the Dynamic Pressure Measurement System (DPMS) from Turbulent Flow Instrumentation. The DPMS software is used to tune the tubing system transfer functions. For this study 1m length tubes with 1.5mm inner diameter were used. All pressures were filtered at 625Hz and sampled simultaneously at 1250Hz for 30 seconds. Each test configuration listed in Table 4-1 was repeated five times. The mean, standard deviation,

maximum and minimum pressures were obtained in each run were averaged and presented in pressure coefficient format ( $C_p = p/(1/2 \rho \bar{U}_h^2)$ ) to give  $\bar{C}_p$ ,  $C_{\sigma pi}$ ,  $\hat{C}_p$  and  $\check{C}_p$  values respectively.

#### 4.2.1 Wind Tunnel Model

A Perspex model building with the dimensions 400mm x 200mm x 100mm was constructed for wind tunnel testing. The model was extended by 600mm below the wind tunnel floor. Solid foam blocks were inserted into the building to vary the volume by 3 (V3), 5 (V5) and 7 (V7) times the initial volume of 400mm x 200mm x 100mm. The wind tunnel model and additional volume is shown in Figure 4-3. A dominant opening was centred on one of the 400mm walls. For this study, a single wind direction where the dominant opening is on the windward wall was studied. In addition to the varying volume, a series of four dominant opening configurations with varying area were also tested. They were 20mm x 20mm (A1), 50mm x 25mm (A2), 50mm x 50mm (A3) and 50mm x 80mm (A4).

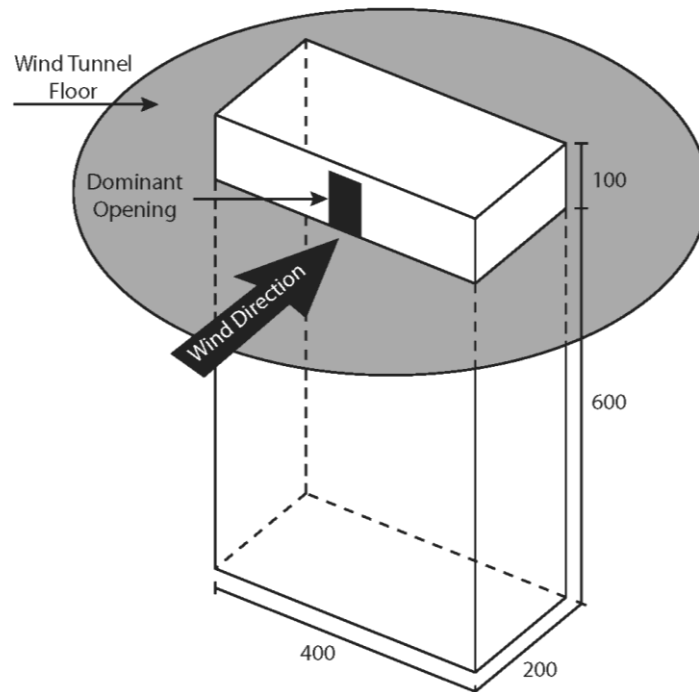


Figure 4-3: Scale model with dimensions 400mm x 200mm x 100mm with a 600mm extension below the wind tunnel floor (All dimensions presented in mm)

Background porosity was modelled by installing 64 x 1.5 mm diameter holes and 54 x 3 mm diameter holes uniformly on the two side walls, the leeward wall and the roof. These porous openings could be closed or opened as needed. The porosity configurations tested were no porosity (P1), only 1.5mm diameter holes open (P2), only 3mm diameter holes open (P3) and all 1.5mm and 3mm diameter holes open (P4). Figure 4-4 shows the location and spacing of the porous openings.

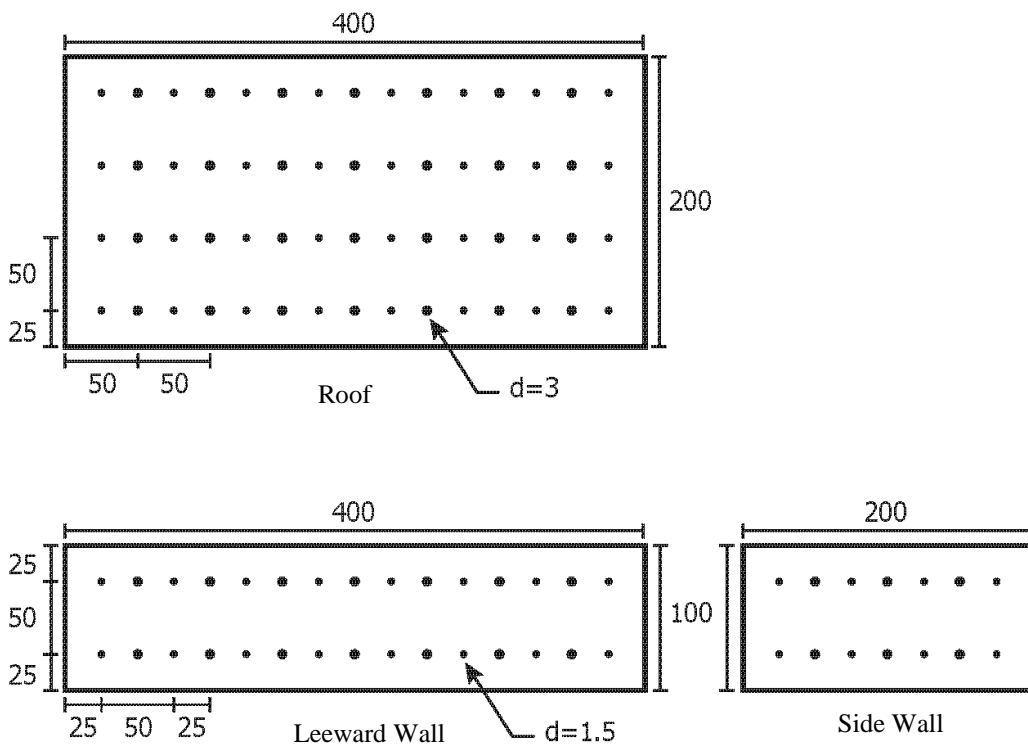


Figure 4-4: Location of 1.5mm and 3mm hole diameter,  $d$  of porosity for the wind tunnel model (All dimensions are presented in mm)

Pressure taps were installed on the roof, windward, leeward and side walls to measure the external pressures. A total of 21 roof taps, 6 taps on each side wall and 12 leeward wall taps were evenly distributed on the building surfaces. The mean lumped pressure acting on porous openings,  $\bar{C}_{pL}$  was obtained by area averaging measured pressures on the roof, side walls and leeward wall pressure taps and used when analysing Equation 3-2 and Equation 3-5.

The windward external pressure at the dominant windward wall opening,  $C_{pW}$  was measured in two ways. In the first method, 30 taps were staggered across an 80mm x 50mm door centred on the 400mm windward wall. The pressures were area averaged for the four corresponding dominant opening areas: A1, A2, A3 and A4. This method gives the external pressure on an intact building at the location of the dominant opening. Figure 4-5 shows the location of the external pressure taps and the corresponding dominant opening areas. In the second method, external windward pressures were measured across six taps 20mm on either side of the dominant opening and recorded simultaneously with the internal pressures. Then, internal and external pressures were used to determine net pressures,  $C_{p net}$  across the windward dominant opening.

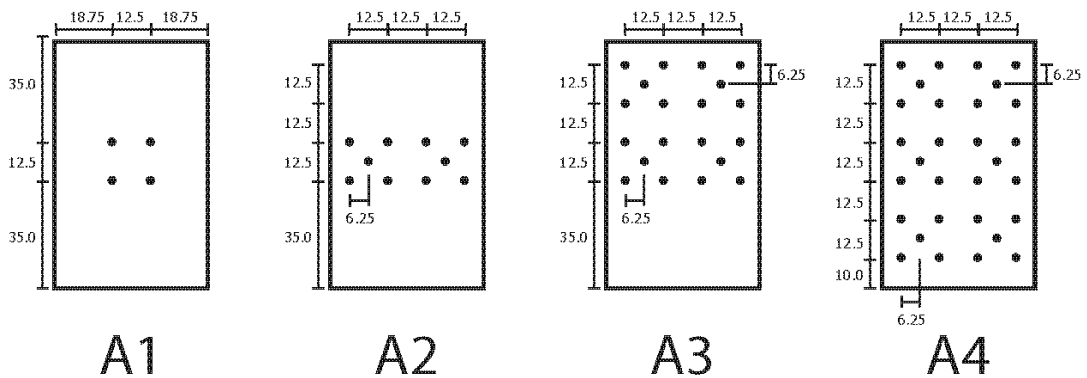


Figure 4-5: Areas A1 to A4 and locations of the external pressure taps used for area averaging (All units presented in mm)

The internal pressure,  $C_{pi}$  was measured for combinations of windward wall opening areas: A1, A2, A3, A4, volumes: V1, V3, V5, V7 and background porosities: P1, P2, P3, P4. Each windward opening area, porosity and volume gives a set of  $S^*$ ,  $\phi_5$  and  $\phi_6$  values given in Table 4-1. It should be noted that volume V1 was only tested for the non porous (P1) case.

Table 4-1: Test configurations opening and volume sizes,  $S^*$ , leakage area  $A_L$  with  $\phi_5$  and  $\phi_6$

$A_W$ (mm <sup>2</sup> )	Volume (mm <sup>3</sup> )	$S^*$	$A_L$ (mm <sup>2</sup> )	$\phi_6$
A1 = 20×20 $\phi_5 = 15.0$	V1 = 200×400×100	1.20	P1 = 0	0
	V3 = 200×400×300	0.46	P1 = 0	0
			P2 = 113	0.28
			P3 = 382	0.95
			P4 = 495	1.24
	V5 = 200×400×500	0.25	P1 = 0	0
			P2 = 113	0.28
			P3 = 382	0.95
			P4 = 495	1.24
	V7 = 200×400×700	0.17	P1 = 0	0
			P2 = 113	0.28
			P3 = 382	0.95
P4 = 495			1.24	
A2 = 50×25 $\phi_5 = 8.5$	V1 = 200×400×100	6.65	P1 = 0	0
	V3 = 200×400×300	2.56	P1 = 0	0
			P2 = 113	0.09
			P3 = 382	0.31
			P4 = 495	0.40
	V5 = 200×400×500	1.38	P1 = 0	0
			P2 = 113	0.09
			P3 = 382	0.31
			P4 = 495	0.40
	V7 = 200×400×700	0.95	P1 = 0	0
			P2 = 113	0.09
			P3 = 382	0.31
P4 = 495			0.40	
A3 = 50×50 $\phi_5 = 6.0$	V1 = 200×400×100	18.82	P1 = 0	0
	V3 = 200×400×300	7.24	P1 = 0	0
			P2 = 113	0.05
			P3 = 382	0.15
			P4 = 495	0.20
	V5 = 200×400×500	3.90	P1 = 0	0
			P2 = 113	0.05
			P3 = 382	0.15
			P4 = 495	0.20
	V7 = 200×400×700	2.69	P1 = 0	0
			P2 = 113	0.05
			P3 = 382	0.15
P4 = 495			0.20	
A4 = 80×50 $\phi_5 = 4.7$	V1 = 200×400×100	38.08	P1 = 0	0
	V3 = 200×400×300	14.65	P1 = 0	0
			P2 = 113	0.03
			P3 = 382	0.09
			P4 = 495	0.12
	V5 = 200×400×500	7.90	P1 = 0	0
			P2 = 113	0.03
			P3 = 382	0.09
			P4 = 495	0.12
	V7 = 200×400×700	5.44	P1 = 0	0
			P2 = 113	0.03
			P3 = 382	0.09
P4 = 495			0.12	

### 4.2.2 Numerical Model

Internal pressures were simulated and compared with measured wind tunnel results. The internal pressures were simulated using external pressures measured from the door areas A1, A2, A3 and A4 on the windward wall of the wind tunnel model. A first order explicit finite difference scheme was used to solve the governing equation as a function of opening area, internal volume and porous area. The first and second time derivatives of the internal pressure are shown in Equation 4-1 and Equation 4-2. Each time derivative was determined at a time step  $j$ , based on the two preceding time steps, where  $\Delta t$  is the time step.

$$\dot{C}_{pi}(j) = \frac{C_{pi}(j) - C_{pi}(j - 1)}{\Delta t} \quad \text{Equation 4-1}$$

$$\ddot{C}_{pi}(j) = \frac{C_{pi}(j) - 2C_{pi}(j - 1) + C_{pi}(j - 2)}{\Delta t^2} \quad \text{Equation 4-2}$$

## 4.3 Results and Discussion

This section describes results obtained from wind tunnel experiments on the building model with varying opening areas, internal volumes and levels of porosity, presented in Table 4-1. The mean, standard deviation and peak internal pressures are presented in a non-dimensional format and are compared with external pressure statistics averaged over a virtual opening area. The measured external pressures were averaged over the opening area and used to simulate internal pressures using a numerical model and matched with measured internal pressure spectra.

### 4.3.1 Sealed Building

External and internal pressure tables of the mean, standard deviation and peak pressure coefficients for each test configuration measured from the wind tunnel experiments are given in Appendix B. The ratios of the mean internal to external pressures for varying  $S^*$  values are shown in Figure 4-6. Figure 4-6 shows that the mean internal pressure matches closely with the mean external pressure at each dominant opening configuration. These results show that

generally, a variation in the internal volume will not affect the mean internal pressures as predicted by Liu (1975). For smaller values of  $S^*$  (i.e. configurations with the smallest opening area A1), the mean internal pressure was measured to be less than the mean external pressure. This difference is attributed to the selection of the location of the external pressure taps which may overestimate the mean pressure.

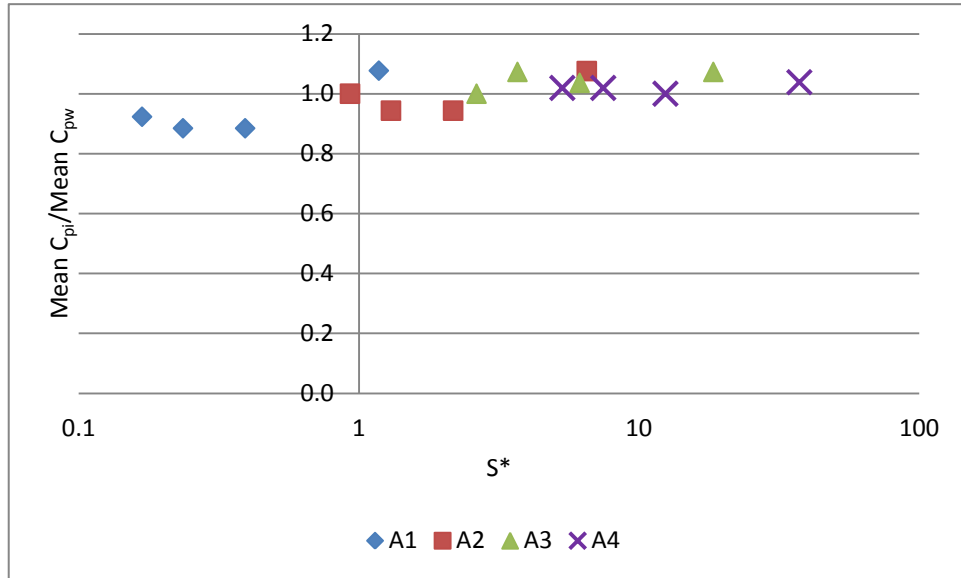
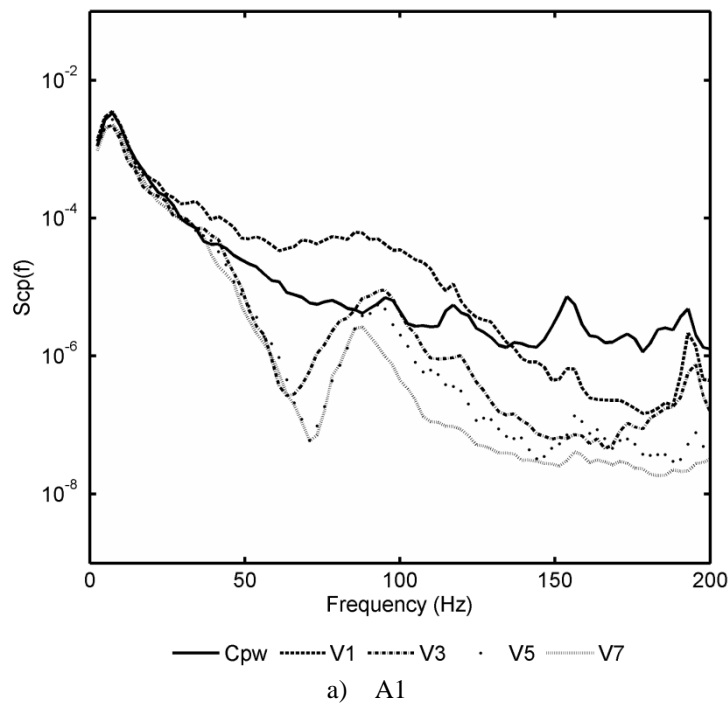


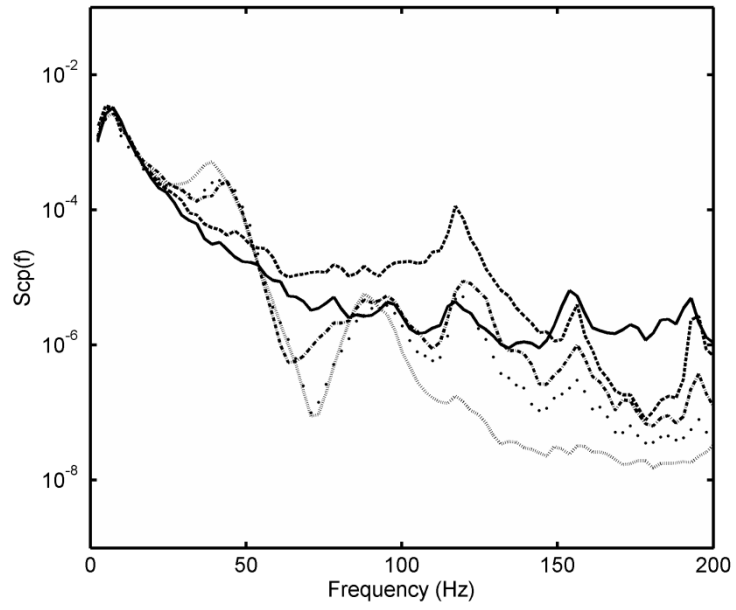
Figure 4-6: Ratio of measured mean internal to external pressure coefficient versus  $S^*$

The internal pressure spectra obtained from wind tunnel measurements, on the model with openings A1, A2, A3 and A4 for volumes V1, V3, V5, and V7 are shown in Figure 4-7a, b, c and d respectively. Helmholtz resonant frequencies were estimated using the undamped Helmholtz frequency equation and are summarized in Appendix A, Table 8-3. Figure 4-7a shows that for the opening and volume configuration A1 and V3, the Helmholtz resonance occurs at a frequency of approximately 40Hz. However, as the opening area increases to areas A2, A3 and A4, the Helmholtz frequency increases to approximately 44Hz, 45Hz and 50 Hz, respectively for a constant volume of V3. This trend is also observed in for volumes V1, V5 and V7. In all cases, configurations with area A1, resulted in the smallest Helmholtz resonance peaks. This is due to the smaller opening area to internal volume ratio. At higher frequencies

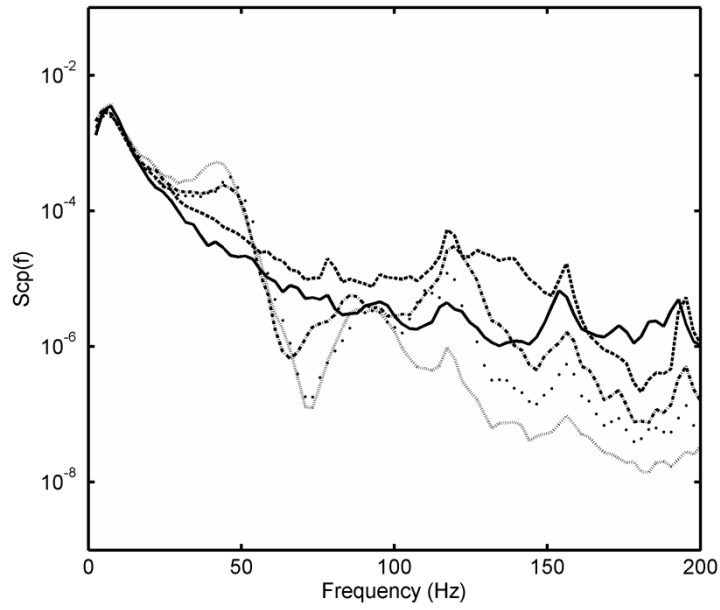
secondary peaks are observed, however since they occur at an order of magnitude below the Helmholtz resonance, it is not expected that they will influence the internal pressure fluctuations. It is worth noting that the undamped Helmholtz frequencies estimated in Table 8-3 differ slightly from the measured Helmholtz frequencies from the wind tunnel experiments. In this case, the measured values are assumed to be correct since the undamped Helmholtz equation ignores damping and is therefore only an approximation.

For a constant opening area and varying volume, the Helmholtz frequency reduces as volume increases. For example, in Figure 4-7b, the Helmholtz resonance for the A2V1 scenario occurs at a high frequency of approximately 120Hz. As the volume is increased, the Helmholtz frequency reduces to approximately 45Hz, 40 Hz and 38Hz for volumes V3, V5 and V7 respectively.





b) A2



c) A3

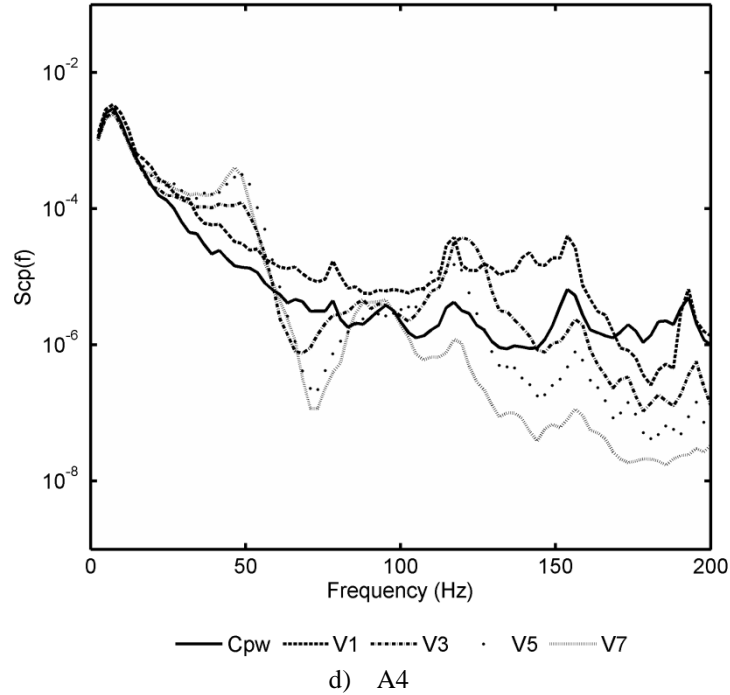


Figure 4-7: Internal pressure spectra for a) volume V1, b) volume V3, c) volume V5 and d) volume V7 with varying dominant opening areas A1 , A2, A3 and A4

The spectra shown in Figure 4-7 demonstrate the variation in internal pressure spectra with the varying sizes of opening areas and volumes. The variation in internal pressure fluctuations with respect to external pressure fluctuations is presented in Figure 4-8 as  $C_{\sigma pi}/C_{\sigma pW}$ , for a range of internal volumes and opening area sizes represented by  $S^*$  for a range of  $\phi_5$ . The fluctuations are represented by the standard deviation and the opening area and internal volume relationship is defined by  $S^*$ . The internal pressure standard deviation,  $C_{\sigma pi}$  exceeds the external pressure standard deviation,  $C_{\sigma pW}$  by about 10% when  $S^*$  is greater than about 0.4. The  $C_{\sigma pi}$  is less than the  $C_{\sigma pW}$  when  $S^*$  is less than 0.4. Figure 4-8 also compares the ratio of measured standard deviation of internal and external pressure to the empirical formula developed by Holmes and Ginger (2012). Holmes and Ginger (2012) compare their empirical formula with those developed by Irwin (1999) and Vickery (1992). For the purpose of this study the Holmes and Ginger (2012) fit has been used. The formula is given by Equation 4-3, where A, B and C can be adjusted to fit experimental data. Holmes and Ginger (2012) suggested values of  $C_{\sigma pi}/C_{\sigma pW} = 1.1$  when  $S^* \geq 1.0$  and  $A = 1.1, B = 4$  and  $C = 1.0$  for  $0.1 < S^* < 1.0$ . In the latter, a conservative  $\phi_5 = 20$  is also proposed for codification. The empirical fit is

slightly more conservative than the measured results and appears to be suitable for design purposes.

$$\frac{C_{\sigma pi}}{C_{\sigma pW}} = A + \left(\frac{B}{\phi_5}\right) \log_{10} \left(\frac{S^*}{C}\right) \quad \text{Equation 4-3}$$

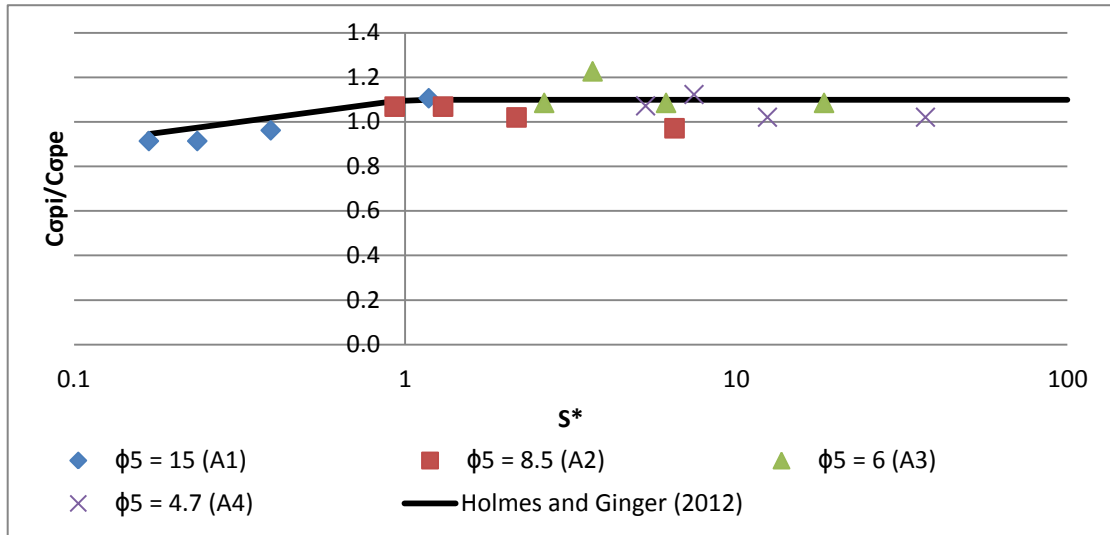


Figure 4-8: Measured ratio of internal to external pressure standard deviation versus  $S^*$  and  $\phi_5$  with area configurations shown in brackets

The ratio of measured peak internal to external pressures versus  $S^*$  for a range of  $\phi_5$  is shown in Figure 4-9. Figure 4-9 shows similar trends as Figure 4-8, where peak internal pressures are larger than peak external pressures by up to 20%, for  $S^*$  greater than approximately 0.4. Peak internal pressures are less than peak external pressures for  $S^*$  less than about 0.4. Figure 4-8 and Figure 4-9 show the importance of the opening area and internal volume relationship on internal pressure fluctuations and peak. Holmes and Ginger (2012) use an empirical formula to determine ratio of the peak internal to external pressure from atmospheric turbulence, shown in Equation 4-4. Equation 4-4 is plotted in Figure 4-9 assuming a peak factor,  $g = 4$  and turbulence intensity determined from turbulence intensity profile in Figure 4-1,  $I_u = 0.2$ . The empirical fit is slightly conservative when  $S^*$  is less than 1, however the empirical fit is unconservative when  $S^*$  is greater than 1.

$$\frac{\hat{C}_{pi}}{\hat{C}_{pw}} = \frac{1 + 2gI_u(C_{\sigma pi}/C_{\sigma pw})}{1 + 2gI_u} \quad \text{Equation 4-4}$$

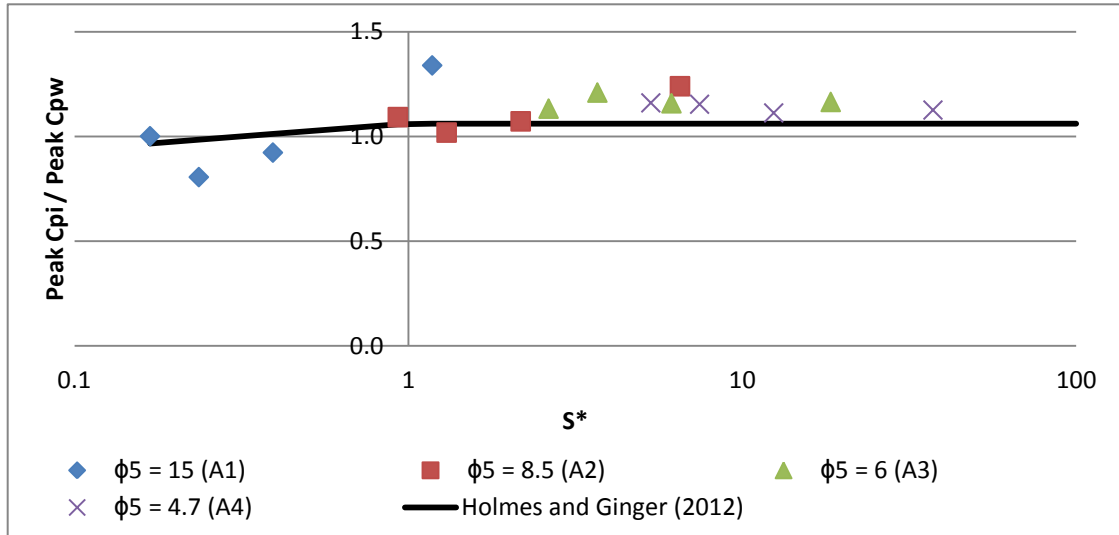


Figure 4-9: Measured ratio of peak internal to external pressure versus  $S^*$  and  $\phi_5$  with area configurations shown in brackets

#### 4.3.2 Internal Pressure Simulation

Figure 4-10 to Figure 4-25 show the measured external and internal pressure spectra and the spectra obtained from numerically simulated internal pressure, for opening areas A1, A2, A3 and A4 with internal volumes V1, V3, V5 and V7. The corresponding values for the inertial coefficient,  $C_I$  and discharge coefficient,  $k$  used for the simulating internal pressures are also listed in the figures. The inertial coefficient was estimated by matching the Helmholtz frequency from the numerically simulated internal pressure spectra with the measured Helmholtz frequency from the wind tunnel experiments. The discharge coefficient was estimated by matching the magnitude of the spectra from the numerically simulated internal pressure (especially near the Helmholtz resonance) with measured magnitude of the internal pressure spectra. At large frequencies secondary peaks were observed. While this study does not address this phenomenon, the peaks are 1 to 2 orders of magnitude less than the Helmholtz resonant peaks and will have a negligible effect on the internal pressure fluctuations.

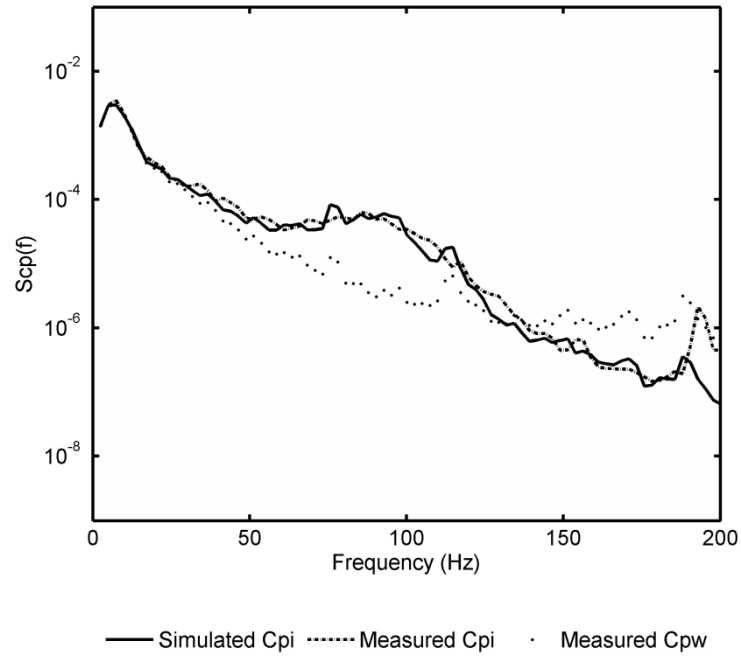


Figure 4-10: Measured external and internal and simulated internal pressure spectra for opening area A1 and volume V1 using  $k = 0.3$  and  $C_I = 0.89$  for simulations

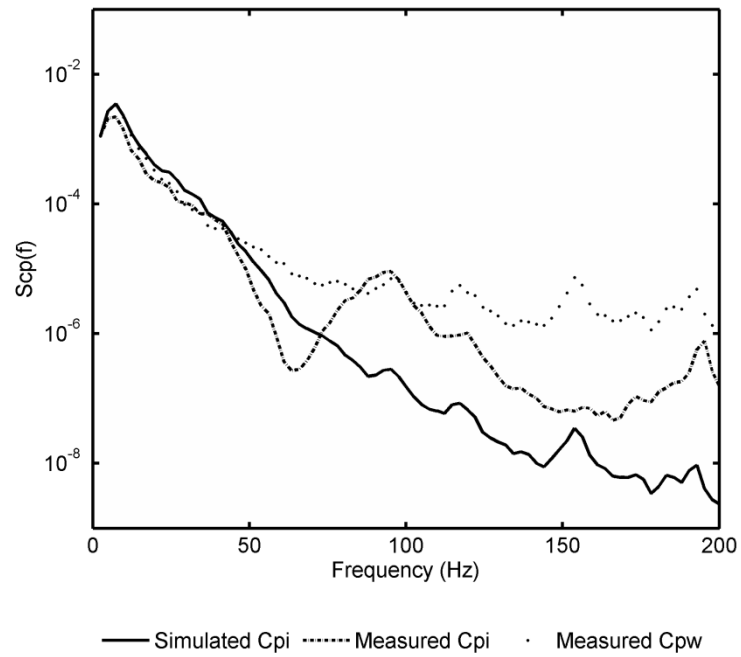


Figure 4-11: Measured external and internal and simulated internal pressure spectra for opening area A1 and volume V3 using  $k = 0.2$  and  $C_I = 1.7$  for simulations

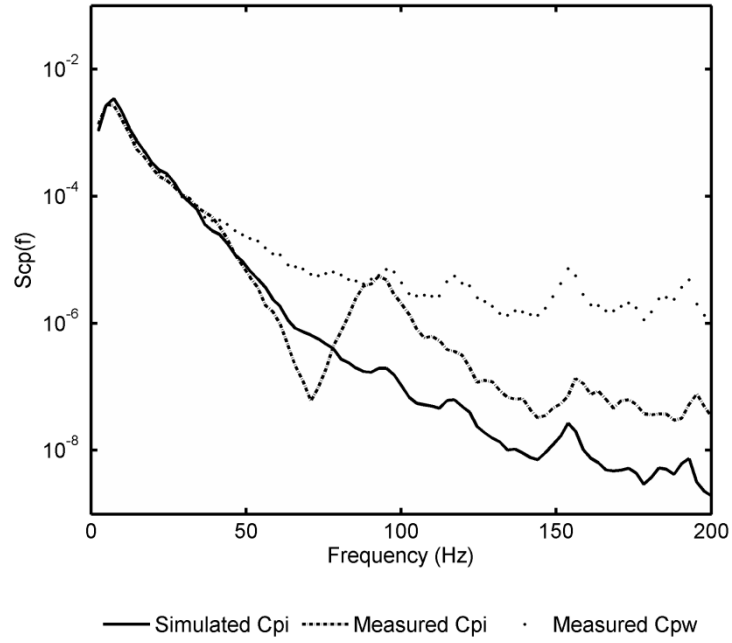


Figure 4-12: Measured external and internal and simulated internal pressure spectra for opening area A1 and volume V5 using  $k = 0.25$  and  $C_I = 1.15$  for simulations

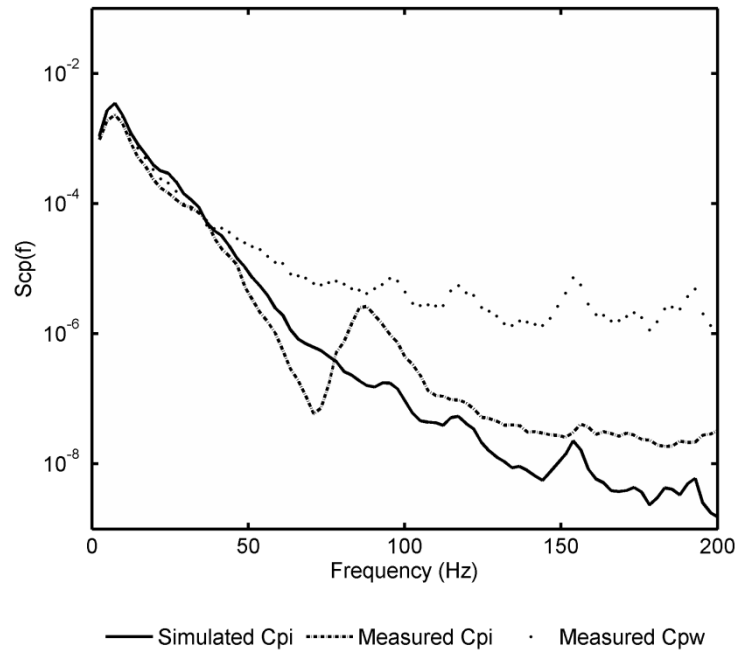


Figure 4-13: Measured external and internal and simulated internal pressure spectra for opening area A1 and volume V7 using  $k = 0.4$  and  $C_I = 0.9$  for simulations

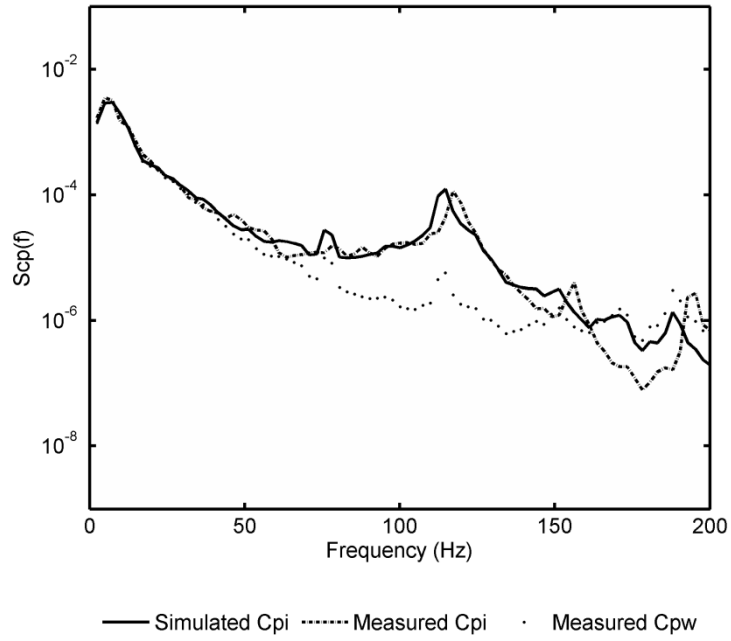


Figure 4-14: Measured external and internal and simulated internal pressure spectra for opening area A2 and volume V1 using  $k = 0.11$  and  $C_I = 1.0$  for simulations

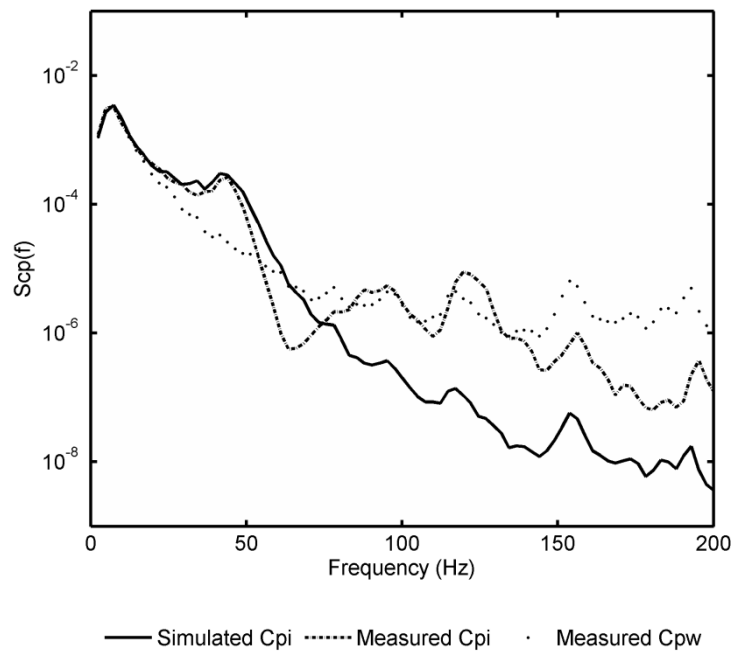


Figure 4-15: Measured external and internal and simulated internal pressure spectra for opening area A2 and volume V3 using  $k = 0.15$  and  $C_I = 2.2$  for simulations

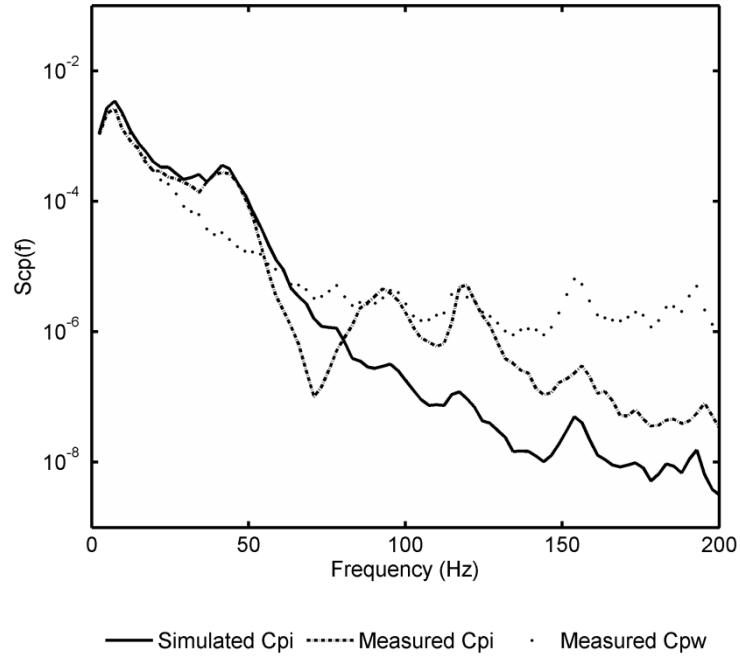


Figure 4-16: Measured external and internal and simulated internal pressure spectra for opening area A2 and volume V5 using  $k = 0.25$  and  $C_I = 1.4$  for simulations

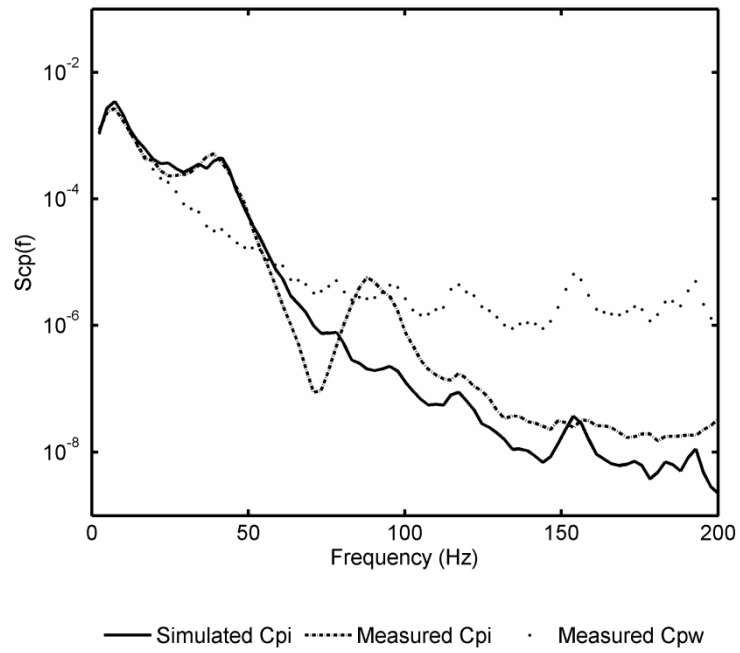


Figure 4-17: Measured external and internal and simulated internal pressure spectra for opening area A2 and volume V7 using  $k = 0.35$  and  $C_I = 1.15$  for simulations

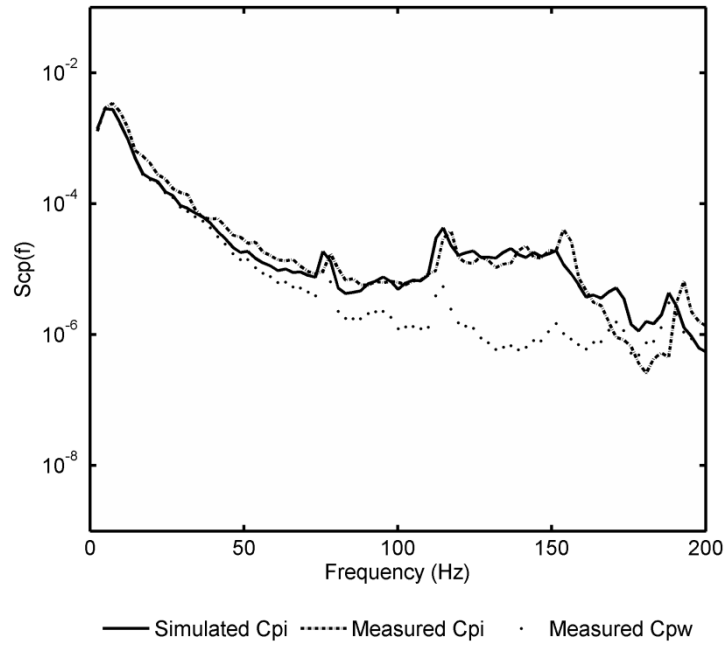


Figure 4-18: Measured external and internal and simulated internal pressure spectra for opening area A3 and volume V1 using  $k = 0.07$  and  $C_l = 1.1$  for simulations

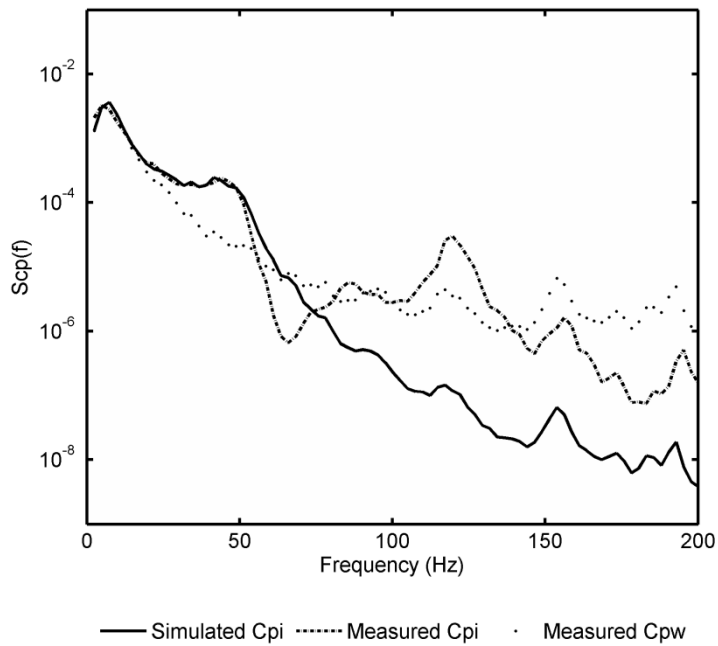


Figure 4-19: Measured external and internal and simulated internal pressure spectra for opening area A3 and volume V3 using  $k = 0.07$  and  $C_l = 3.0$  for simulations

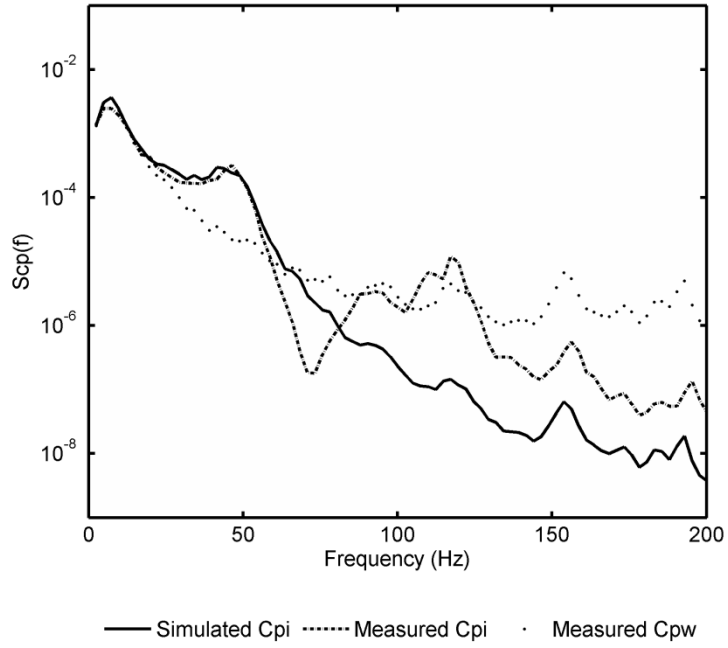


Figure 4-20: Measured external and internal and simulated internal pressure spectra for opening area A3 and volume V5 using  $k = 0.13$  and  $C_l = 1.8$  for simulations

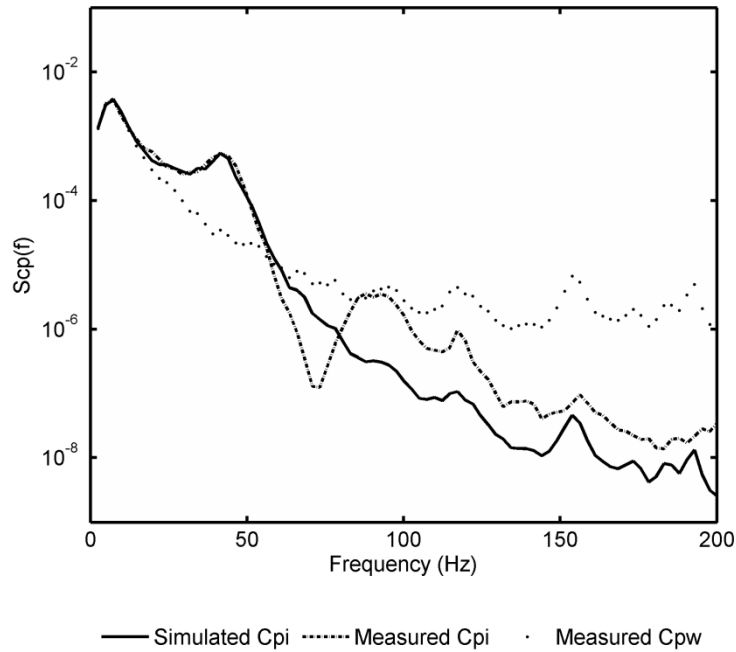


Figure 4-21: Measured external and internal and simulated internal pressure spectra for opening area A3 and volume V7 using  $k = 0.2$  and  $C_l = 1.5$  for simulations

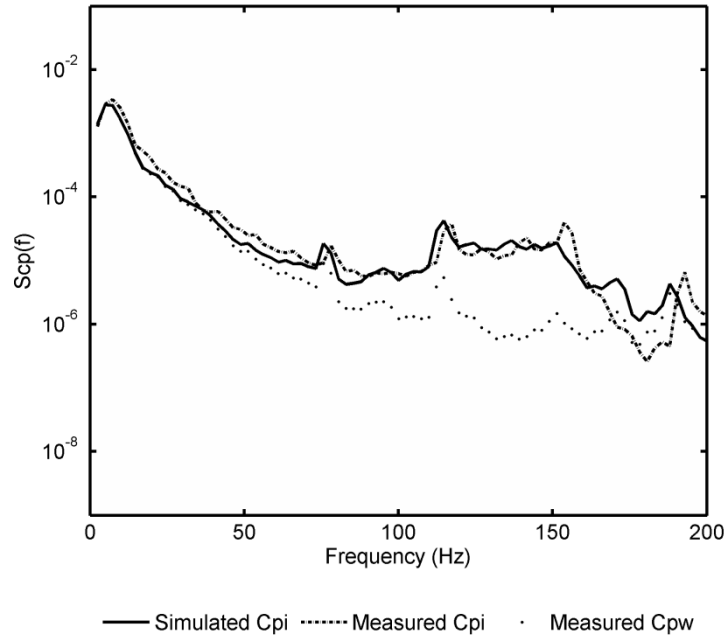


Figure 4-22: Measured external and internal and simulated internal pressure spectra for opening area A4 and volume V1 using  $k = 0.04$  and  $C_l = 1.3$  for simulations

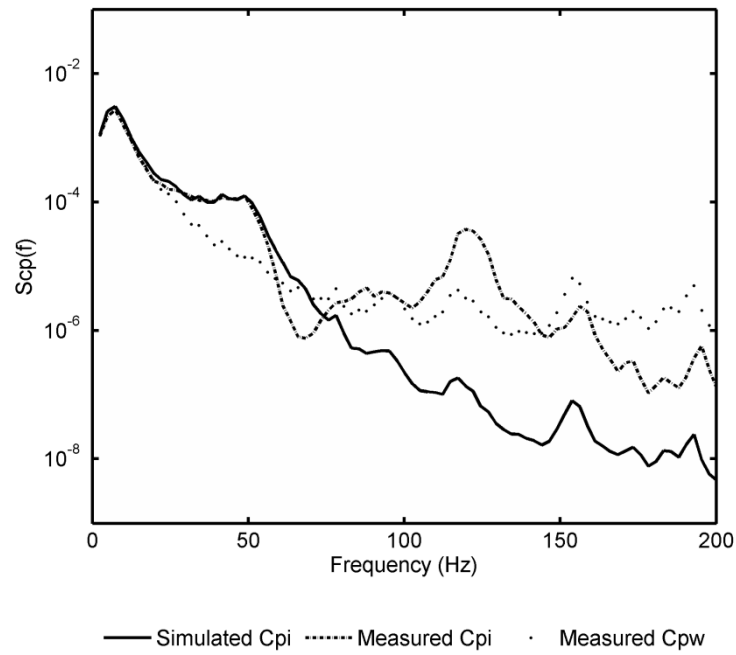


Figure 4-23: Measured external and internal and simulated internal pressure spectra for opening area A4 and volume V3 using  $k = 0.04$  and  $C_l = 3.4$  for simulations

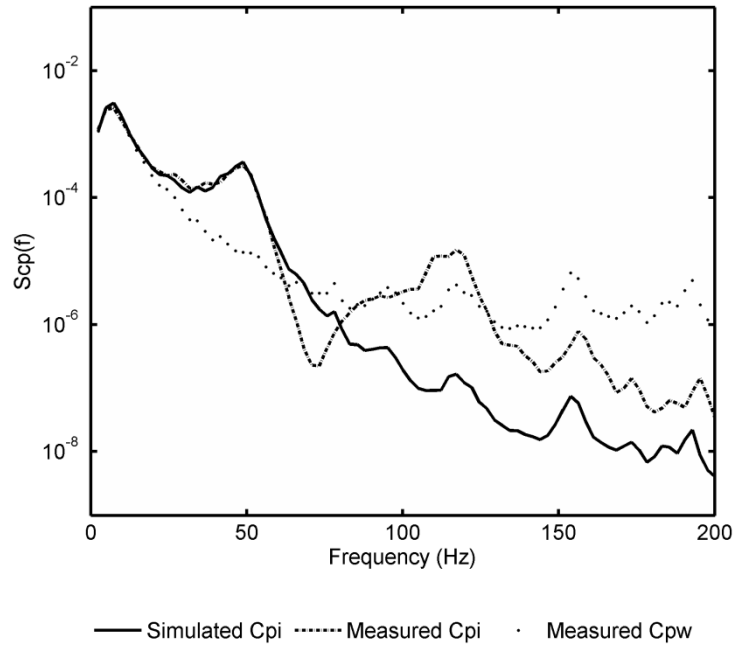


Figure 4-24: Measured external and internal and simulated internal pressure spectra for opening area A4 and volume V5 using  $k = 0.1$  and  $C_l = 2.1$  for simulations

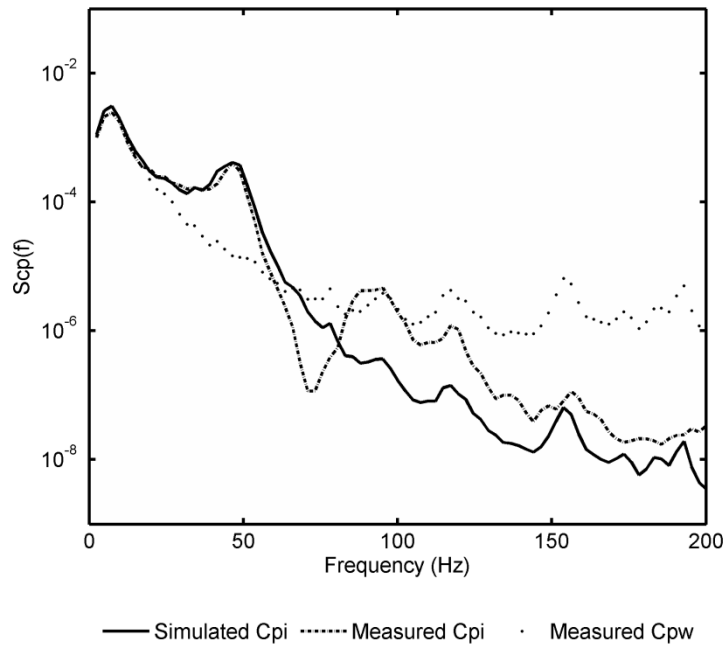


Figure 4-25: Measured external and internal and simulated internal pressure spectra for opening area A4 and volume V7 using  $k = 0.15$  and  $C_l = 1.6$  for simulations

Figure 4-10 to Figure 4-25 showed that the magnitude of  $k$  varied depending on the size of the opening area and the size of internal volume. The estimated discharge,  $k$  coefficient

ranged between 0.05 and 0.4. This range of  $k$  was less than the theoretical value used in steady flow of 0.61. Figure 4-26 shows the variation of  $k$  with  $S^*$ . The figure indicates that the magnitude of  $k$  reduces with increasing  $S^*$ . The reduction is due to the flow at the dominant opening being resisted by the air inside the volume. Figure 4-26 also shows that  $k$  becomes larger with decreasing  $S^*$ . The larger  $k$  is attributed to the flow through the opening being similar to the flow through an orifice connecting two large volumes.

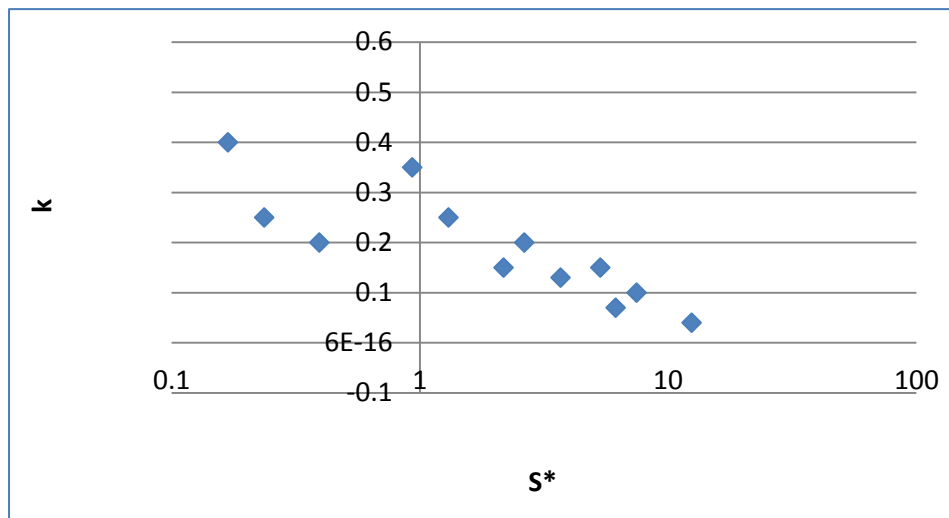


Figure 4-26: Discharge coefficient  $k$ , versus  $S^*$ , estimated from numerical simulations

Figure 4-27 presents the inertial coefficient  $C_I$  obtained from matching the  $f_H$  from the internal pressure simulations with the measured value, versus  $S^*$ . The  $C_I$  ranged between 0.9 and 3.4 depending on the size of opening area and size of internal volume. Figure 4-27 shows that for small values of  $S^*$ , the inertial coefficient is small. However, as  $S^*$  increases, the inertial coefficient will also increase. These values are generally higher than the assumed inertial coefficient of 0.89 from Helmholtz resonator theory. Vickery (1994) also stated that  $C_I$  could be up to a value of 2 for highly fluctuating flow. Sharma and Richards (1997b) use a separate flow coefficient to account for the contraction of the air slug at the opening that gives an overall equivalent  $C_I$  of approximately 1.5.

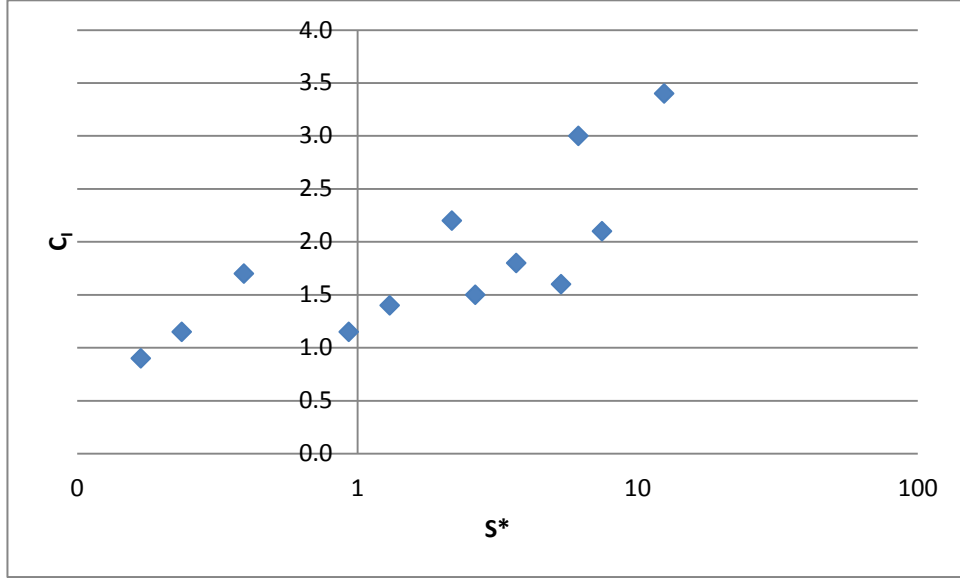


Figure 4-27: Inertial coefficient  $C_I$  versus  $S^*$ , estimated from numerical simulations

### 4.3.3 Linearization of the Governing Equation

Linearization can be used to simplify the governing equation (Equation 3-3). This allows internal pressure fluctuations to be determined explicitly. Vickery and Bloxham (1992) and Chaplin et al (2010) have linearized the governing equation for internal pressures. Yu et al (2006) determined that the Vickery and Bloxham linearization method matched closer to the admittance obtained by numerical methods. Using the Vickery and Bloxham (1992) method of linearization, the second order term can be represented in Equation 4-5. Here,  $\omega_H$  is the Helmholtz frequency in radians.

$$\dot{C}_{pi}|\dot{C}_{pi}| \approx \sqrt{\frac{8}{\pi}} C_{\sigma pi} \dot{C}_{pi} \omega_H \quad \text{Equation 4-5}$$

The damping coefficient represented by  $2\zeta$ , can then be expressed in terms of  $S^*$ , shown in Equation 4-6.

$$2\zeta = \sqrt{\frac{1}{2\pi} \frac{C_{\sigma pi}}{k^2 C_I S^*}} \quad \text{Equation 4-6}$$

The admittance function,  $X^2$  for the internal pressure response with respect to the external pressure forcing function is Equation 4-7.

$$X^2(\omega) = \frac{1}{\left(1 - \left(\frac{\omega}{\omega_H}\right)^2\right) + \left(2\zeta \frac{\omega}{\omega_H}\right)^2} \quad \text{Equation 4-7}$$

As the frequency approaches the Helmholtz frequency (i.e.  $\omega \cong \omega_H$ ) in Equation 4-7,  $X^2 = 1/4\zeta^2$ . Rearranging Equation 4-7 and solving for  $k$ , leads to Equation 4-8. This allows the discharge coefficient to be solved explicitly, using the measured admittance function of the internal and external pressure and estimated  $C_I$  values from the numerical simulation.

$$k \cong \sqrt{\left(\frac{\sqrt{1/4\zeta^2} C_{\sigma pi}}{\sqrt{2\pi} C_I S^*}\right)} \quad \text{Equation 4-8}$$

Figure 4-28 shows the discharge coefficients estimated by using Vickery and Bloxham's linearised equation versus  $S^*$ . The results shows similar trends to Figure 4-27, where the discharge coefficient is large at smaller  $S^*$  values and  $k$  is small for larger  $S^*$ . In general, the values for  $k$ , solved using linearization are slightly larger than the discharge coefficient values estimated using the numerical simulations. However, it is worth noting that in both cases, the  $k$  values estimated are less than the steady flow discharge coefficient of 0.61.

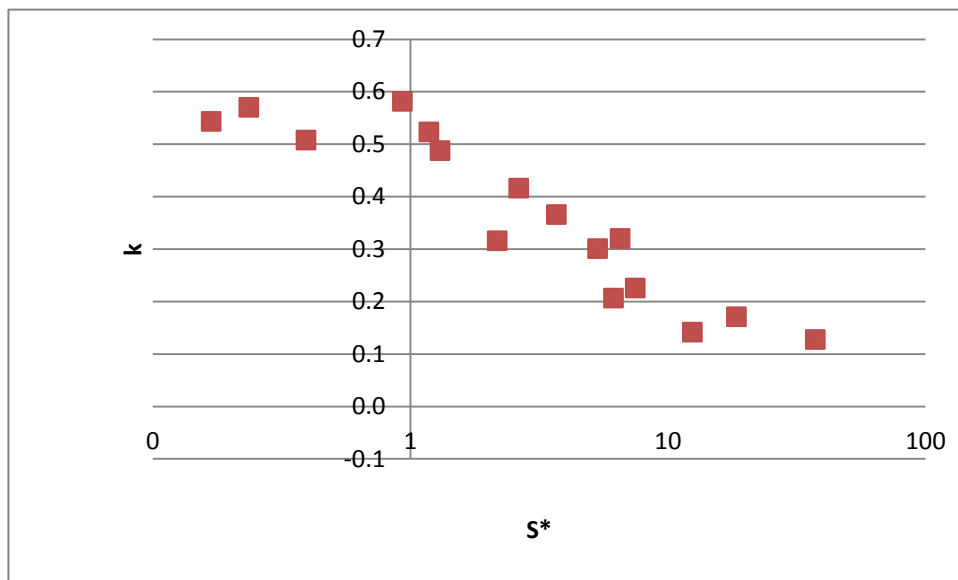


Figure 4-28: Discharge coefficient  $k$ , versus  $S^*$ , estimated by linearizing the governing equation using Vickery and Bloxham method

#### 4.3.4 Porous Building

Figure 4-29 compares the measured  $\bar{C}_{pi}$  to  $\bar{C}_{pw}$  ratios with theoretical values from Equation 3-9 for varying porosity levels,  $\phi_6 = A_L/A_w$ , where  $A_L$  is the lumped leeward opening and  $A_w$  is the dominant windward opening. When  $\phi_6 = 0$  (i.e. no porosity case)  $\bar{C}_{pi} = \bar{C}_{pw}$ . Using the measured mean leeward surface pressure coefficient,  $\bar{C}_{pL} = -0.6$ , the theoretical results show that when  $\phi_6$  is less than approximately 0.2,  $\bar{C}_{pi}$  is within 10% of the  $\bar{C}_{pw}$ . However, when  $\phi_6$  is larger than 0.2, the mean internal pressures are significantly reduced in comparison with the external pressures at the windward opening. These trends are similar to those obtained by Vickery (1994).

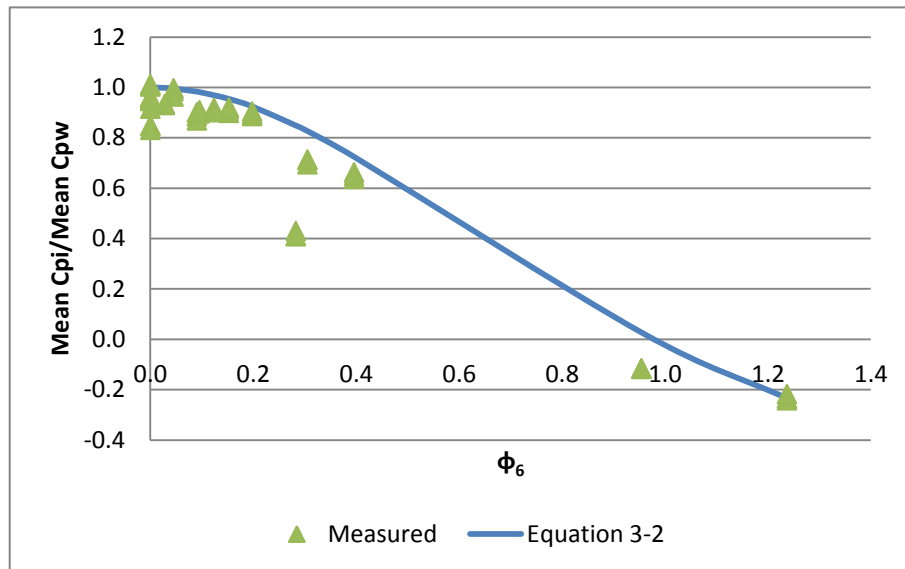
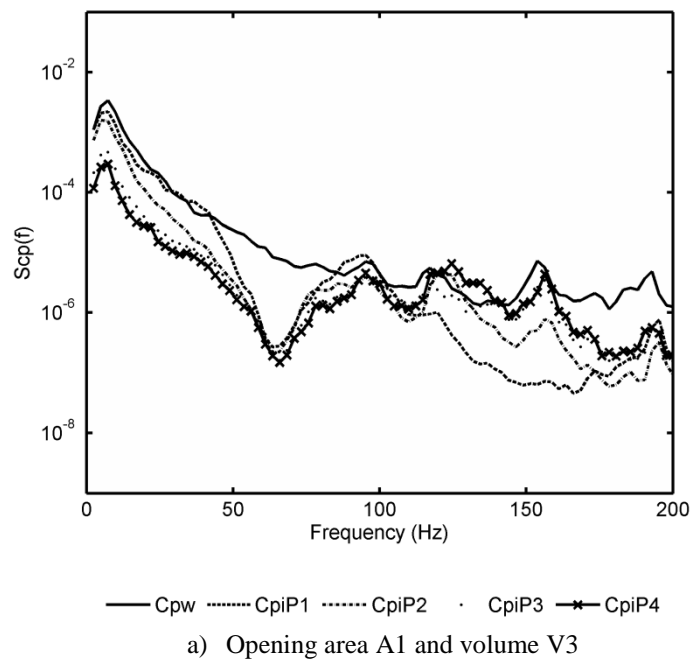


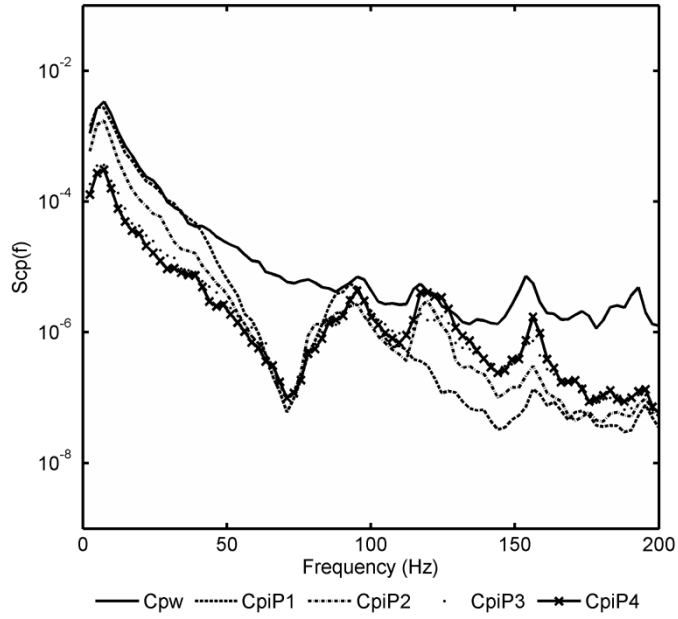
Figure 4-29: Ratio of internal and external mean pressure coefficients to  $\phi_6$

The measured external and internal pressure spectra  $S_{Cp}(f)$  with varying background porosities P1, P2, P3 and P4, with volumes V3, V5 and V7 for opening areas A1, A2, A3 and A4 are shown in Figure 4-30, Figure 4-31, Figure 4-32 and Figure 4-33 respectively. In Figure 4-30, the background component of the internal pressure spectra for the sealed building case (P1) closely match the background component of the external pressure spectra at low frequencies. However, as porosity is introduced, the internal pressure spectra becomes

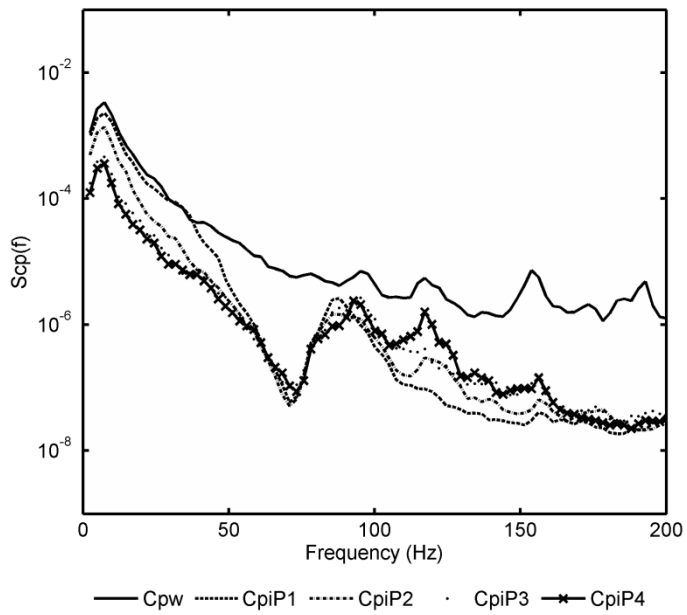
dominated by the porosity and the background component of the internal pressure spectra becomes an order of magnitude less than the external pressure spectra at the opening.

Figure 4-31a shows a distinct Helmholtz resonant peak at approximately 45 Hz when the building is sealed (P1). Increasing the porosity from P2, P3 to P4 progressively reduces the magnitude of the Helmholtz peak. The damping is caused by large values of  $\phi_6$ . For this case  $\phi_6$  was equal to 0.09, 0.31 and 0.40 for porosities P2, P3 and P4 respectively. When  $\phi_6$  is equal to 0.31 and 0.40, the Helmholtz resonance is almost completely damped. Similar trends are observed in Figure 4-32 and Figure 4-33; however there is less attenuation of the Helmholtz peaks because of the smaller  $\phi_6$  values (ie. less porosity). The  $\phi_6$  values were 0.05, 0.15 and 0.20 for Figure 4-32 and 0.03, 0.10 and 0.12 for Figure 4-33 for porosities P2, P3 and P4 respectively.



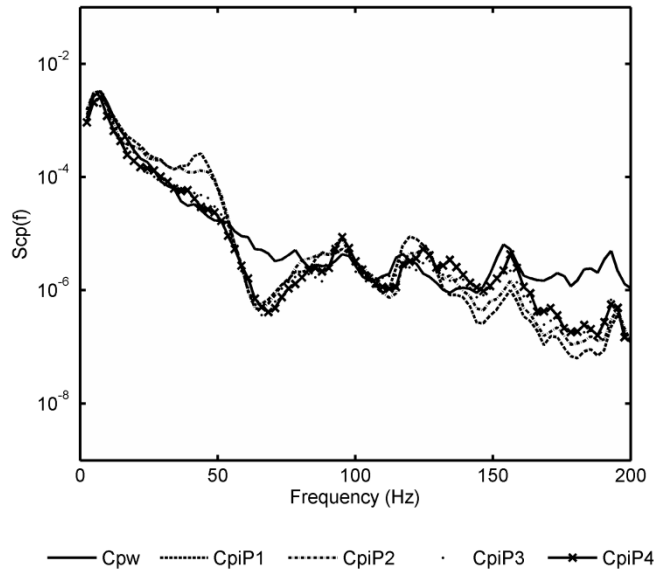


b) Opening area A1 and volume V5

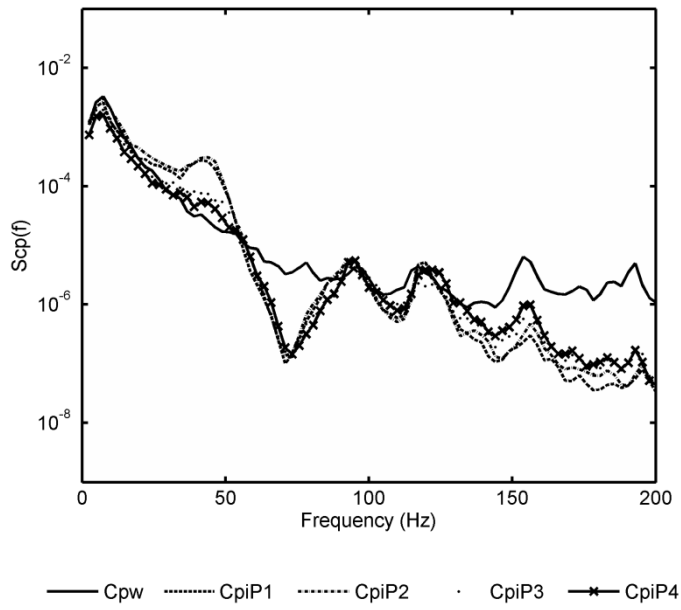


c) Opening area A1 and volume V7

Figure 4-30: Measured external and internal pressure spectra for varying  $\phi_6$  values of 0 (P1), 0.28 (P2), 0.95 (P3) and 1.24 (P4) for area A1 and volumes V3, V5 and V7



a) Opening area A2 and volume V3



b) Opening area A2 and volume V5

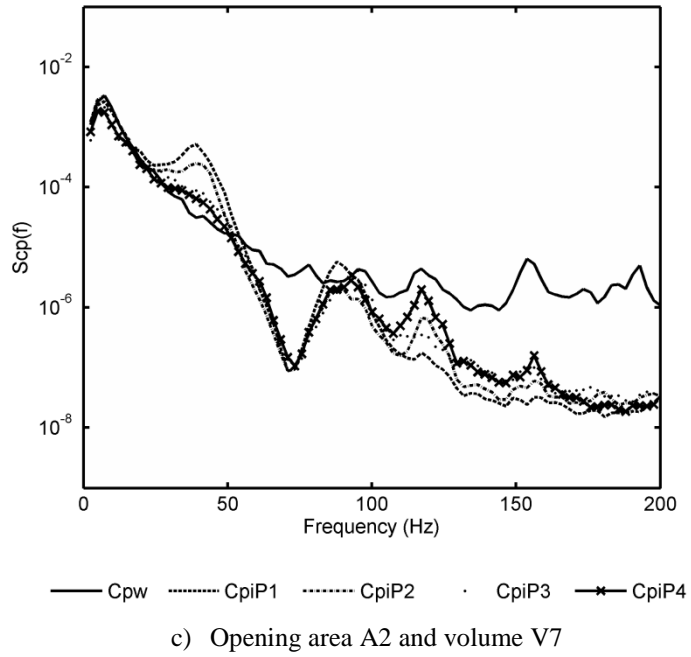
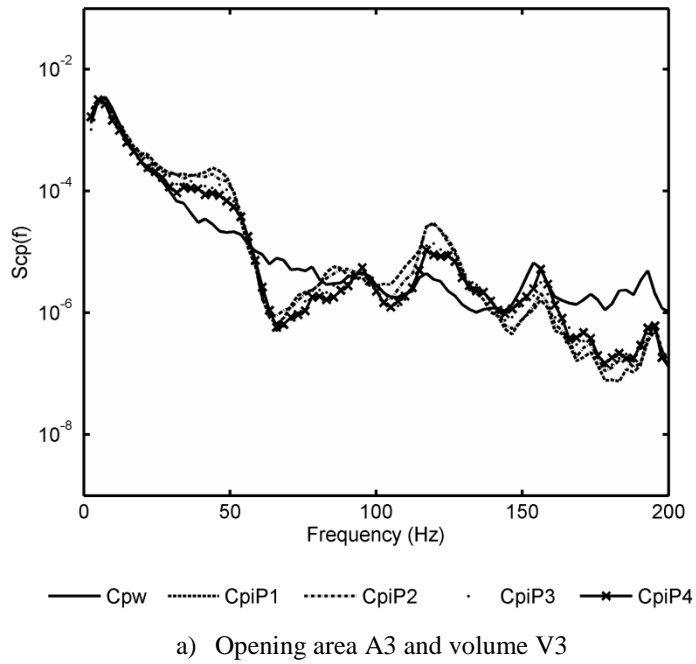
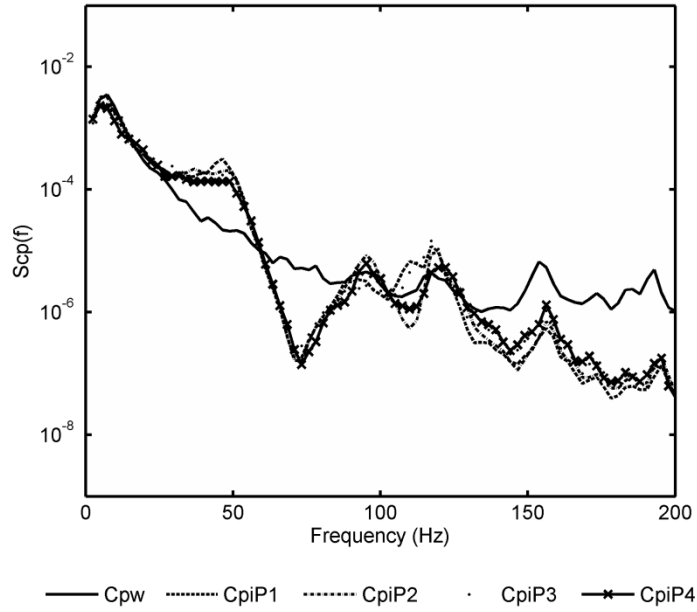
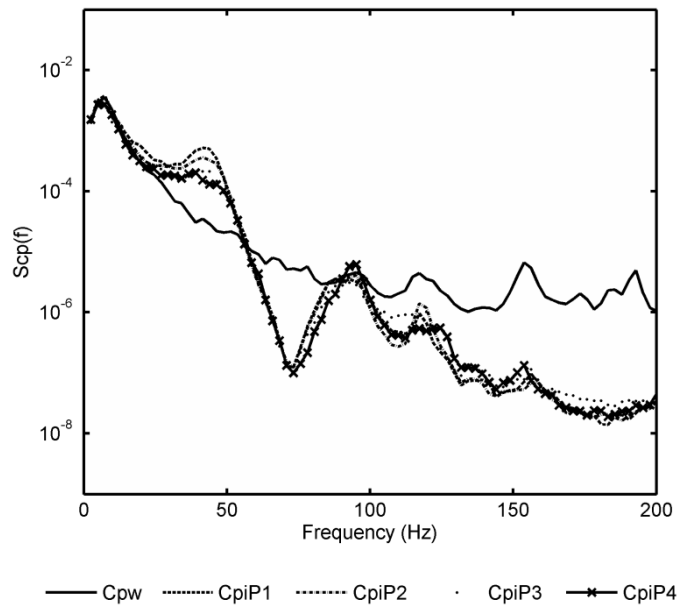


Figure 4-31: Measured external and internal pressure spectra for varying  $\phi_6$  values of 0 (P1), 0.09 (P2), 0.31 (P3) and 0.40 (P4) for area A2 and volumes V3, V5 and V7



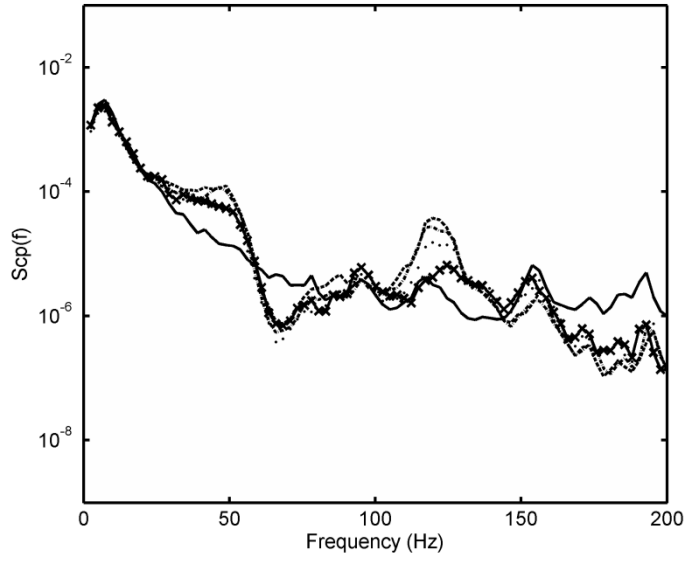


b) Opening area A3 and volume V5



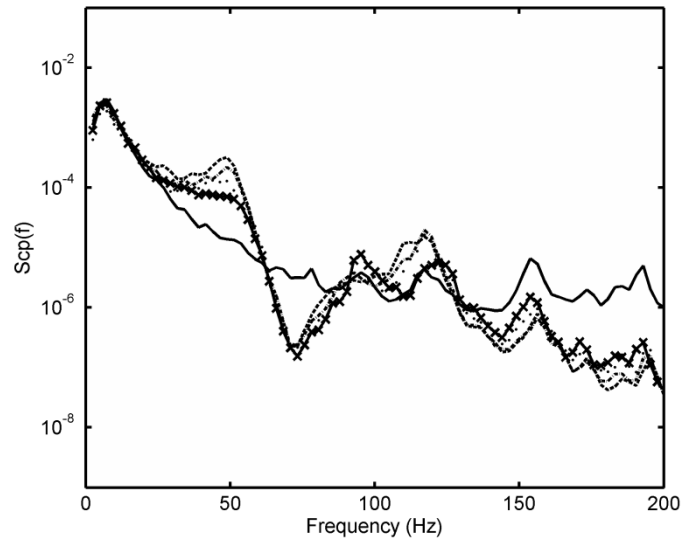
c) Opening area A3 and volume V7

Figure 4-32: Measured external and internal pressure spectra for varying  $\phi_6$  values of 0 (P1), 0.05 (P2), 0.15 (P3) and 0.20 (P4) for area A3 and volumes V3, V5 and V7



— Cpw    ..... CpiP1    -.-.-.- CpiP2    ····· CpiP3    —\*— CpiP4

a) Opening area A4 and volume V3



— Cpw    ..... CpiP1    -.-.-.- CpiP2    ····· CpiP3    —\*— CpiP4

b) Opening area A4 and volume V5

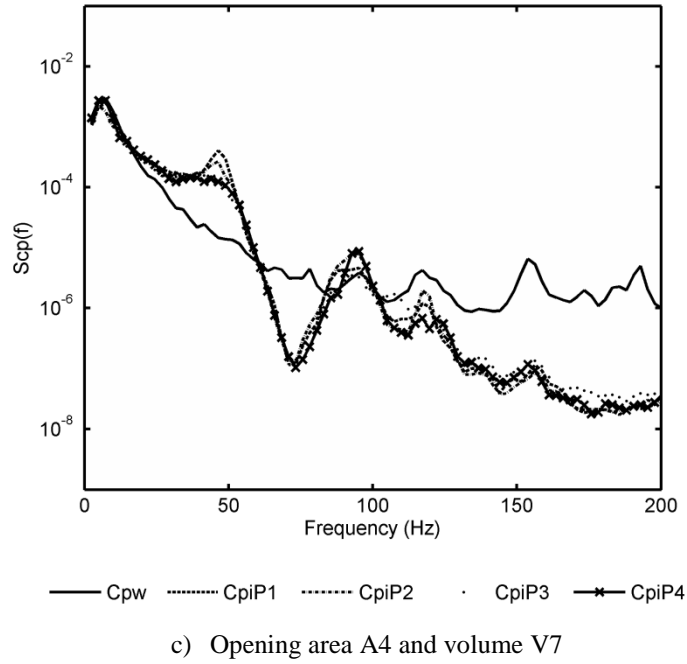


Figure 4-33: Measured external and internal pressure spectra for varying  $\phi_6$  values of 0 (P1), 0.03 (P2), 0.10 (P3) and 0.12 (P4) for area A4 and volumes V3, V5 and V7

The ratio of the measured  $C_{\sigma pi}$  to  $C_{\sigma pw}$  are compared with  $S^*$  for ranges of  $\phi_6$ , as shown in Figure 4-34. When  $\phi_6$  is less than 0.1, the internal pressure fluctuations were greater than the external pressure fluctuations for  $S^*$  values larger than 0.4. For cases when  $S^*$  is less than 0.4, the internal pressure fluctuations are greatly reduced compared to external pressure fluctuations. This figure also shows that when the background porosity is increased the internal pressure fluctuations are attenuated. The magnitude of the reduction is dependent on the magnitude of the porous area to dominant opening area  $\phi_6$  in addition to  $S^*$ . For low  $\phi_6$  values between 0.1 and 0.2, the attenuation of the internal pressure fluctuation is small. However when  $\phi_6$  is greater than 0.2 the internal pressure fluctuations decrease by greater than 20%, especially when  $S^*$  is less than 0.4. For comparison, results from Vickery and Bloxham (1992) were also plotted on Figure 4-33. The results are similar for the range of  $\phi_6$  values tested in this study. The ratio of the measured  $\hat{C}_{pi}$  to  $\hat{C}_{pw}$  is shown in Figure 4-35. The measured peak pressures follow similar trends to the measured standard deviations. This is expected since smaller internal pressure fluctuations results in smaller peak pressures.

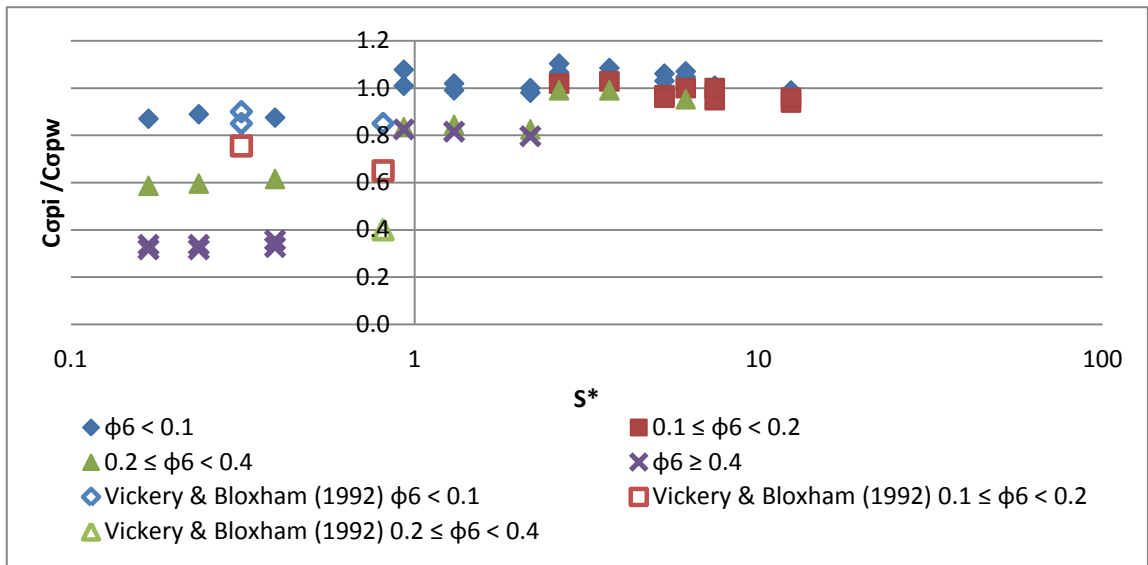


Figure 4-34: Ratio of internal and external pressure standard deviation to  $S^*$  for varying  $\phi_6$

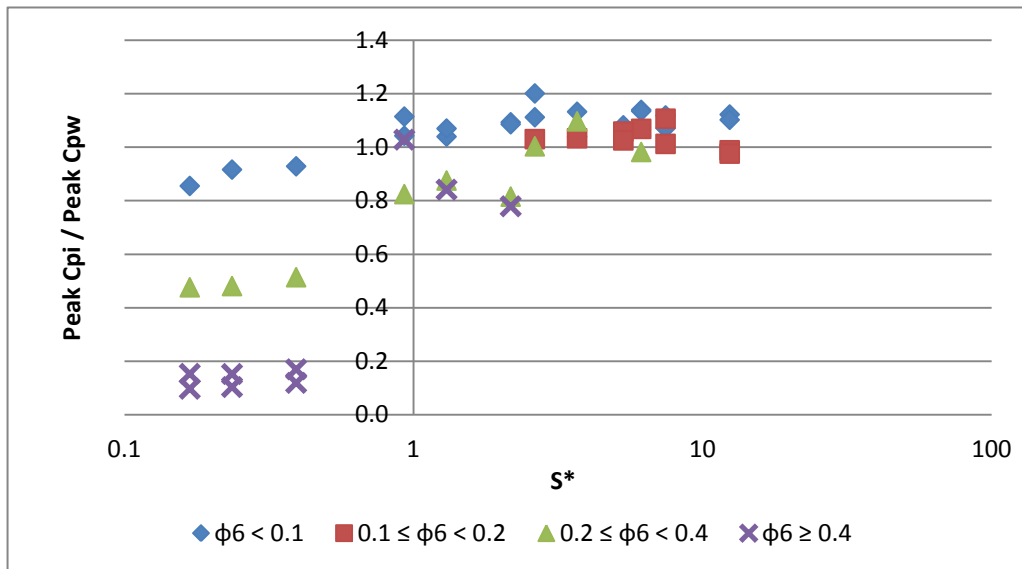
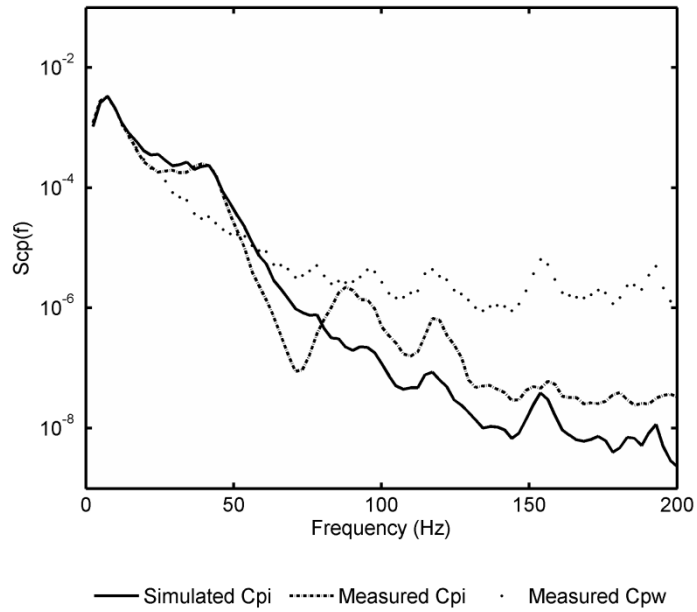


Figure 4-35: Ratio of internal and external peak pressure coefficient to  $S^*$  for varying  $\phi_6$

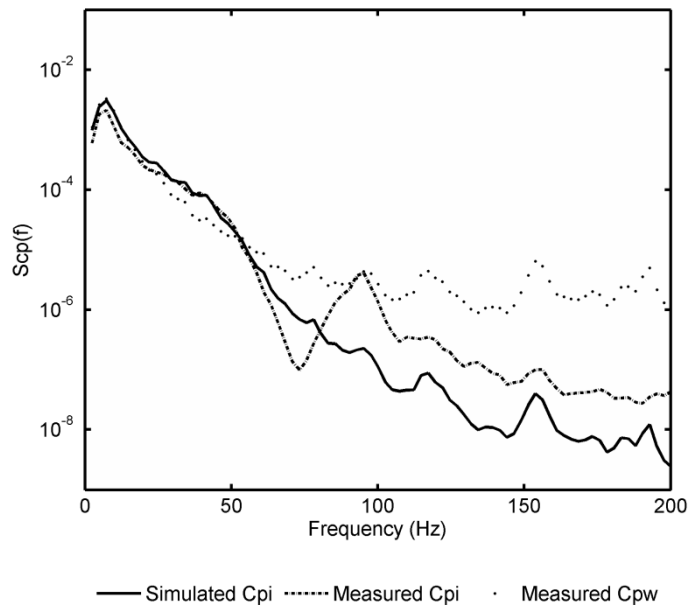
#### 4.3.5 Internal Pressure Simulation

The spectra of the internal pressure simulations using Equation 3-5 were matched with measured internal pressure spectra obtained from the wind tunnel results by varying the parameters:  $C_I$ ,  $k$  and  $k'_L$ , where  $k'_L$  is the lumped background porosity discharge coefficient. The windward wall opening discharge coefficient,  $k$  and inertial coefficient  $C_I$  obtained from the sealed building case (P1), were assumed to be the same for the porous cases. The lumped background leakage discharge coefficient  $k'_L$  was adjusted to match internal pressure spectra for

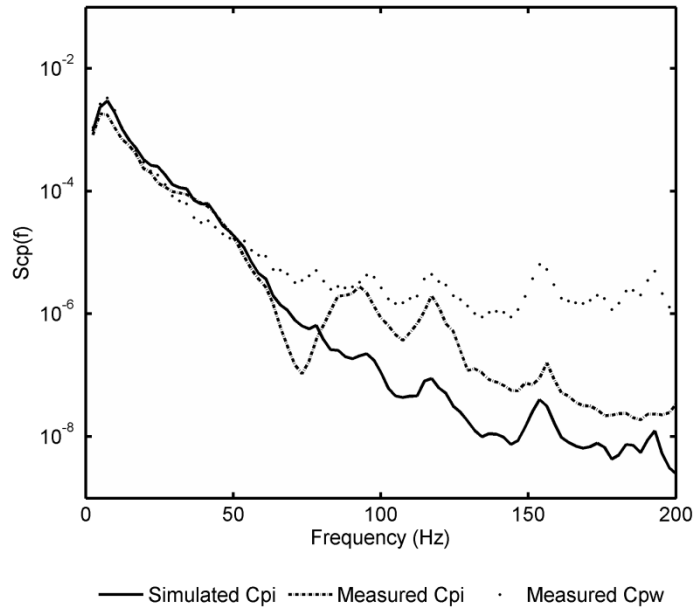
P2, P3 and P4. A comparison of the measured external pressure spectra and measured and simulated internal pressure spectra for configurations A2V7 and A4V7 with porosities of P1, P2, P3 and P4 are presented in Figure 4-36 and Figure 4-37, respectively. The figures also show the  $k$  and  $k'_L$  used for simulations.



a) P2,  $k = 0.35, k'_L = 0.4$

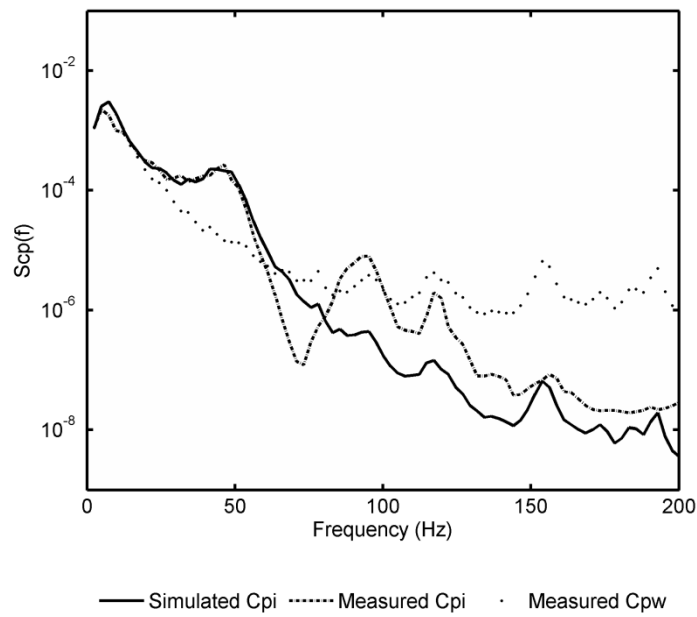


b) P3,  $k = 0.35, k'_L = 0.25$

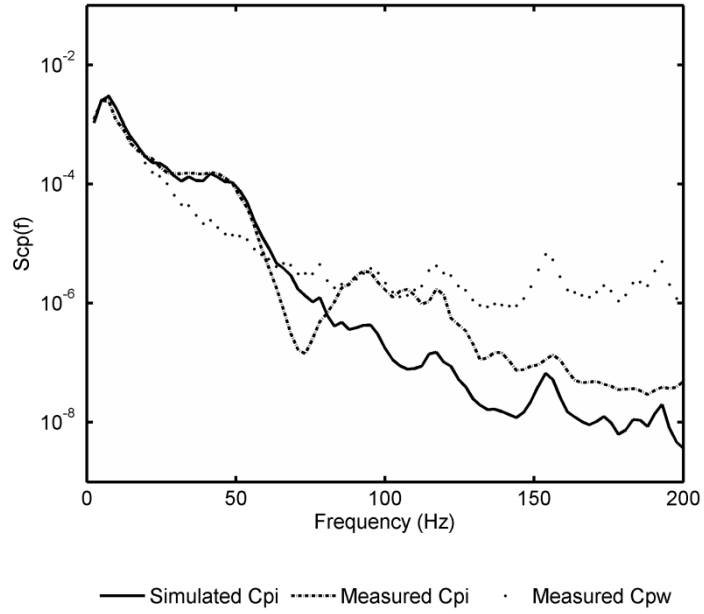


c) P4,  $k = 0.35, k'_L = 0.22$

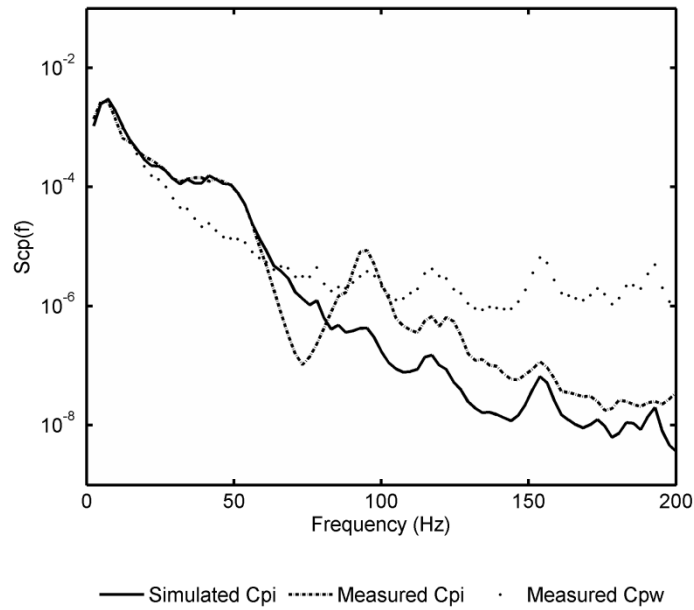
Figure 4-36: Area A2 and internal volume V7 for porosities with a constant  $k$  and varying  $k'_L$



a) P2,  $k = 0.15, k'_L = 0.4$



b) P3,  $k = 0.15, k'_L = 0.2$



c) P4,  $k = 0.15, k'_L = 0.15$

Figure 4-37: Area A4 and internal volume V7 for porosities with opening  $k = 0.15$  and varying  $k'_L$

Figure 4-38 shows the effective discharge coefficient  $k'_L$  for the background leakage area with increasing  $S^*$  and varying  $\phi_6$ . The estimated  $k'_L$  values have a large variation ranging from 0.05 to 0.5. Figure 4-38 shows that in general, for larger  $\phi_6$  values, the estimated  $k'_L$  values tend to decrease. This may seem unexpected, however it is possible that in scenarios

which exhibit a strong Helmholtz phenomenon (ie. reversing flow at the dominant opening) could decrease the porous opening discharge coefficient, even if it is large.

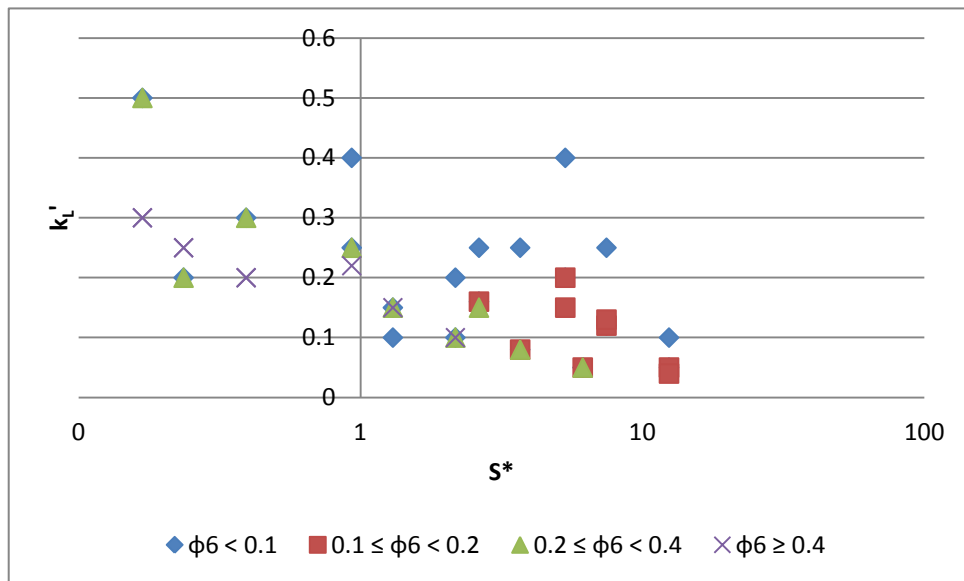


Figure 4-38: Discharge coefficient for background porosity  $k'_L$  with increasing  $S^*$

Figure 4-39 shows the variation of lumped background porosity discharge coefficient,  $k'_L$  with the dominant opening discharge coefficient,  $k$  for varying porosity configurations. Here, it is assumed that  $k$  is not influenced by an increase in the background porosity and is taken as the values determined from the non porous building case. The results show, that when the dominant opening discharge coefficient is small, the porous opening discharge is also small. An increase in the  $k$  values results in an increase in the values of  $k'_L$ . As increasing flow passes through the dominant opening, there is a corresponding increase in the flow through porous openings. However, when less flow passes through the dominant opening, the air flow through the porous openings are also reduced. It is worth noting, that it is possible that  $k$  could vary depending on the level of porosity present in a building, since porous openings will cause an increase in the flow through the dominant opening. Given the current testing configuration, it was not possible to measure the dominant opening discharge coefficient, nevertheless the general trends of the relationship between the dominant opening and porous opening discharge coefficients are valid.



## 5 Flow Characteristics across an Opening

### 5.1 Experimental Setup

Following on the estimation of the discharge coefficient  $k$  from wind tunnel results, a second experiment was designed to study the discharge characteristics across an opening. Figure 5-1 shows the experimental set-up used for studying the flow characteristics through an opening. The 700mm x 200mm x 400mm pressure chamber was attached to a pressure loading actuator (PLA) via a 90mm diameter, 4m length of PVC pipe and a settling volume. The PLA uses a rotating disc in the valve to control the flow rate and the applied pressure to a test chamber (Kopp et al., 2010). A pressure transducer was installed in the pressure chamber and used as feedback by a computer which adjusted the disc position in the valve until the target pressure was obtained.

The openings were subjected to a series of static, unidirectional sinusoidal and reversing sinusoidal pressures. Static pressure is when a constant pressure drop is maintained across the opening. A unidirectional sinusoidal pressure is defined as a sinusoidal pressure trace in the pressure chamber which remains entirely positive and results in a fluctuating but unidirectional flow. Reversing flow is defined as sinusoidal pressure in the pressure chamber that crosses 0Pa (i.e. the flow changes direction).

The mean pressure drop across the opening is  $\Delta\bar{p} = \frac{1}{2}\rho C_L \bar{U}_o^2$ . The mean flow through the opening is  $\bar{Q} = \bar{U}_o \times A_o$ . The mean flow through the opening was measured by determining the mean flow through the pipe using a Cobra Probe. The Cobra Probe uses multiple holes to measure velocity time histories in three dimensions. To measure the mean velocity profile in the PVC pipe, the Cobra Probe was immersed in the flow with the holes positioned in the positive flow longitudinal direction and traversed at 5mm intervals along the radius of the pipe. The velocity time history at each 5mm interval was averaged to determine the mean velocity at each interval. The mean velocity profile was integrated over the cross sectional area of the PVC pipe

to estimate the mean flow,  $\bar{Q}$ . Since the Cobra Probe does not measure velocity in the reverse longitudinal direction (i.e. air flow moving towards the PLA), a repeat test was performed with the Cobra Probe positioned in the opposite direction ( $180^\circ$ ) for each reversing sinusoidal flow configuration. The velocity time history  $U_{forward}$  was appended to  $U_{reverse}$  and a mean net velocity profile was estimated. This mean net velocity was then integrated over the cross sectional area to determine a mean net flow,  $\bar{Q}_{net}$  through the opening. A single discharge coefficient can then be estimated using the time average discharge equation,  $C_L = \Delta\bar{p} / \frac{1}{2} \rho \bar{U}_o^2$ , where,  $C_L = 1/k^2$ .

Pressure taps were installed in the pressure chamber and measured simultaneously with the Cobra Probe using the TFI integrated DPMS. Pressures were sampled at 1250Hz for 60 seconds. The mean pressure drop across the opening,  $\Delta\bar{p}$  is determined by the difference between the pressure chamber and atmospheric pressure. It should be noted, that the pressure transducer used for the control of the PLA was independent of the TFI data acquisition system. A schematic of the experiment setup is shown in Figure 5-1.

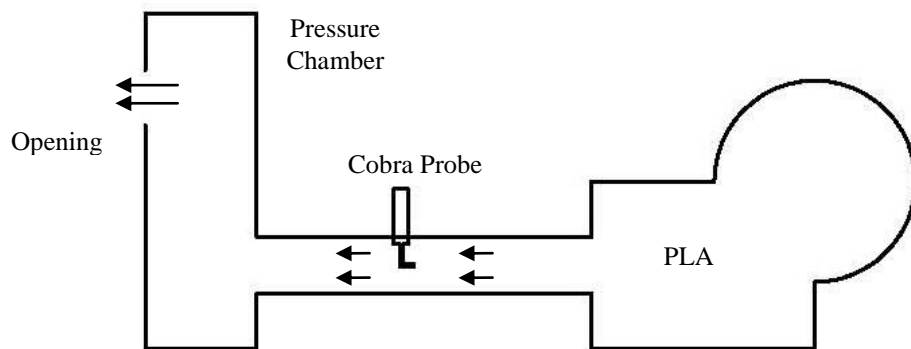


Figure 5-1: Setup for measuring the discharge coefficient, with the opening shown in the pressure chamber and arrows indicating positive flow direction

Opening areas A2, A3 and A4 described for the wind tunnel model were also used as orifice sizes in the discharge experiments. The openings were made of 6mm thick Perspex and could be interchanged onto the pressure chamber. In addition, a sharp edged circular opening

and a 6mm thick circular opening, both of 56mm diameters were also used as test configurations. The two circular openings have areas equivalent to a 50mm x 50mm square opening (A3). The sharp edged circular opening is shown in Figure 5-2, and area A3, 50mm x 50mm is shown in Figure 5-3 as examples of openings.

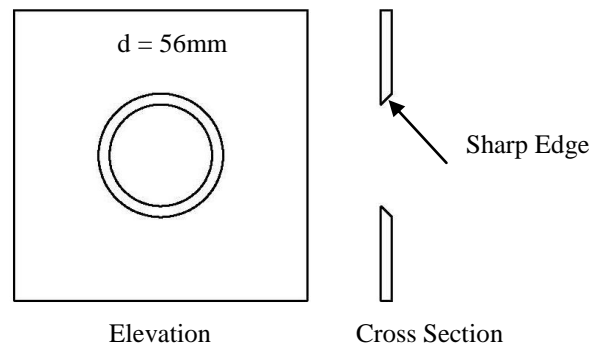


Figure 5-2: Sharp edged, 56mm diameter, d circular opening

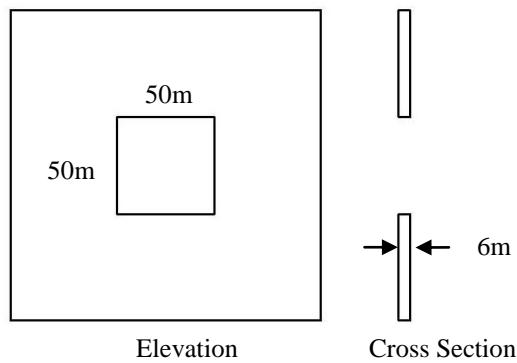


Figure 5-3: 6mm thickness, 50mm x 50mm square opening

## 5.2 Results and Discussion

The pressure fluctuations across an opening are found by obtaining a trace of the net pressure (i.e. external – internal pressure). Figure 5-4 shows a 3-second portion of the net pressure across opening A3 with volume V7, obtained in the wind tunnel experiments. The mean, standard deviation, maximum and minimum  $C_{p\ net}$ , for the entire time history were measured to be -0.07, 0.16, 0.57 and -0.88 respectively. A  $\bar{C}_{p\ net}$  of -0.07 is small and results in a very low average pressure difference across the opening. The large  $C_{op\ net}$  of 0.16 is due to the highly fluctuating signal, as observed in Figure 5-4. The large  $\hat{C}_{p\ net}$  and  $\check{C}_{p\ net}$  indicate, that

sizeable flow is still possible even with a small mean pressure coefficient. The highly fluctuating nature of the pressure signal is clearly observed as well as the pressure changing from positive to negative numerous times. The rapid change from positive to negative pressure causes a mass of air to move in and out of the opening.

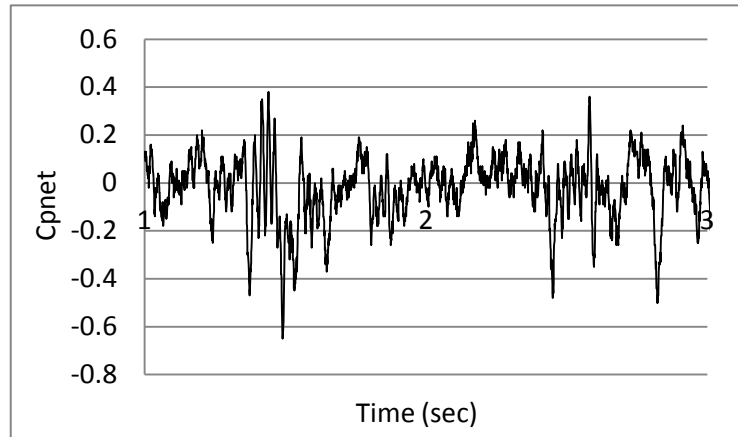


Figure 5-4: Sample net pressure across the dominant opening time history trace

The discharge coefficient can be measured by the steady flow equation shown in Equation 5-1. The steady (i.e. time averaged) flow,  $\bar{Q}$  through the opening of area,  $A_o$  is driven by a pressure difference  $\Delta p$ , where,  $\rho$  is the density of air. For the purpose of this study, the discharge coefficient is considered as a constant and does not vary with time.

$$\bar{Q} = kA_o \sqrt{\frac{2\Delta\bar{p}}{\rho}} \quad \text{Equation 5-1}$$

Table 5-1 presents the measured discharge coefficients for varying opening geometries, such as sharp and thick edges, circular, square and rectangular shaped openings, size of opening areas and mean pressure drops across the opening under a steady pressure. Generally, the discharge coefficients for the sharp edged circular opening are less than those for the 6mm thick circular opening of same area. Similarly, the discharge coefficients for the 6mm thick square opening (A3), are slightly less than those for the 6mm thick circular opening of the same area. In addition, varying the size of the opening area (A2, A4), slightly increased the discharge coefficients compared to the square opening A3 case. The results show that the variation in

pressure drop has minimal effects on the discharge coefficient for steady flow. With the exception of the 6mm thickness A2 opening with a pressure drop of 0.302kPa, the discharge coefficients consistently ranged between 0.65 and 0.78 for all opening configurations. This is similar to results found by Vickery and Karakatsanis (1987), where the discharge coefficient remained nominally constant at 0.7 for Reynolds numbers at the dominant opening larger than 3000. In this test program, the Reynolds number at openings were much larger than 3000. The range of  $k$  between 0.65 to 0.78 is greater than the  $k = 0.61$  under steady flow conditions. The increase in discharge coefficient can be attributed to the turbulent flow which allows an increase of air flow through the orifice due to less separation of the flow at the edges of the opening. Based on the configurations tested, the opening geometries, opening area size and magnitude of the pressure drop under steady flow conditions have some effect on the discharge coefficient for a dominant opening when the pressure drop across the opening is constant.

Table 5-1: Discharge coefficients under steady pressure for various opening configurations

Opening Shape	A (mm <sup>2</sup> )	$\Delta\bar{p}$ (kPa)	Estimated Discharge Coefficient, $k$
Sharp edged circular opening	A3 = 50x50 = 0.0025	0.026	0.65
		0.153	0.68
		0.607	0.69
		1.312	0.69
6mm thick, circular opening	A3 = 50x50 = 0.0025	0.026	0.75
		0.154	0.76
		0.613	0.75
		1.353	0.75
6mm thick, square opening	A3 = 50x50 = 0.0025	0.026	0.68
		0.153	0.68
		0.603	0.67
		1.324	0.66
6mm thick, rectangular opening	A2 = 25x50 = 0.00125	0.302	0.56
		0.681	0.74
		1.760	0.78
6mm thick, rectangular opening	A4 = 80x50 = 0.004	0.105	0.69
		0.357	0.69
		0.647	0.66

Table 5-2 shows the measured discharge coefficient for unidirectional, nominally sinusoidal flow at varying amplitudes and frequencies for opening configurations A2 and A3. In the A2 opening configuration, the discharge coefficient was calculated by varying the amplitude of the sinusoidal pressure trace from 0.21kPa to 0.63kPa, with a nominal constant mean

pressure of 0.7kPa and constant frequency of 6Hz. The change in amplitude had little effect on the discharge coefficient giving values of 0.75 and 0.73 for the 0.21kPa and 0.63kPa amplitudes respectively. When the amplitude was constant at 1.67kPa with a constant mean pressure of 0.9kPa with a varying frequency of 1Hz, 3Hz and 6Hz for, the discharge coefficients had a little variation with values of 0.73, 0.75 and 0.75 respectively. The case where a larger area, A3 was used as the orifice and the mean pressure was varied between 0.487kPa and 1.012kPa for constant amplitude of 1.0kPa and frequency of 5Hz, the discharge coefficients were 0.674 and 0.659 respectively. Overall, when the flow is highly fluctuating but still unidirectional, the discharge coefficient appears to remain relatively unchanged and fall within the range of 0.65 to 0.75. This range of discharge coefficients is similar to those observed from the steady flow results. This suggests that the magnitude and frequency (at least between 1Hz and 6Hz) of fluctuations have little effect on the discharge coefficient.

Table 5-2: Discharge coefficients under unidirectional, sinusoidal flow for varying amplitudes, frequencies and opening configurations

Opening Shape	A (mm <sup>2</sup> )	$\Delta\bar{p}$ (kPa)	Nominal Amplitude (kPa)	Frequency (Hz)	Estimated Discharge Coefficient, <i>k</i>
6mm thick, rectangular opening	A2 = 25x50 = 0.00125	0.712	0.21	6	0.75
		0.752	0.63	6	0.73
		0.941	1.67	1	0.73
		0.943	1.67	3	0.75
		0.946	1.67	6	0.75
6mm thick, square opening	A3 = 50x50 = 0.0025	0.487	1.0	5	0.67
		1.012	1.0	5	0.66

Table 5-3 shows the measured discharge coefficients under reversing (nominally sinusoidal) flow conditions with varying opening areas and frequencies. As discussed, the mean pressure drop,  $\Delta\bar{p}$  changes, there is little effect on the discharge. However, when the pressure in the chamber alternates between positive and negative, the flow direction at the opening also changes direction and results in a much smaller net flow,  $\bar{Q}$ . The smaller  $\bar{Q}$  with respect to the  $\Delta\bar{p}$ , results in a much smaller *k*, since  $\Delta\bar{p}$  implies that the flow is always acting in one direction. The discharge coefficients for decreasing mean pressure differences of 0.199kPa, 0.109kPa and

0.020kPa, are 0.25, 0.16 and 0.19 respectively. The  $k = 0.25$  is larger due to the majority of the flow being in the direction of the positive pressure drop and only a small part of the flow in the reversing direction, causing a larger net flow in the positive direction. However, as the mean approaches 0 kPa, the positive and negative pressures become similar in magnitude and the net flow is reduced.

The discharge coefficients for the A2, A3 and A4 case have also been measured with varying frequency of the reversing sinusoidal pressure trace for a near zero mean pressure. Overall the discharge coefficients are generally less than 0.2, under reversing flow conditions. The exceptions are when  $k = 0.55$  and  $k = 0.39$  for opening A2 with frequencies of 5Hz and 2.5Hz respectively. This is because as mean pressure approaches 0 kPa any observed air flow fluctuations will amplify the discharge coefficient, since the net flow is also expected to be very small. In all cases, the discharge coefficient is reduced to less than measured  $k$  values under unidirectional, sinusoidal flow and steady flow cases.

Table 5-3: Discharge coefficients under reversing flow, sinusoidal flow with varying opening areas and frequencies

Opening Shape	A (mm <sup>2</sup> )	$\Delta\bar{p}$ (kPa)	Nominal Amplitude (kPa)	Frequency (Hz)	Estimated Discharge Coefficient, $k$
6mm thick, square opening	A3 = 50x50 = 0.0025	0.199	1.0	5	0.25
		0.109	1.0	5	0.16
		0.020	1.0	5	0.19
		0.007	1.0	2.5	0.15
		0.027	1.0	1	0.12
6mm thick, rectangular opening	A2 = 25x50 = 0.00125	0.005	1.0	5	0.55
		0.007	1.0	2.5	0.39
		0.014	1.0	1	0.17
6mm thick, rectangular opening	A4 = 80x50 = 0.004	0.003	1.0	5	0.16
		0.005	1.0	2.5	0.20
		0.018	1.0	1	0.21

The reversing flow direction in and out of a dominant opening in a building resembles the reversing flow case in the pressure chamber. This change of flow direction causes the velocity coefficient,  $C_v$  to become smaller since the mean velocity at the vena contracta implies a unidirectional flow across the opening. The actual magnitude of the  $C_v$  from wind tunnel results have not been estimated in this study and remains to be determined. However, if the area

of the vena contracta,  $C_c$  is reduced as suggested by Sharma (1997b) and the velocity at the vena contracta is also reduced, then this would result in discharge coefficients much smaller than the “accepted” value of 0.61 used in many studies.

## 6 Conclusions

Internal pressure generated in a building with a dominant wall opening is a critical design consideration. Buildings with a dominant windward opening have large net pressures acting across roof, side wall and leeward wall envelopes. Internal pressure fluctuations can be exacerbated in a building with a dominant opening by Helmholtz resonance.

This thesis used analytical and experimental techniques to study the effects of varying opening area, internal volume and background porosity of the building envelope on internal pressure characteristics. Numerical simulations were used to estimate the discharge coefficient and inertial coefficient of the flow through the dominant opening. Experiments were also conducted to generate a range of air flows through dominant openings and calculate the discharge coefficients. The main findings of the study are:

- The mean internal pressure in a building is equal to the mean external pressure at the dominant opening when there are no other openings or building porosity.
- Internal pressure characteristics are influenced by the size of the dominant opening area, size of the internal building volume and approach flow characteristics. The area to volume non dimensional parameter  $S^* = (A_o^{3/2}/V_e) \times (a_s/\bar{U}_h)^2$  can be used to relate the variations in internal pressure to external pressure at the opening.
- The inertial coefficient,  $C_I$  of the flow through the dominant opening is dependent on  $S^*$ , and estimated to be in the range of 0.9 to 3.5, with larger  $C_I$  values for higher  $S^*$  values. These  $C_I$  values were determined by matching Helmholtz frequency of the internal pressure spectra using numerical analysis.
- The internal pressure fluctuations (and the resulting peak pressure) are dependent on the discharge coefficient,  $k$  of the flow through the dominant opening. The values of  $k$  were estimated using numerical simulations and ranged between 0.05 to 0.4, and 0.15 to 0.58 from Vickery and Bloxham's linearization techniques. Values for  $k$  are less than the

steady flow value of 0.61 and are dependent on  $S^*$ , where larger  $k$  values occurred at smaller values of  $S^*$ .

- A single lumped opening was used to represent the background porosity of a building. The porosity is represented in non-dimensional form,  $\phi_6$ ; the ratio of the single lumped opening area to dominant opening area.
- Internal pressure characteristics are influenced by background porosity. When  $\phi_6$  is larger than 0.2, the internal pressure mean and standard deviation are attenuated by more than 10% and 20% respectively, compared to the non-porous,  $\phi_6 = 0$ , building case.
- The discharge coefficient for flow through the lumped porous opening,  $k'_L$  is dependent on the dominant opening discharge coefficient (or the magnitude of pressure fluctuations inside the building). When the dominant opening discharge coefficient is large, the lumped porous discharge coefficient was also large.
- The net pressure across a dominant opening (in a nominally sealed building) has a near zero mean pressure, but is highly fluctuating (i.e. changes from positive to negative pressure). The net pressure controls the direction of air flow in to and out of the dominant opening.
- For a nominally steady flow, pressure drop across an opening, the measured discharge coefficient was between 0.65 and 0.7 for sharp edged circular openings.
- For a nominally steady, pressure drop across openings with a thickness of 6 mm and area with dimensions 25mm x 50mm, 50mm x 50mm and 50mm x 80mm, the measured discharge coefficient was nominally between 0.65 and 0.75.
- The discharge coefficient for a unidirectional sinusoidal pressure drop with varying amplitudes and frequencies acting across openings with a thickness of 6mm and areas 25mm x 50mm and 50mm x 50mm was measured to be in the range of 0.65 and 0.75.

- For sinusoidal reversing flow (i.e. crosses 0 Pa) with varying frequencies, the measured discharge coefficient for 6mm thick openings with areas 25mm x 50mm, 50mm x 50mm and 50mm x 80mm was in the range of 0.15 and 0.55.
- The discharge coefficients for the sinusoidal reversing flow are similar to the discharge coefficients estimated from the wind tunnel experiments. These results suggest that dominant opening discharge coefficients are less than the steady flow discharge coefficient of 0.61.

## 6.1 Recommendations for Future Work

This study has analysed internal pressure characteristics in a building with a range of dominant windward wall opening sizes, internal volume sizes and background porosity, using wind tunnel models, and analytical and numerical methods. Mean and fluctuating (i.e. peak and standard deviation) internal pressures were presented in terms of non-dimensional parameters,  $S^*$ ,  $\phi_5$  and  $\phi_6$ . These results can be used for design codification.

However, further  $S^*$  configurations should be tested, primarily in the region where internal pressure peaks and fluctuations transition from being less to larger than the external pressure peaks and fluctuations (i.e.  $0.1 < S^* < 1$ ). It would also be useful to expand the suite of curves for different  $\phi_5$  and to further examine the effects, if any, that  $\phi_5$  would have on internal pressure peaks and fluctuations. It would be of interest to compare wind tunnel results and numerical modelling results with a full-scale building to observe the effects of  $S^*$  and building porosity.

The discharge coefficients derived in this study for fluctuating air flow in and out of a dominant opening, are lower in magnitude than those obtained in steady flow. Furthering the understanding of discharge coefficients for dominant openings may result in improved application of internal pressure for ventilation, structural design and water ingress. Using computational fluid dynamics, simulations and accounting for air momentum could help in quantifying the discharge coefficient in a more standardized format.

## 7 References

- Australian Standard/New Zealand Standard (AS/NZS). (2002). "Structural design actions. Part 2: Wind actions." AS/NZS 1170.2, Standards Australia, Sydney, New South Wales, Australia, and Standards New Zealand.
- ASCE Standard. (2010). "Minimum Design Loads for Buildings and Other Structures." American Society of Civil Engineers 7-10, New York, 2010.
- Boughton, G.N., Henderson, D.J., Ginger, J.D., Holmes, J.D., Walker, G.R., Leitch, C.J., Somerville, L.R., Frye, U., Jayasinghe, N.C. and Kim, P.Y. (2011). "Cyclone Testing Station Technical Report 57: Tropical Cyclone Yasi Structural Damage to Buildings."
- Chaplin, G. C., Randall, J. R. and Baker, C.J. (2000). "The turbulent ventilation of a single opening enclosure." *Journal of Wind Engineering and Industrial Aerodynamics* **85**: 145-161.
- Costola, D. and Etheridge, D. W. (2008). "Unsteady natural ventilation at model scale - Flow reversal and discharge coefficients of a short stack and an orifice." *Building and Environment* **43** (9): 1491-1506.
- Deaves, D.M. and Harris, R.I. (1978) "A mathematical model of the structure of strong winds." Construction Industry Research and Information Association (UK), Report No. 76.
- Etheridge, D.W. (2000). "Unsteady flow effects due to fluctuating wind pressures in natural ventilation design - instantaneous flow rates." *Building and Environment* **35**: 321-337.
- Ginger, J. D. (2000). "Internal pressures and cladding net wind loads on full-scale low-rise building." *Journal of Structural Engineering-ASCE* **126** (4): 538-543.
- Ginger, J. D., Holmes, J. D. and Kopp, G.A. (2008). "Effect of building volume and opening size on fluctuating internal pressures." *Wind and Structures* **11** (5): 361-376.
- Ginger, J. D., Mehta, K. C. and Yeatts, B.B. (1997). "Internal pressures in a low-rise full-scale building." *Journal of Wind Engineering and Industrial Aerodynamics* **72**: 163-174.
- Guha, T. K., Sharma, R. N. and Richards, P.J. (2009). "CFD modelling of transient internal pressure response following a sudden opening in building/cylindrical cavities." 11<sup>th</sup> Americas Conference on Wind Engineering, San Juan, Puerto Rico.

- Guha, T. K., Sharma, R. N. and Richards, P. J. (2011a). "Internal pressure dynamics of a leaky building with a dominant opening", *Journal of Wind Engineering and Industrial Aerodynamics* **99**: 1151-1161.
- Guha, T. K., Sharma, R. N. and Richards, P.J. (2011b). "Full-scale studies of wind induced internal pressure in a warehouse." 13th International Conference on Wind Engineering, Amsterdam, Netherlands.
- Henderson, D., Ginger, J., Leitch, C., Boughton, G., Falck, D., (2006). "Cyclone Testing Station Technical Report 51: Tropical Cyclone Larry damage to Buildings in the Innisfail area."
- Holmes, J. D. (1977). Design and performance of a wind tunnel for modelling the atmospheric boundary layer in strong winds, James Cook University of North Queensland.
- Holmes, J. D. (1979). "Mean and fluctuating internal pressure induced by wind." 5th International Conference on Wind Engineering, Fort Collins, Colorado.
- Holmes, J. D. (2009). "Discussion of: "Net pressures on the roof of a low-rise building with wall openings by RN Sharma and PJ Richards" *Journal of Wind Engineering and Industrial Aerodynamics* **97**: 320-321.
- Holmes, J. D. and Ginger, J. D. (2012). "Internal pressures - The dominant windward opening case - A review." *Journal of Wind Engineering and Industrial Aerodynamics* **100**: 70-76.
- Karava, P., Stathopoulos, T. and Athienitis, A.K. (2005). "Wind driven flow through openings - A review of discharge coefficients." *International Journal of Ventilation* **3** (3): 255-266.
- Kopp, G. A., Morrison, M., Gavanski, E., Henderson, D. and Hong, H.P. (2010). ""Three little pigs" project: Hurricane risk mitigation by integrated wind tunnel and full-scale laboratory tests." *Natural Hazards Review ASCE* **11**: 151-161.
- Leitch, L., Ginger, J., Harper, B., Kim, P., Jayasinghe, N., Somerville, L. (2008). "Cyclone Testing Station Technical Report 55: Investigation of performance of housing in Brisbane following storms on the 16<sup>th</sup> and 19<sup>th</sup> November, 2008."
- Liu, H., (1975). "Wind pressure inside buildings." *Proceedings of the 2<sup>nd</sup> U.S. National Conference on Wind Engineering Research*, Fort Collins, Colorado, June.

- Liu, H. and K. H. Rhee (1986). "Helmholtz Oscillation in Building Models." *Journal of Wind Engineering and Industrial Aerodynamics* **24**: 95-115.
- Liu, H. and Saathoff P. J. (1981). "Building Internal-Pressure - Sudden Change." *Journal of the Engineering Mechanics Division-ASCE* **107** (2): 309-321.
- Malecki, I., Ed. (1969). "Physical Foundations of Technical Acoustics", Pergamon Press.
- Oh, J. H. (2004). "Wind-induced internal pressures on low-rise buildings." Masters Degree Masters Thesis, The University of Western Ontario.
- Oh, J. H., Kopp, G. A. and Incullet, D.R. (2007). "The UWO contribution to the NIST aerodynamic database for wind loads on low buildings: Part 3. Internal pressures." *Journal of Wind Engineering and Industrial Aerodynamics* **95**: 755-779.
- Pearce, W. and Sykes, D. M. (1999). "Wind tunnel measurements of cavity pressure dynamics in a low-rise flexible roofed building." *Journal of Wind Engineering and Industrial Aerodynamics* **82**: 27-48.
- Rayleigh, J. W. S., Ed. (1896). "The Theory of Sound - Volume 2". Reprint. Dover Publications, 1945.
- Rouse, H. ed. (1959). "Advanced Mechanics of Fluids." Wiley, New York.
- Sharma, R. N., Mason, S. and Driver, P. (2010). "Scaling methods for wind tunnel modelling of building internal pressures induced through openings." *Wind and Structures* **13** (4): 363-374.
- Sharma, R. N. and P. J. Richards (1997a). "Computational modelling in the prediction of building internal pressure gain functions." *Journal of Wind Engineering and Industrial Aerodynamics* **67**: 815-825.
- Sharma, R. N. and P. J. Richards (1997b). "Computational modelling of the transient response of building internal pressure to a sudden opening." *Journal of Wind Engineering and Industrial Aerodynamics* **72**: 149-161.
- Sharma, R. N. and Richards, P.J. (2003). "The influence of Helmholtz resonance on internal pressures in a low-rise building." *Journal of Wind Engineering and Industrial Aerodynamics* **91** (6): 807-828.

- Shaw, C. Y. (1981). "Air Tightness - Supermarkets and Shopping Malls." *ASHRAE Journal-American Society of Heating Refrigerating and Air-Conditioning Engineers* **23**: 44-46.
- Tryggvason, B. V. (1979). "Aeroelastic modelling of pneumatic and tensioned fabric structures." 5th International Conference on Wind Engineering, Fort Collins, Colorado.
- Vickery, B. J. (1986). "Gust-Factors for Internal-Pressures in Low Rise Buildings." *Journal of Wind Engineering and Industrial Aerodynamics* **23**: 259-271.
- Vickery, B. J. (1991). "Comments on "The propagation of internal pressures in buildings" by: R. I. Harris." *Journal of Wind Engineering and Industrial Aerodynamics* **37**: 209-212.
- Vickery, B. J. (1994). "Internal-Pressures and Interactions with the Building Envelope." *Journal of Wind Engineering and Industrial Aerodynamics* **53**: 125-144.
- Vickery, B. J. and Bloxham C. (1992). "Internal-Pressure Dynamics with a Dominant Opening." *Journal of Wind Engineering and Industrial Aerodynamics* **41**: 193-204.
- Vickery, B. J. and Karakatsanis, C. (1987). "External wind pressure distributions and induced internal ventilation flow in low-rise industrial and domestic structures." *ASHRAE Transactions* **93**: 2198-2213.
- Woods, A. R. and Blackmore, P. A. (1995). "The Effect of Dominant Openings and Porosity on Internal-Pressures." *Journal of Wind Engineering and Industrial Aerodynamics* **57**: 167-177.
- Yu, S. C., Lou, W.J. and Sun, B.N. (2006). "Wind-induced internal pressure fluctuations of structure with single windward opening." *Journal of Zhejiang University-Science A* **7**(3): 415-423.
- Yu, S. C., Lou, W.J. and Sun, B.N. (2008). "Wind-induced internal pressure response for structure with single windward opening and background leakage." *Journal of Zhejiang University-Science A* **9** (3): 313-321.

## 8 Appendix A – Additional Tables

Table 8-1: Measured area averaged external pressure coefficients for dominant opening sizes A1, A2, A3 and A4

Area (mm <sup>2</sup> )	$\bar{C}_{pW}$	$C_{p\sigma W}$	$\hat{C}_{pW}$
A1 = 20x20	0.52	0.21	2.10
A2 = 50x25	0.53	0.21	2.04
A3 = 50x50	0.55	0.22	1.98
A4 = 50x80	0.52	0.20	1.89

Table 8-2: Measured internal pressure coefficients for dominant opening sizes A1, A2, A3 and A4 with internal volumes V1, V2, V3 and V4

Area (mm <sup>2</sup> )	Volume (mm <sup>3</sup> )	$\bar{C}_{pi}$	$C_{p\sigma W}$	$\hat{C}_{pW}$
A1 = 20x20	V1 = 200x400x100	0.56	0.23	2.06
	V3 = 200x400x300	0.46	0.20	1.42
	V5 = 200x400x500	0.46	0.19	1.24
	V7 = 200x400x700	0.48	0.19	1.54
A2 = 50x25	V1 = 200x400x100	0.57	0.20	1.85
	V3 = 200x400x300	0.50	0.21	1.60
	V5 = 200x400x500	0.50	0.22	1.52
	V7 = 200x400x700	0.53	0.22	1.63
A3 = 50x50	V1 = 200x400x100	0.59	0.23	1.82
	V3 = 200x400x300	0.57	0.23	1.81
	V5 = 200x400x500	0.59	0.26	1.89
	V7 = 200x400x700	0.55	0.23	1.77
A4 = 50x80	V1 = 200x400x100	0.54	0.20	1.64
	V3 = 200x400x300	0.52	0.20	1.62
	V5 = 200x400x500	0.53	0.22	1.68
	V7 = 200x400x700	0.53	0.21	1.69

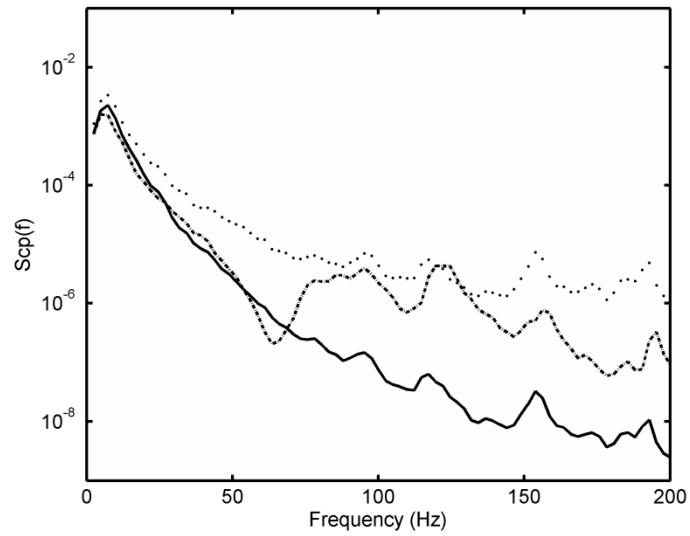
Table 8-3: Dominant opening and internal volume sizes, Helmholtz Frequency with  $S^*$  and  $\phi_5$

Area (mm <sup>2</sup> )	Volume (mm <sup>3</sup> )	$\phi_5$	$S^*$	Helmholtz Frequency (Hz)
A1 = 20x20	V1 = 200x400x100	15.0	1.20	91
	V3 = 200x400x300		0.46	53
	V5 = 200x400x500		0.25	41
	V7 = 200x400x700		0.17	34
A2 = 50x25	V1 = 200x400x100	8.5	6.65	121
	V3 = 200x400x300		2.56	70
	V5 = 200x400x500		1.38	54
	V7 = 200x400x700		0.95	46
A3 = 50x50	V1 = 200x400x100	6.0	18.82	144
	V3 = 200x400x300		7.24	83
	V5 = 200x400x500		3.90	64
	V7 = 200x400x700		2.69	54
A4 = 50x80	V1 = 200x400x100	4.7	38.08	162
	V3 = 200x400x300		14.65	94
	V5 = 200x400x500		7.90	73
	V7 = 200x400x700		5.44	61

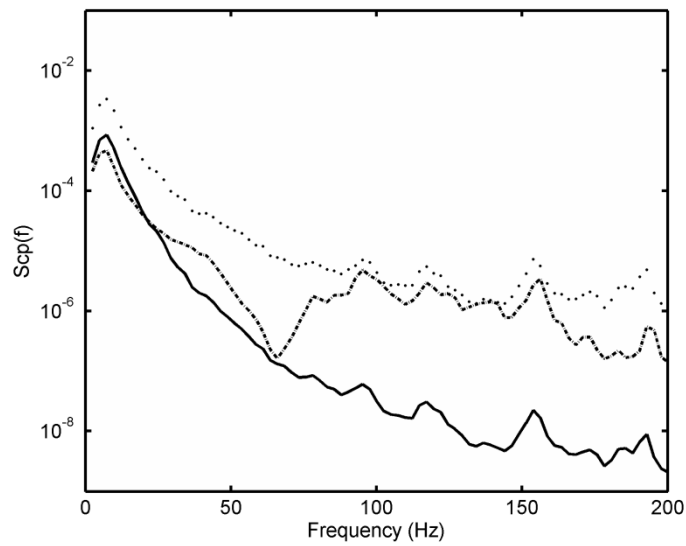
Table 8-4: Ratios of measured internal and external pressure coefficients for varying opening areas and internal volume sizes

Area (mm <sup>2</sup> )	Volume (mm <sup>3</sup> )	$\bar{C}_{pi}/\bar{C}_{pe}$	$C_{\sigma pi}/C_{\sigma pe}$	$\hat{C}_{pi}/\hat{C}_{pe}$
A1 = 20x20	V1 = 200x400x100	1.08	1.10	0.98
	V3 = 200x400x300	0.88	0.95	0.68
	V5 = 200x400x500	0.88	0.91	0.59
	V7 = 200x400x700	0.92	0.90	0.73
A2 = 50x25	V1 = 200x400x100	1.08	0.97	0.91
	V3 = 200x400x300	0.94	1.03	0.78
	V5 = 200x400x500	0.94	1.06	0.75
	V7 = 200x400x700	1.00	1.08	0.80
A3 = 50x50	V1 = 200x400x100	1.07	1.06	0.92
	V3 = 200x400x300	1.04	1.07	0.91
	V5 = 200x400x500	1.07	1.19	0.96
	V7 = 200x400x700	1.00	1.06	0.89
A4 = 50x80	V1 = 200x400x100	1.04	1.00	0.87
	V3 = 200x400x300	1.00	1.01	0.86
	V5 = 200x400x500	1.02	1.09	0.89
	V7 = 200x400x700	1.02	1.05	0.89

## 9 Appendix B – Additional Figures



a) P2  $k = 0.20, k'_L = 0.30$



b) P3  $k = 0.20, k'_L = 0.20$

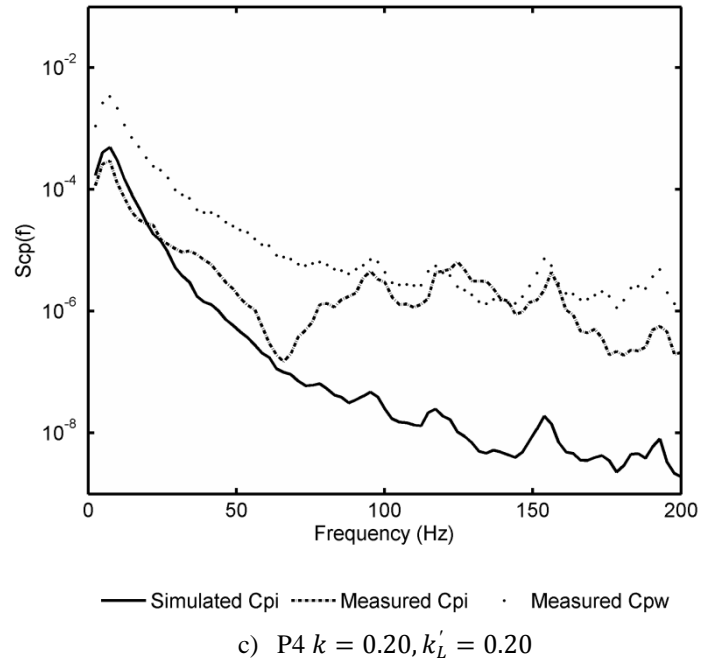
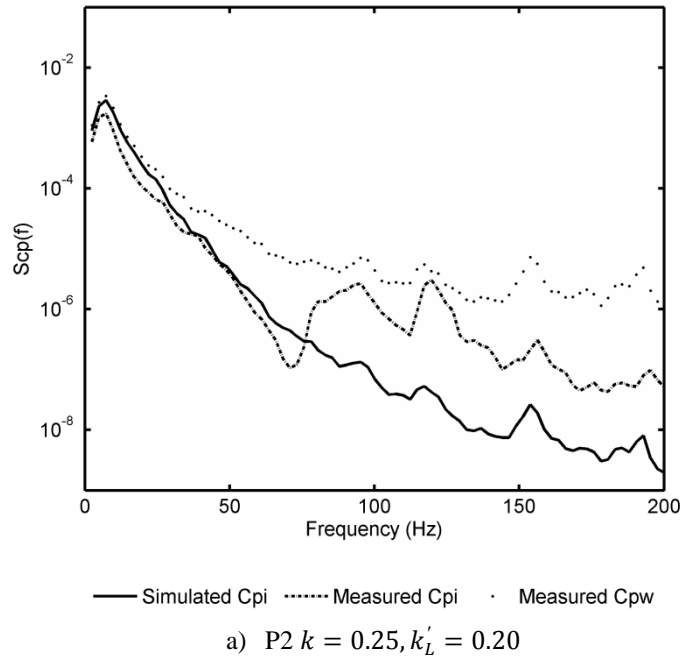
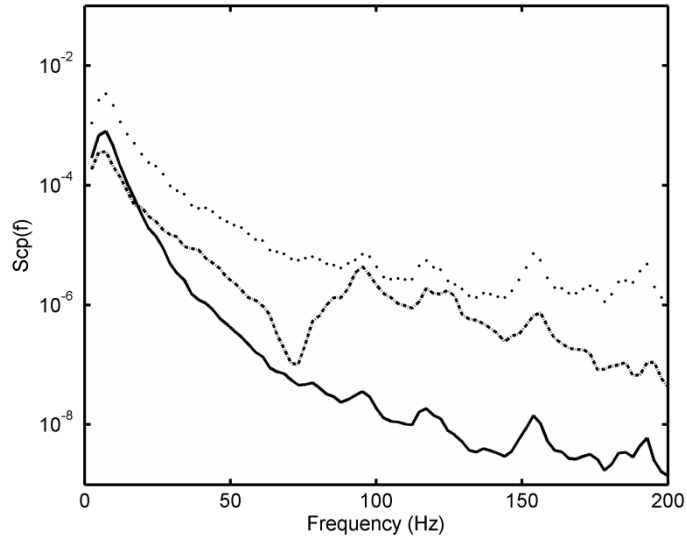


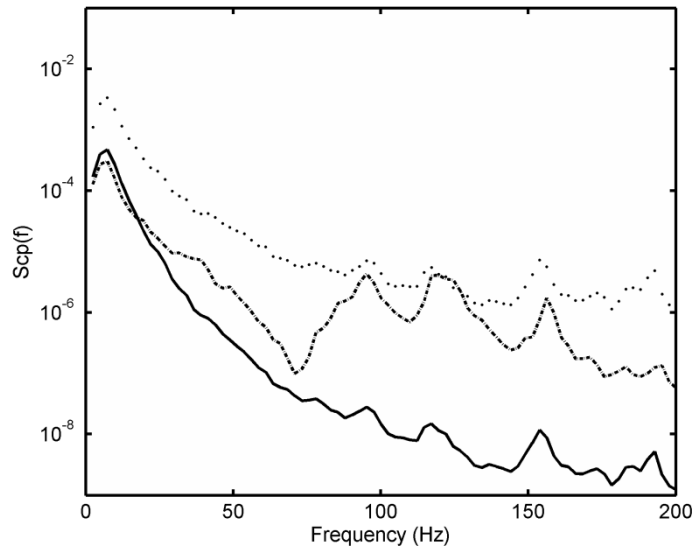
Figure 9-1: Area A1 and internal volume V3 for porosities with a constant  $k$  and varying  $k'_L$





— Simulated Cpi    ..... Measured Cpi    ····· Measured Cpw

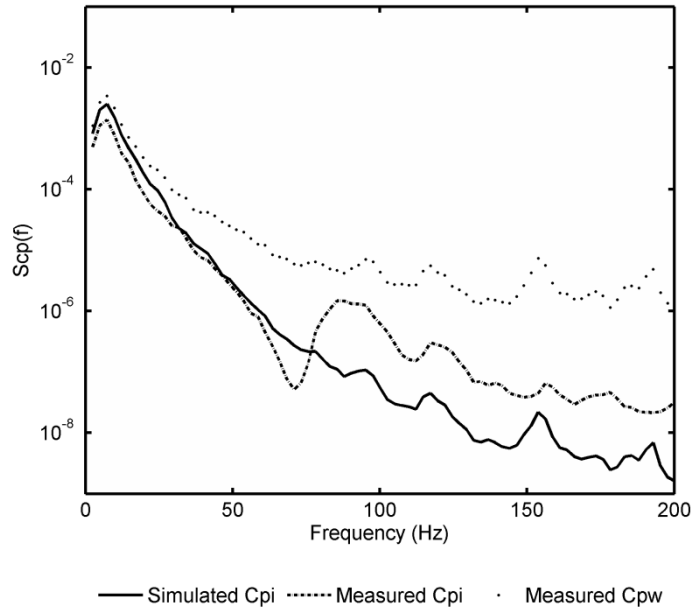
b) P3  $k = 0.25, k'_L = 0.25$



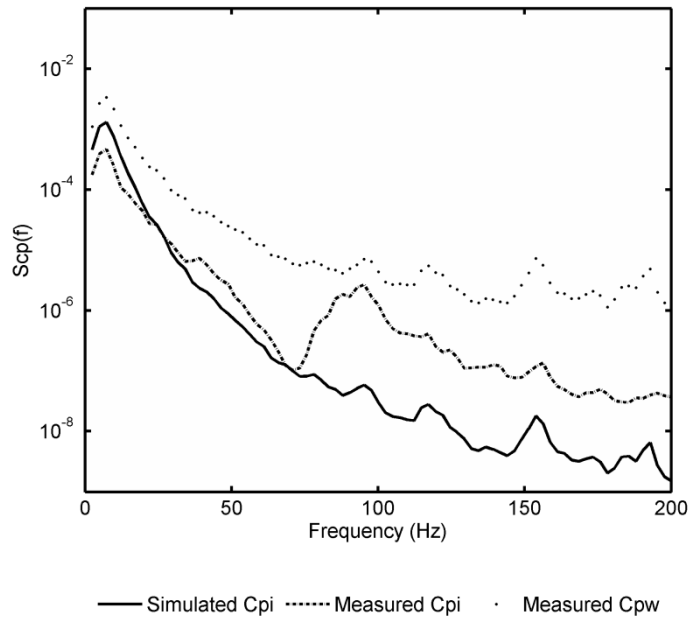
— Simulated Cpi    ..... Measured Cpi    ····· Measured Cpw

c) P4  $k = 0.25, k'_L = 0.25$

Figure 9-2: Area A1 and internal volume V5 for porosities with a constant  $k$  and varying  $k'_L$



a) P2  $k = 0.40, k'_L = 0.50$



b) P3  $k = 0.40, k'_L = 0.30$

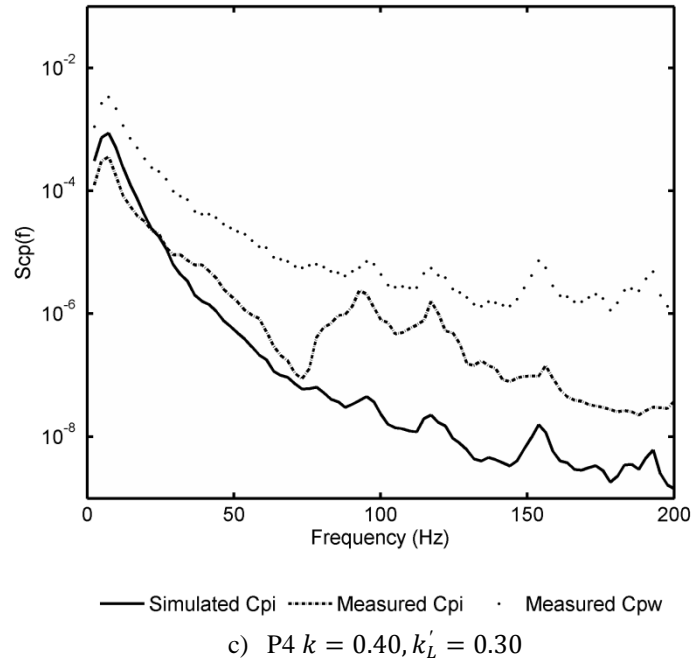
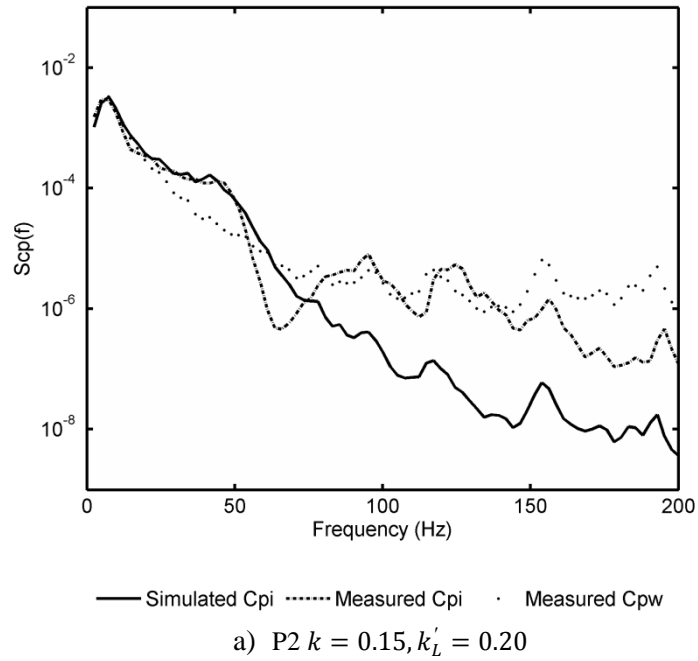
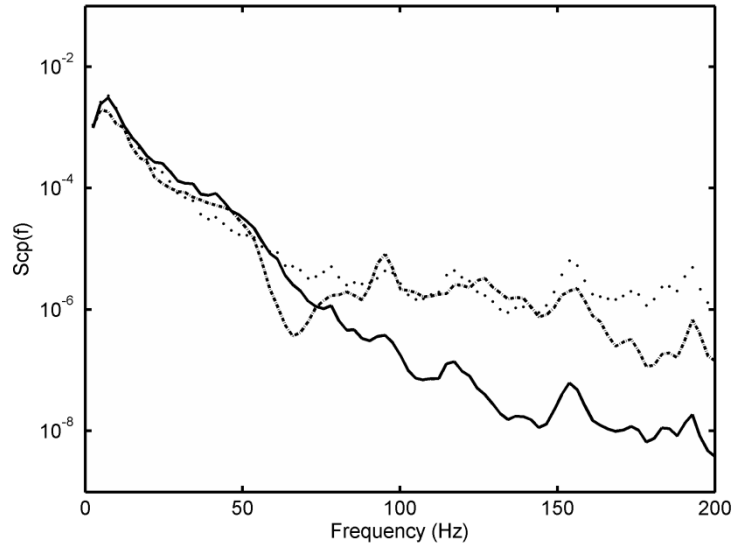


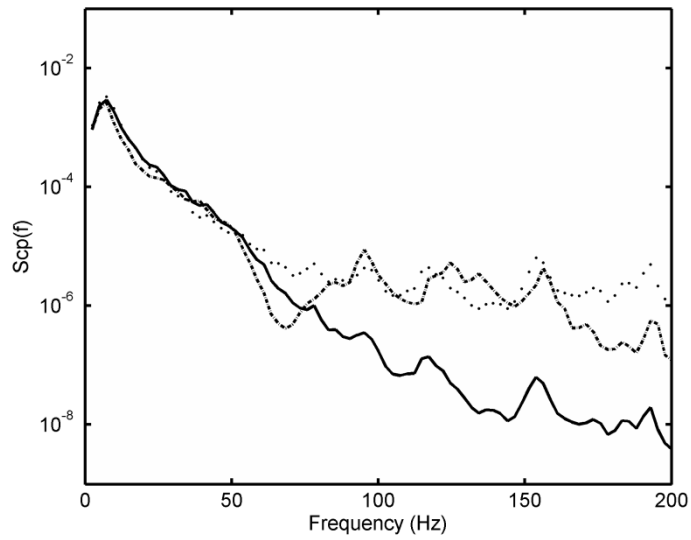
Figure 9-3: Area A1 and internal volume V7 for porosities with a constant  $k$  and varying  $k'_L$





— Simulated Cpi    ..... Measured Cpi    ····· Measured Cpw

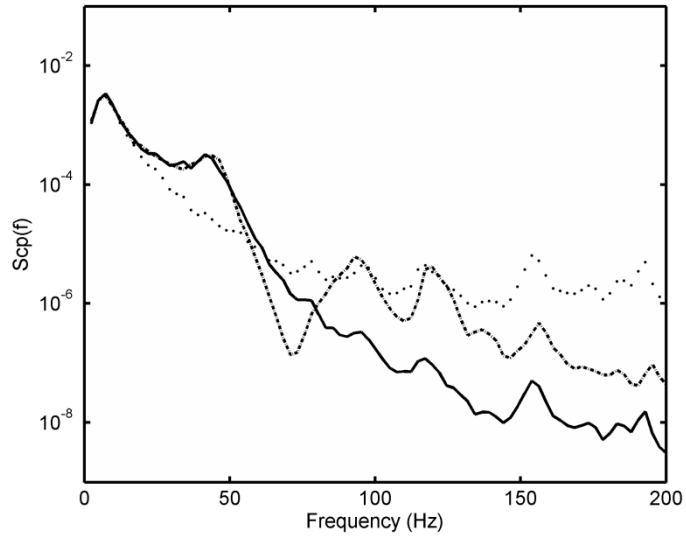
b) P3  $k = 0.15, k'_L = 0.10$



— Simulated Cpi    ..... Measured Cpi    ····· Measured Cpw

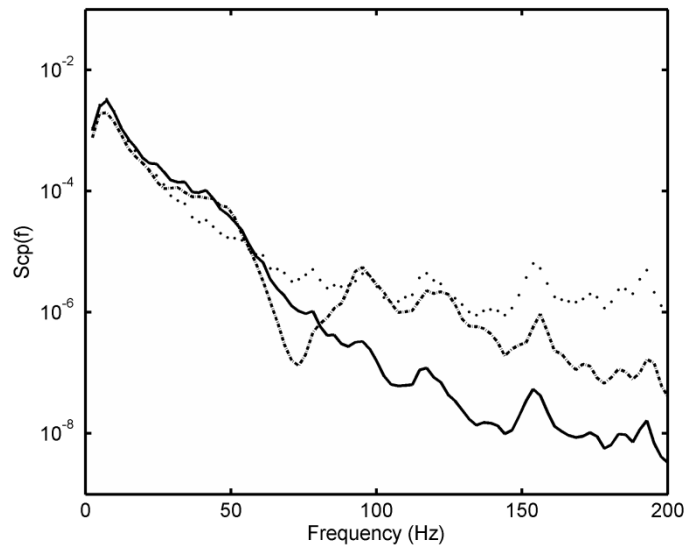
c) P4  $k = 0.15, k'_L = 0.10$

Figure 9-4: Area A2 and internal volume V3 for porosities with a constant  $k$  and varying  $k'_L$



— Simulated Cpi    ..... Measured Cpi    ····· Measured Cpw

a) P2  $k = 0.25, k'_L = 0.10$



— Simulated Cpi    ..... Measured Cpi    ····· Measured Cpw

b) P3  $k = 0.25, k'_L = 0.15$

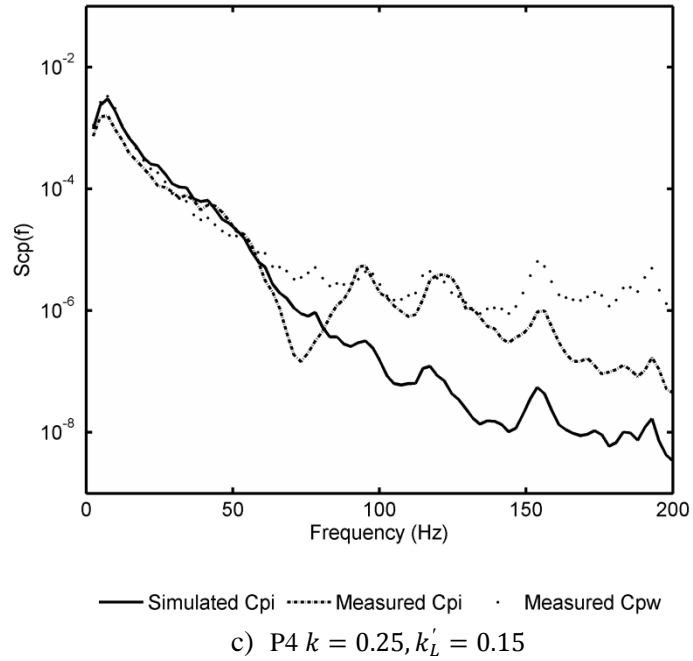
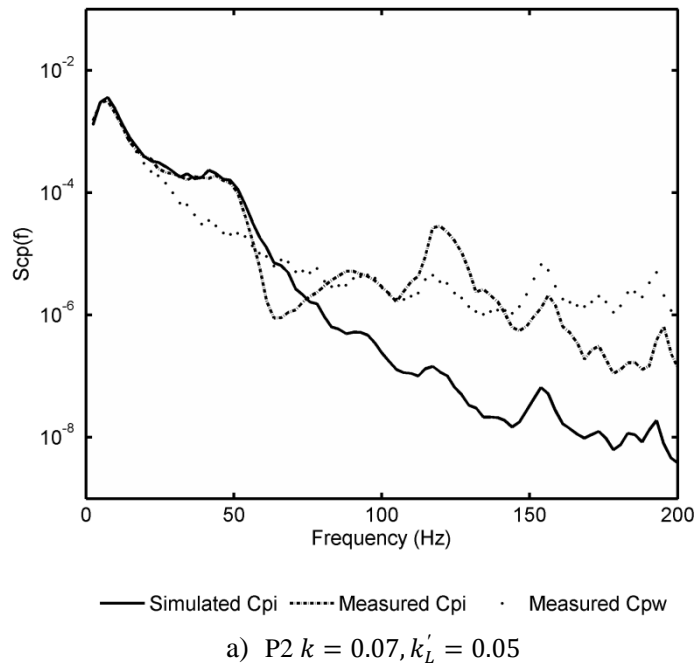
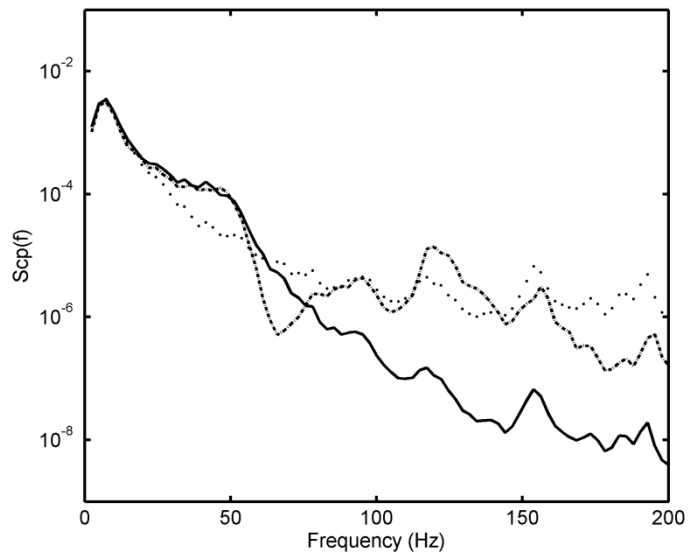


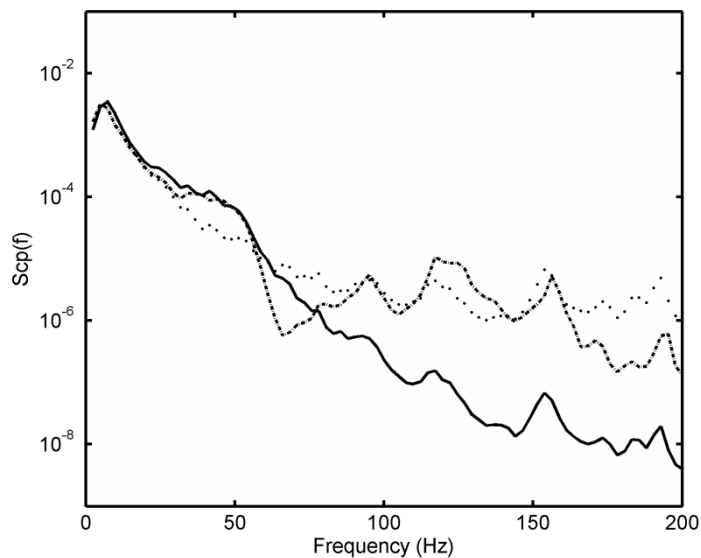
Figure 9-5: Area A2 and internal volume V5 for porosities with a constant  $k$  and varying  $k'_L$





— Simulated Cpi    ..... Measured Cpi    ····· Measured Cpw

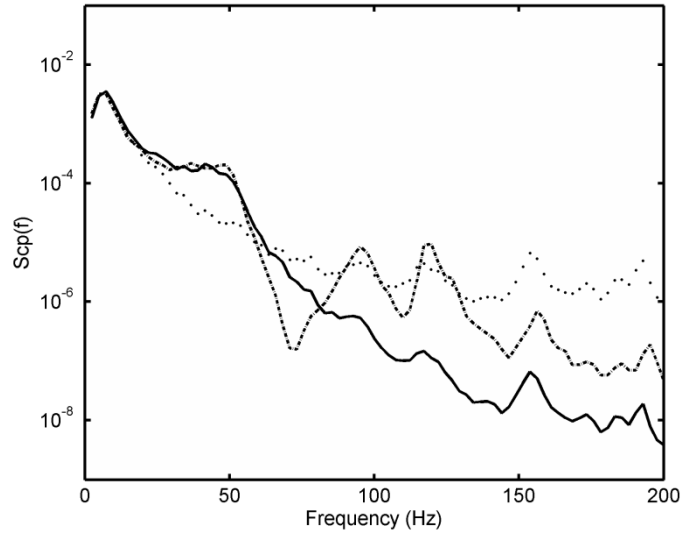
b) P3  $k = 0.07, k'_L = 0.05$



— Simulated Cpi    ..... Measured Cpi    ····· Measured Cpw

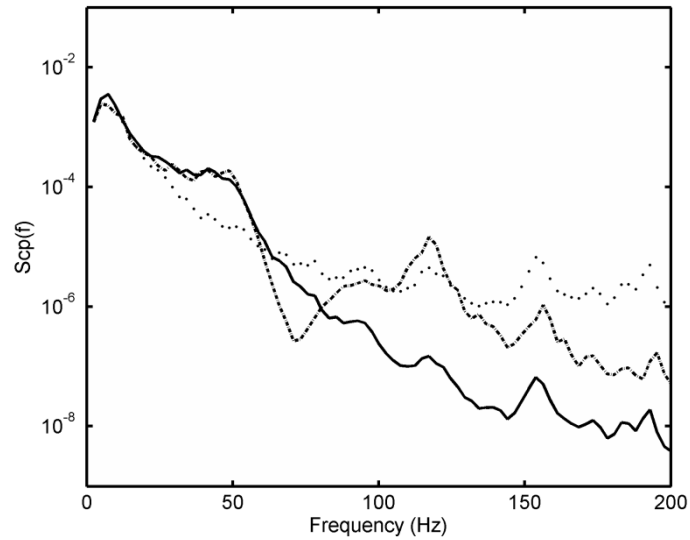
c) P4  $k = 0.07, k'_L = 0.05$

Figure 9-6: Area A3 and internal volume V3 for porosities with a constant  $k$  and varying  $k'_L$



— Simulated Cpi    ..... Measured Cpi    ····· Measured Cpw

a) P2  $k = 0.13, k'_L = 0.25$



— Simulated Cpi    ..... Measured Cpi    ····· Measured Cpw

b) P3  $k = 0.13, k'_L = 0.08$

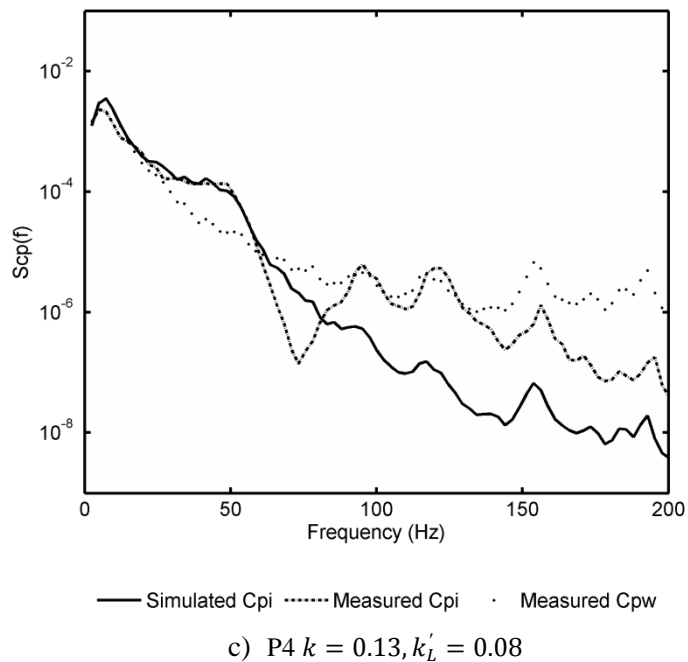
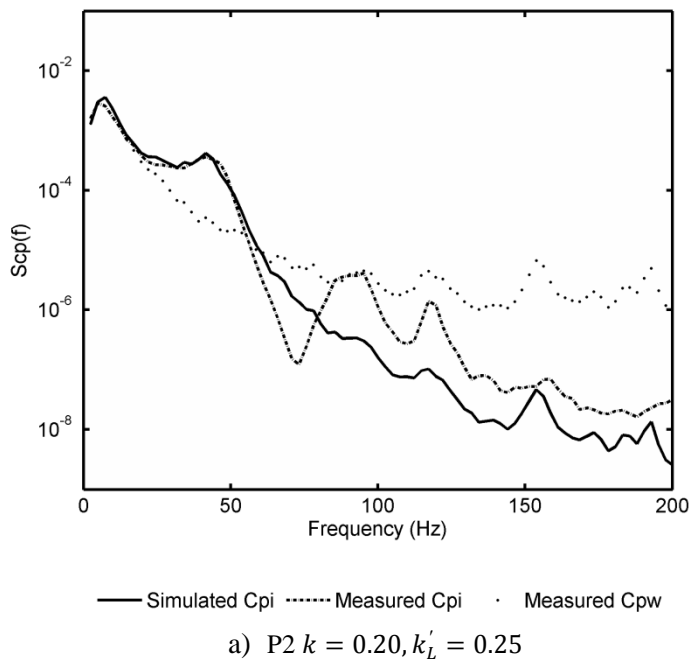
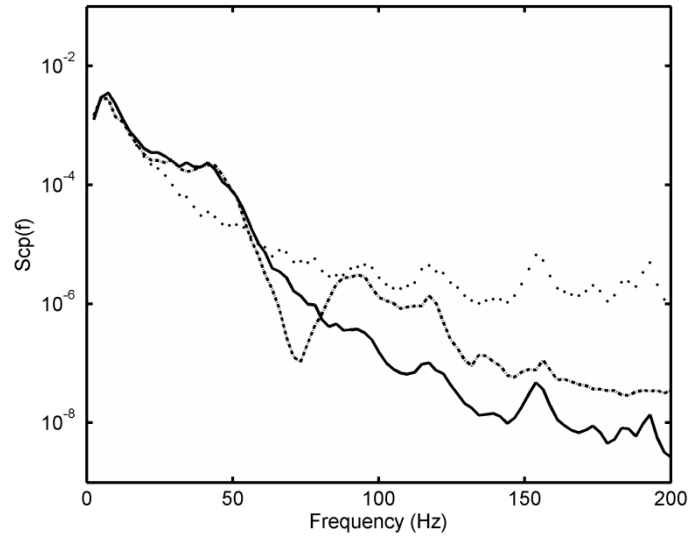


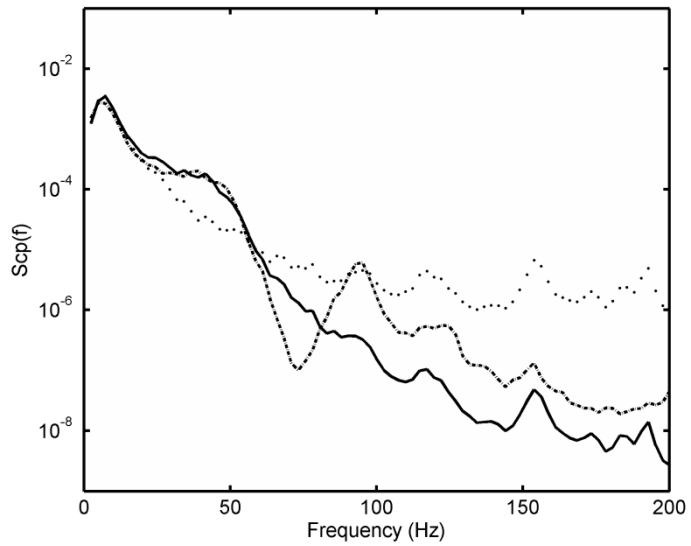
Figure 9-7: Area A3 and internal volume V5 for porosities with a constant  $k$  and varying  $k'_L$





— Simulated Cpi    ..... Measured Cpi    ····· Measured Cpw

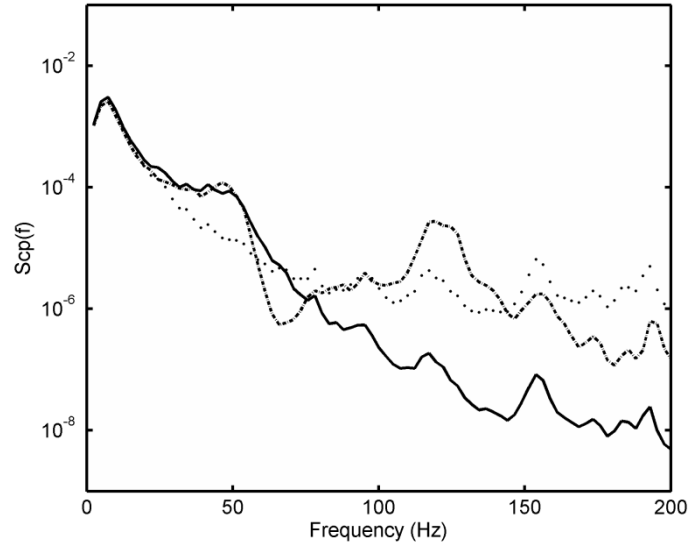
b) P3  $k = 0.20, k'_L = 0.16$



— Simulated Cpi    ..... Measured Cpi    ····· Measured Cpw

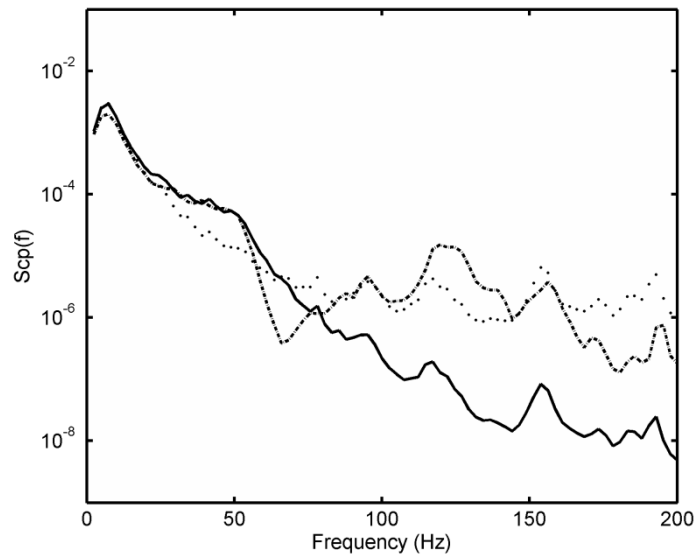
c) P4  $k = 0.20, k'_L = 0.15$

Figure 9-8: Area A3 and internal volume V7 for porosities with a constant  $k$  and varying  $k'_L$



— Simulated Cpi    ..... Measured Cpi    ····· Measured Cpw

a) P2  $k = 0.04, k'_L = 0.10$



— Simulated Cpi    ..... Measured Cpi    ····· Measured Cpw

b) P3  $k = 0.04, k'_L = 0.05$

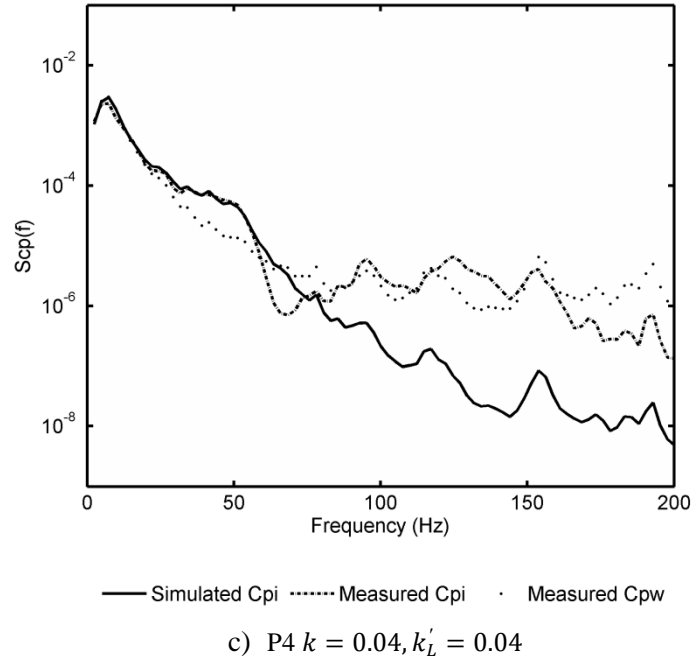
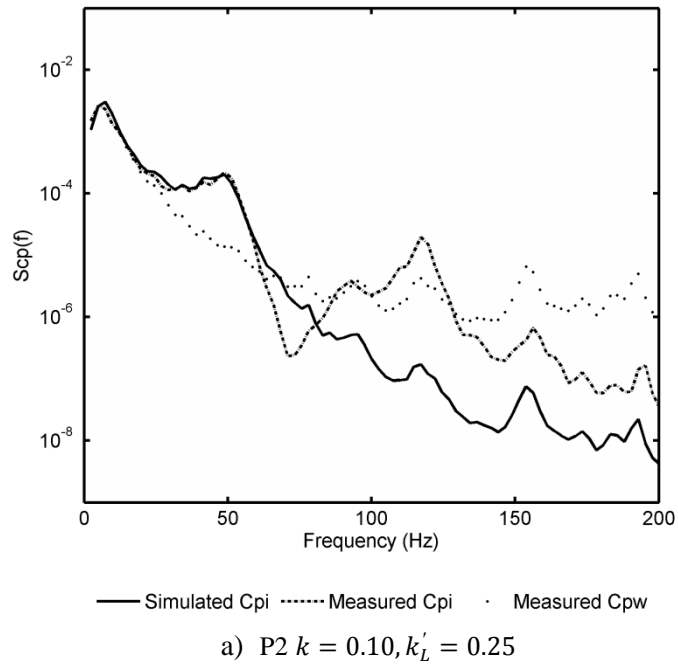
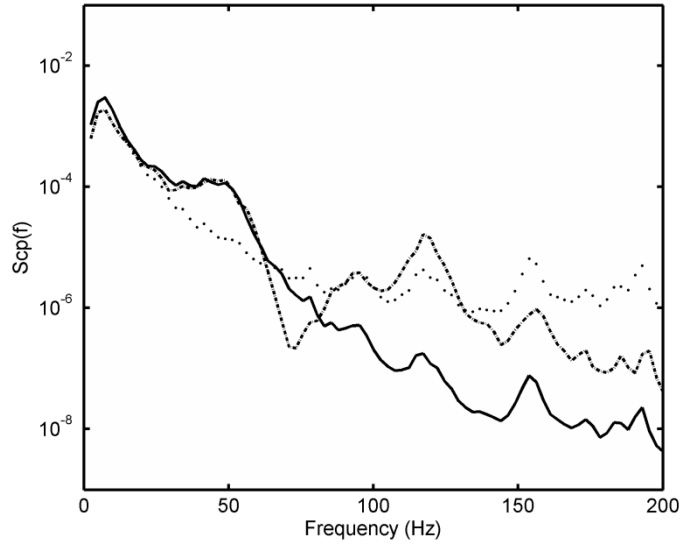


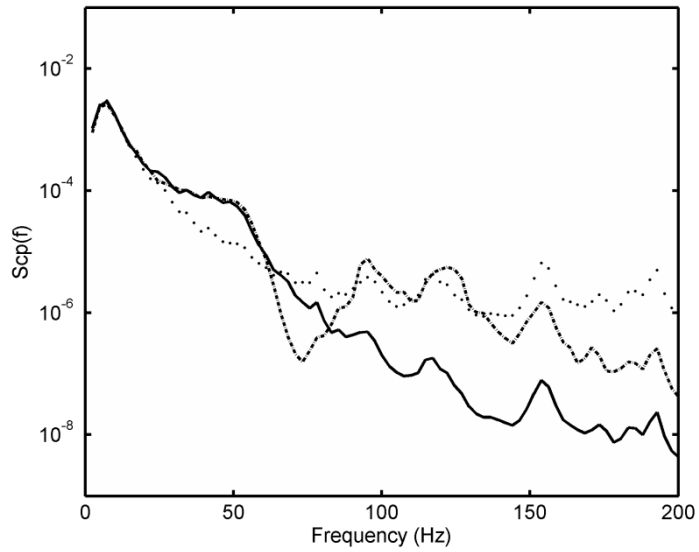
Figure 9-9: Area A4 and internal volume V3 for porosities with a constant  $k$  and varying  $k'_L$





— Simulated Cpi    ..... Measured Cpi    ····· Measured Cpw

b) P3  $k = 0.10, k'_L = 0.12$



— Simulated Cpi    ..... Measured Cpi    ····· Measured Cpw

c) P4  $k = 0.10, k'_L = 0.13$

Figure 9-10: Area A4 and internal volume V5 for porosities with a constant  $k$  and varying  $k'_L$